Master's thesis

NTNU
Norwegian University of Science and Technology
Faculty of Natural Sciences
Department of Materials Science and Engineering

Nicolas Holvik Nygård

Synthesis of a graphitic carbon nitride electrode for hydrogen production by photoelectrolysis of water and ultrasound deposition of nanoparticles

Master's thesis in Chemical Engineering and Biotechnology
Supervisor: Svein Sunde
Co-supervisor: Henrik Erring Hansen
June 2021

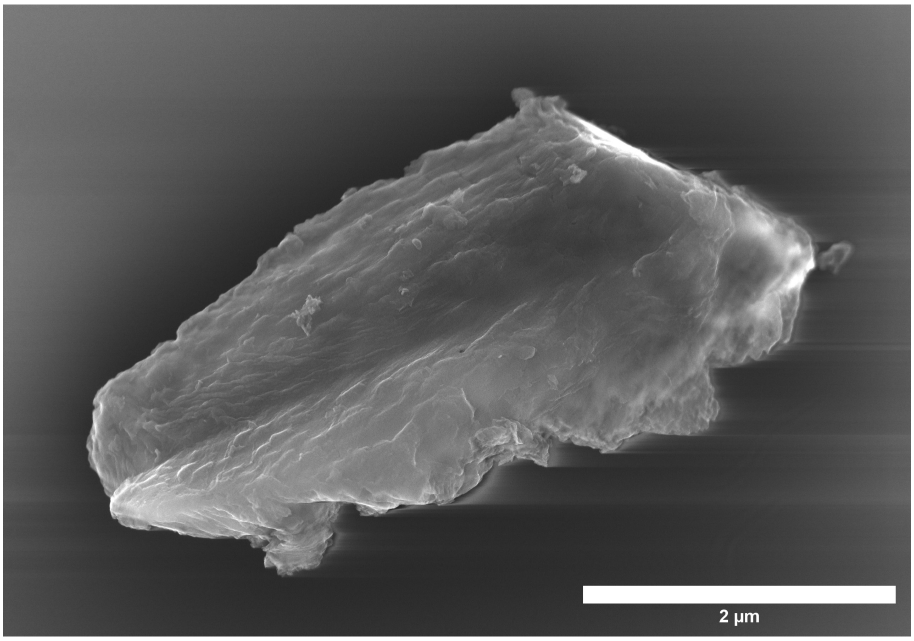

NTNU
Norwegian University of
Science and Technology

Nicolas Holvik Nygård

Synthesis of a graphitic carbon nitride electrode for hydrogen production by photoelectrolysis of water and ultrasound deposition of nanoparticles

Master's thesis in Chemical Engineering and Biotechnology
Supervisor: Svein Sunde
Co-supervisor: Henrik Erring Hansen
June 2021

Norwegian University of Science and Technology
Faculty of Natural Sciences
Department of Materials Science and Engineering

NTNU
Norwegian University of
Science and Technology

Abstract

This project aims to produce hydrogen gas from water using solar radiation for the purpose of providing a renewable energy carrier. In order to do so, a graphitic carbon nitride electrode was produced and synthesized in a facile one-step heating process, on which gas evolution was investigated. Graphitic carbon nitride was produced from dicyandiamide at 550°C and modified through heat exfoliation, ultrasound exfoliation and washing procedures, and the resulting materials displayed band gaps ranging from 2.66 eV for a pristine bulk sample to 2.84 eV for a heat exfoliated sample. Flatband potentials were determined in acidic solutions to be between -1.00 V and -1.20 V, making all the researched materials suited for photocatalytic water splitting. The material was also determined to be a direct n-type semiconductor. Electrochemical tests showed that the exfoliation techniques greatly enhances the properties of the materials, while S(T)EM imaging and XRD verified that the bulk material was converted into sheets, thus increasing the electrochemically active surface area. Platinum deposition on the electrode material was done using $NaBH_4$ reduction and ultrasound techniques, both of which gave enhanced electrochemical properties, but where the ultrasound technique generally performed the best. The material was determined to mainly act as a photoanode with a large overpotential for the hydrogen evolution reaction, indicating that a co-catalyst for the oxygen evolution reaction would be more suited than platinum for improving the overall gas evolution in the investigated systems. In the end, it was found that graphitic carbon nitride does produce hydrogen gas when illuminated by solar irradiation, and a solid theoretical framework is detailed for all observations made in this project.

Dette prosjektet tar sikte på å produsere hydrogengass fra vann ved hjelp av solstråling for å gi en fornybar energibærer. For å gjøre det, ble en grafittisk karbonnitridelektrode produsert og syntetisert i en enkel ettrinns oppvarmingsprosess, hvorpå gassutviklingen ble undersøkt. Grafittisk karbonnitrid ble produsert fra dicyandiamid ved 550°C og modifisert gjennom varmeeksfoliering, ultralydseksfoliering og vaskeprosedyrer, og de resulterende materialene viste båndgap som spenner fra 2.66 eV for en ubehandlet bulkprøve til 2.84 eV for en varmeeksfoliert prøve. Flatbåndspotensialer ble bestemt i syrlige løsninger til å befinne seg mellom -1.00 V og -1.20 V, noe som gjør alle de undersøkte materialene egnet for fotokatalytisk vannsplitting. Materialet ble også bestemt til å være en direkte n-type halvleder. Elektrokjemiske tester viste at eksfolieringsteknikkene i stor grad forbedrer egenskapene til karbonnitridet, mens S(T)EM-avbildning og XRD verifiserte at bulkmaterialet ble omdannet til enkelte lag, og dermed økte det elektrokjemisk aktive overflatearealet. Platinautfelling på elektrodematerialet ble gjort ved bruk av $NaBH_4$ reduksjonsog ultralydsteknikker, som begge ga forbedrede elektrokjemiske egenskaper, men hvor ultralydteknikken generelt presterte best. Materialet var ble bestemt til å hovedsaklig fungere som en fotoanode med stort overpotensiale for hydrogenutviklingsreaksjonen, noe som indikerer at en ko-katalysator for oksygenutviklingsreaksjonen ville vært mer egnet enn platina for å forbedre gassutviklingen i de undersøkte systemene. Til slutt ble det funnet at grafittisk karbonnitrid produserer hydrogengass når den blir belyst av solstråling, og et solid teoretisk rammeverk er gitt for alle observasjoner gjort i dette prosjektet.

Acknowledgements

The guidance of my supervisor, Svein Sunde, and co-supervisor Henrik Erring Hansen has proved invaluable as their insight and chemical intuition has helped this project move forward. From theory, instrumentation and tricks that make laboratory work easier, they have been instructive in an informative and engaging manner. I would also like to thank all the knowledgeable, helpful and kind people at IMA for providing training in different experimental techniques and technical instruments, as well as contributing with wholesome conversations during the ongoing global pandemic. Although I may refer to Svein as the person I bother a couple times a week and Henrik as the person I bother a couple times a day, they really have done an outstanding job in guiding me through this exciting and rewarding year of my life.

Contents

List of Figures

List of Tables

Acronyms

$\boldsymbol{E}_{\mathbf{f}}$ Fermi level.

$\boldsymbol{E}_{\mathbf{g}}$	Band gap energy.
$\boldsymbol{V}_{\mathbf{fb}}$	Flat band potential.
AC	Alternating Current.
CB	Conduction Band.
CV	Cyclic Voltammogram.
DC	Direct Current.
DOS	Density of States.
EDX	Energy-Dispersive X-ray spectroscopy.
EIS	Electrochemical Impedance Spectrocscopy.
eV	Electron volt.
g-$\mathbf{C_3N_4}$	Graphitic carbon nitride.
HER	Hydrogen Evolution Reaction.
HOMO	Highest Occupied Molecular Orbital.
LSV	Linear Sweep Voltammetry.
LUMO	Lowest Unoccupied Molecular Orbital.
MS	Mott-Schottky.
NHE	Normal Hydrogen Electrode.
OCP	Open Circuit Potential.
OER	Oxygen Evolution Reaction.
RC	Resistor-Capacitor.
S(T)EM	Scanning (Transmitting) Electron Microscope.

TGA	Thermogravimetric Analysis.
UV-Vis	Ultraviolet-Visible light.
VB	Valence Band.
XRD	X-Ray Diffraction.

Preface

As this master's thesis builds on what was done and reported in the previous project's work, there will be similarities between the two reports. However, all relevant theory will be expanded upon and most results are significant improvements and advancements of what was found in that work.

1 Introduction

1.1 Background and motivation

With an increasing focus on renewables and decarbonization, hydrogen is becoming attractive with its many applications for reduced environmental impact. The transportation sector could reduce its emissions by using hydrogen fuel cells instead of internal combustion engines, the heating sector could use hydrogen instead of natural gas and portions of the metal industry could exchange reduction chemicals for hydrogen to provide CO_2-free metal production without carbothermic reduction [1]. The common denominator is how hydrogen could potentially exchange fossil fuels with an energy input that leaves only water as the local exhaust product. If produced from renewable energies, hydrogen could create entirely green value chains and speed up the transition to a low-carbon society.

To facilitate the implementation of hydrogen, *graphitic carbon nitride* has been proposed as a potential material for photochemical production of hydrogen from water. With an attractive band gap size of around 2.7 eV, cheap and plentiful precursor materials, high chemical stability and low toxicity, much dedication has been provided to this exciting and promising material in recent years [2]. Properties such as band gap tuning, surface topology, doping, deposition of co-catalysts, precursors and characterization has been studied extensively, and the research is both ongoing and promising.

The research, characterization, optimization and evaluation from this project will provide a solid framework for any future work with graphitic carbon nitride, and will provide key insights into the fundamentals of this material, as well as recommendations for future work and enhancements.

1.2 Aim and scope of the work

This project will seek to create graphitic carbon nitride materials for electrochemical and photocatalytical systems. This will be done *via* a facile one-step heating process. Furthermore, exfoliation techniques with ultrasound and heating will be researched for the purpose of increased surface area and enhanced electrochemical properties. All material variants will be thoroughly characterized and investigated using techniques such as XRD, TGA, S(T)EM, EDX, CV, LSV, EIS, photocurrent and gas evolution measurements. In addition, sonochemistry will be utilized to create a catalyst-cocatalyst system for enhanced properties on the graphitic carbon nitride. It will be investigated under which circumstances the material behaves as a photoanode and photocathode, and detail whether the hydrogen- or oxygen evolution reaction should be the primary target for enhancing the overall gas production rate. The theoretical framework for all of these aspects will be detailed so that a thorough understanding of the mechanisms gives rise to rational decisions about future recommendations and further work.

2 Theory

To properly understand the electrochemical system that this project aims to produce, descriptions of various phenomena and measuring techniques must be described in detail. On the fundamental level, parts of semiconductor physics such as electronic band structures, must be considered in relation to electrochemistry and interfacial charge transfer [3]. The nature of the semiconductor-electrolyte interface, including energy levels and kinetics, as well as the electronic transfer across the junction can be investigated to give greater insight as to how the system at large performs, and gives key insights in as to how to optimize the parameters for future implementation.

2.1 Photoelectrocatalysis

2.1.1 Energy levels and the semiconductor-electrolyte interface

For semiconductors, there are large numbers of atomic orbitals which overlap [4]. According to the Pauli exclusion principle, no two electrons can occupy the same state within the same system. As a system fills up with additional orbitals, the distance between them becomes characteristically very small, practically continuous, followed by a "gap" before a new continuous region arises. These regions of perceived continuous energy levels for electrons to occupy, are called bands. Between bands, there are band gaps, typically measured in electron volts (eV). Semiconductors are generally agreed to have band gaps of between 1 and 4 eV, but band gaps are both material specific and temperature dependent.

In inorganic chemistry, there is a distinction between the highest occupied molecular orbital (HOMO) and lowest unoccupied molecular orbital (LUMO). The former is often known as the valence band VB, in which electrons can be excited into the conduction band CB, which is the latter of the two bands. The distance between them is of such importance that it is usually referred to as *the* band gap, written as E_g. The Fermi level E_f is the energy at which the probability of an electronic state being occupied is 0.5 [5]. For an intrinsic semiconductor, the Fermi level is thus in the middle of a band gap, while for an n-type semiconductor, that is, a semiconductor with a surplus of electrons as the majority charge carrier, the Fermi level is much closer to the conduction band. For a p-type semiconductor, the Fermi level is therefore closer to the VB. The bands of a material vary with the semiconductor potential, ϕ, changing with $-e\phi$, where e is the charge of the electron.

Consider the three diagrams below in Figure 2.1, where the energy levels of an n-type semiconductor and a redox pair in solution are illustrated. The figure shows the band diagrams of the semiconductor on the left side of each of the subfigures, and the density of states (DOS) for the redox couple in the solution on the right. The origins of the latter will be detailed below.

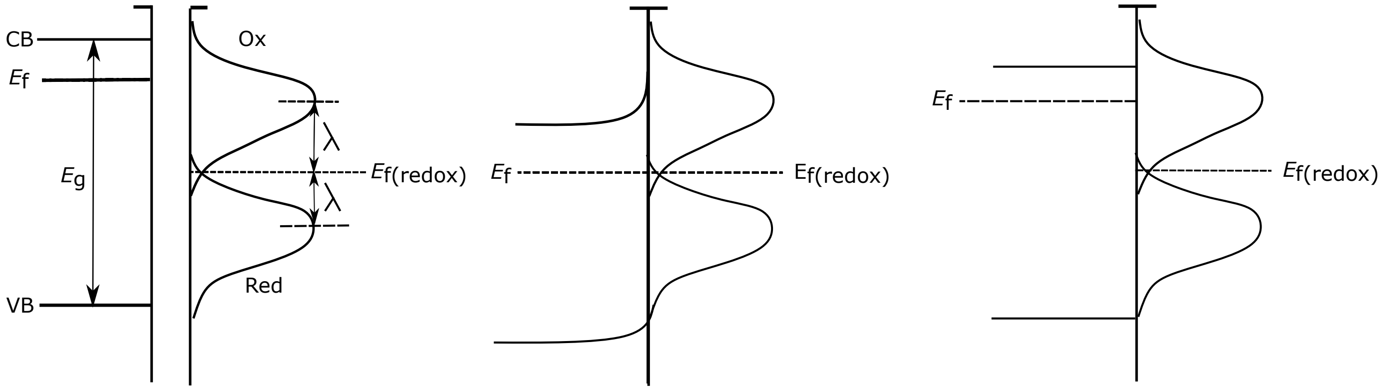

Separated
No junction

In contact
Equilibrium

At flatband potential

Figure 2.1: Energy diagrams for a n-type semiconductor and a redox couple in solution. The diagrams show band edges and band banding when the semiconductor surface comes into contact with a redox pair in solution. By adjusting the applied voltage, one can find the potential at which there is no band bending – the flatband potential V_{fb}.

In the middle subfigure, one can observe how there is a difference in the energy levels of the CB and VB inside the semiconductor and towards the interface with the solution. The bands display band bending, a concept similar to that of a diffuse layer, but inside the semiconductor. This is usually not present for metal electrodes as they have good conductivity. It is however common for semiconductors, for which the conductivity may be on a similar scale to that of the ionic conductors [6].

The redox couple has two oxidation states, where acceptors are denoted as “Ox” as they can be reduced by an incoming electron, and donors are referred to as “Red” in the figure. The energy levels of the solution are a consequence of these, following the reaction [5]:

$$\mathrm{Ox} + \mathrm{e}^{-} \rightleftharpoons \mathrm{Red}$$

As there are charge differences, there will also be attractive and repulsive forces on a molecular scale. In water, ions with positive charges will be surrounded by a sheath of water molecules oriented with the oxygen atom facing them due to the polarity of the water molecule. For a central ion, there is an inner layer of solvent molecules for which the orientation will not change over time. This is referred to as as the "inner sphere". As the distance grows from the central ion, the solvent molecules will be less restrained by the charge of the central ion, but still have a net orientation towards it. This is within the "outer sphere". The energy of the central ion will move up if a random rotation of a solvent molecule orients itself with the same polarity towards the center, and the central ion energy is reduced if such a solvent molecule has its polarity orientation flipped. The latter could be exemplified by a cation central ion for which a water molecule flips from having the hydrogen-side aimed towards the ion, to having the oxygen atom oriented towards it, as seen in Figure 2.2 below.

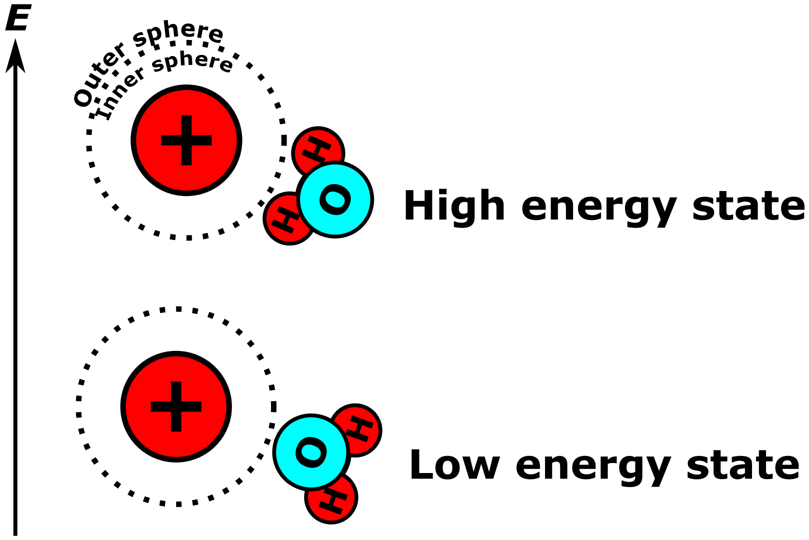

Figure 2.2: Reorganizing the water molecule in the outer sphere from having the hydrogen side oriented towards the central cation to having the oxygen side oriented towards the central ion will lower the energy state of the system.

The quantity that is associated with these changes in energy, is called the reorganization energy λ. λ is thus formally defined as the energy required to distort the reactant and its associated solvent molecules, from their relaxed nuclear configurations, to the relaxed nuclear configurations of the product and its associated solvent molecules [7]. The energy of the central ion traces out a temporal density of states as the solvent molecules reorient in the outer sphere, and these density of states typically have the shapes as illustrated in Figure 2.1 [5].

Equilibrium between two phases is achieved if they have equal electrochemical potentials. A semiconductor's electrochemical potential is the Fermi level E_f; the electrochemical potential for electrons in the semiconductor, usually appearing in the gap of the semiconductor. For redox pairs in solution, the electrochemical is given by $E_{\mathrm{F(redox)}}$.

Different branches of science have a tendency to use different references of energy. For example, in electrochemistry, it is common to use the Fermi level E_f of the normal hydrogen electrode NHE as the reference, while physisists may utilize the vacuum energy scale. These scales are shifted relative to each other by approximately 4.5 eV [3], and the step lengths are equal. Both will therefore be drawn in any relevant illustrations in this paper.

If the interface of the semiconductor makes contact with the electrolyte, and its Fermi level is higher on the vacuum energy scale than the Fermi level $E_{\mathrm{F(redox)}}$ of the redox couple in solution, electrons can migrate from the semiconductor to the redox couple and instil equilibrium between the Fermi levels. This is illustrated in the middle diagram in Figure 2.1. At this stage, there is no external potential or power source, so this leaves the semiconductor lacking in electrons, comparatively. As before, this electrostatic potential will be counterbalanced by ions in the solution. As the bands of the semiconductor is dependent on the voltage, one can artificially alter the potential through a potentiostat so that there is no band bending, thus separating the E_f and $E_{\mathrm{F(redox)}}$. When the band bending is non-existent as a result of the externally applied voltage, the semiconductor has reached its flatband potential V_{fb}.

Band bending, as illustrated in Figure 2.1, is due to the pinning of band edges relative to the energy levels in the solution. This is called band pinning, and in aqueous solutions, the band edges are usually considered to be pinned [8]. In metal-semiconductor heterojunctions, one usually refers to Fermi level pinning as the superior conductivity of the metal leads to its Fermi level being the dominating one.

2.1.2 Water splitting at a photocatalytic electrode

In order for a photocatalytic system to split water molecules into hydrogen and oxygen gas, certain prerequisites must be met. Importantly, the semiconductor VB band edge energy level must more positive than the Fermi level for the OER, determined by the O_2/H_2O or O_2/OH^- in acid or alkaline redox couple, respectively. In addition, the CB edge must be more negative than the Fermi level of the H^+/H_2 in acid or OH^-/H_2 in alkaline on the vacuum scale [2]. Photons with a higher energy input than that of the band gap $h\nu \geq E_g$ must be provided for creating an electron-hole pair. Thereafter, the charge carriers must be transported to an active surface site on which it can interact with water molecules in the solution.

There are in other words three important events which determine the efficiency of the photoelectrochemical system: absorption of light, transfer of charge carriers, and then the actual chemical reaction at the surface. The absorption of light is highly dependent on the band gap of the relevant material, which will be detailed in later sections.

Charge separation is imperative as when the photon creates the electron-hole pair, recombination effects can make these interact and annihilate each other before they contribute to a chemical reaction at the interface with the electrolyte. A long carrier lifetime is therefore preferred.

Reaction at the heterojunction between the liquid and the semiconductor will depend on a range of factors, including surface area and interaction strength between surface and substrate as often illustrated in 'volcano plots', or the Sabatier principle [4]. These plots show how the early d-block metals form too stable surface compounds, while noble metals like gold and silver bond too weakly – both of which are detrimental for any catalytic effect. The platinum metals, however, are in between these two extremes and gives "just the right" binding energy to adsorb reactants, and also desorb products afterwards.

Some of these applied concepts are illustrated in Figure 2.3 below. Note also the relevant experimental values in table 2.1 [2].

Material	Conduction Band [vs. NHE]	Valence Band [vs. NHE]	Band gap
WO_3	0.3 eV	3.1 eV	2.8 eV
CdTe	-0.8 eV	0.9 eV	1.7 eV
g-C_3N_4	-1.2 eV	1.5 eV	2.7 eV

Table 2.1: Band edge positions for a selection of materials. Since WO_3 has its CB higher in energy than the HER, it is not suitable for water splitting. Similarly, CdTe has a VB positioned at a too negative value to evolve oxygen gas. Graphitic carbon nitride has band edges at suitable values for water splitting.

These can be illustrated concurrently with the HER and oxygen evolution values in Figure 2.3 below.

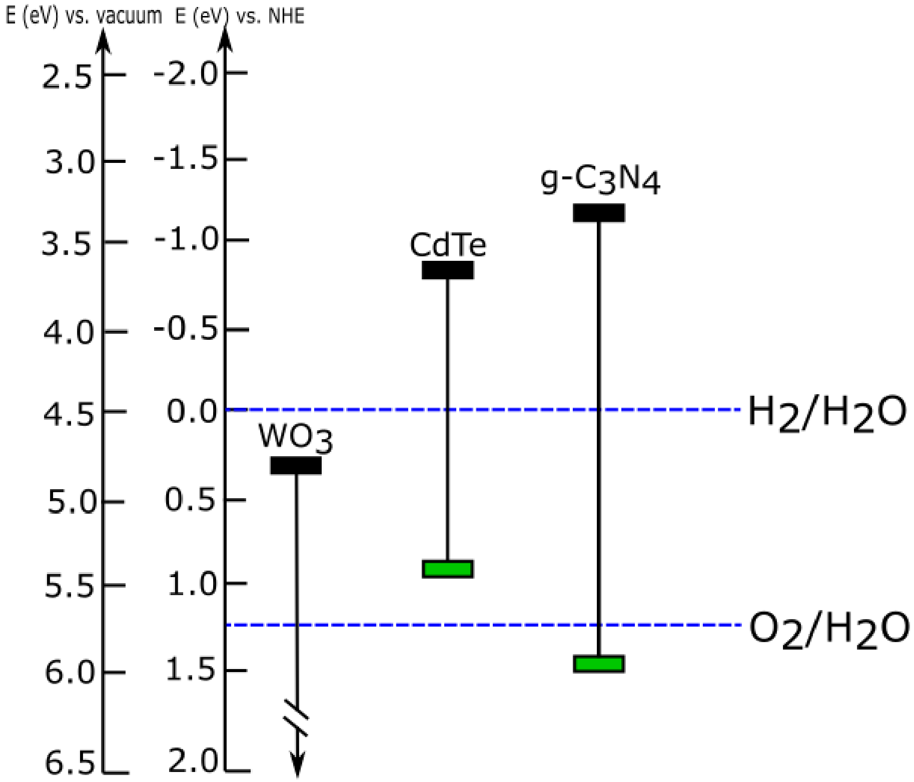

Figure 2.3: Band edges and water splitting. Observe how the WO_3 has a more positive value for its CB (upper bar) than the HER, while CdTe has its VB (lower bar) at a more negative value than the OER. Water splitting is only possible when both of these values are superseded, as present for graphitic carbon nitride.

The figure therefore illustrates why CdTe is unsuited for oxygen evolution, and that WO_3 is unsuited for hydrogen evolution, while g-C_3N_4 is suited for both reactions simultaneously.

The two figures below, Figure 2.4 and Figure 2.5, illustrates all of the necessary and concurrent procedures that take place in a photoelectrochemical cell during water splitting. Focus points are the band bending properties in the cases of anodic and cathodic currents, the oxidation/reduction of the solvent ions by holes and electrons and the photoexcitation from the valence band to the conduction band. First, a photon with energy $h\nu \geq E_g$ will excite an electron from the VB to the CB. When the energy levels of the bands are bending upwards, as is the case in Figure 2.4, the electrons will move towards the ammeter/exterior circuit, while the hole transitions into solution to oxidize one of the ionic components in solution, namely the one acting as a donor [6] [10]. The bands bending upwards may be due to the intrinsic properties of the semiconductor, or it may be due to an externally applied voltage. The oxidized component can then be reduced by an electron arriving from the counter electrode, acting as an acceptor, and the circuit is thus complete. In the case of the bands bending downwards, as in Figure 2.5, the photoexcited electron moves into solution to reduce the oxidized species and the flow of electricity in the circuit moves in the opposite direction from the previous case. As the bands shift with externally applied potential, it is possible to chose which system one operates with.

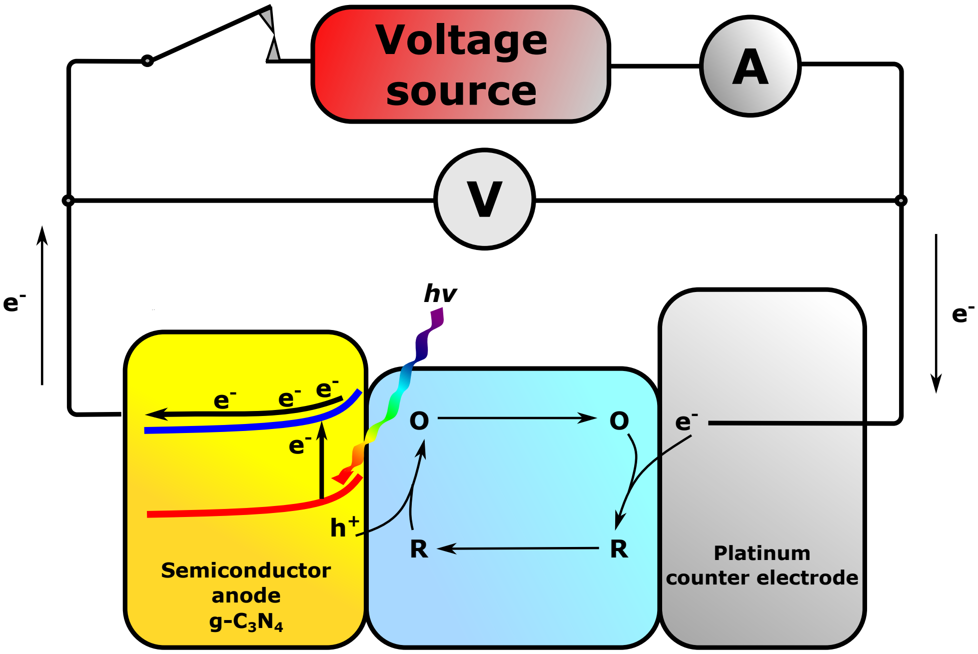

Figure 2.4: Anodic current from semiconductor excitation with upwards band bending. Light with energy higher than the band gap excites an electron which moves through the external circuit. The hole participates in an oxidation reaction with the ionic conductor, which is reduced at the counter electrode to produce a closed circuit.

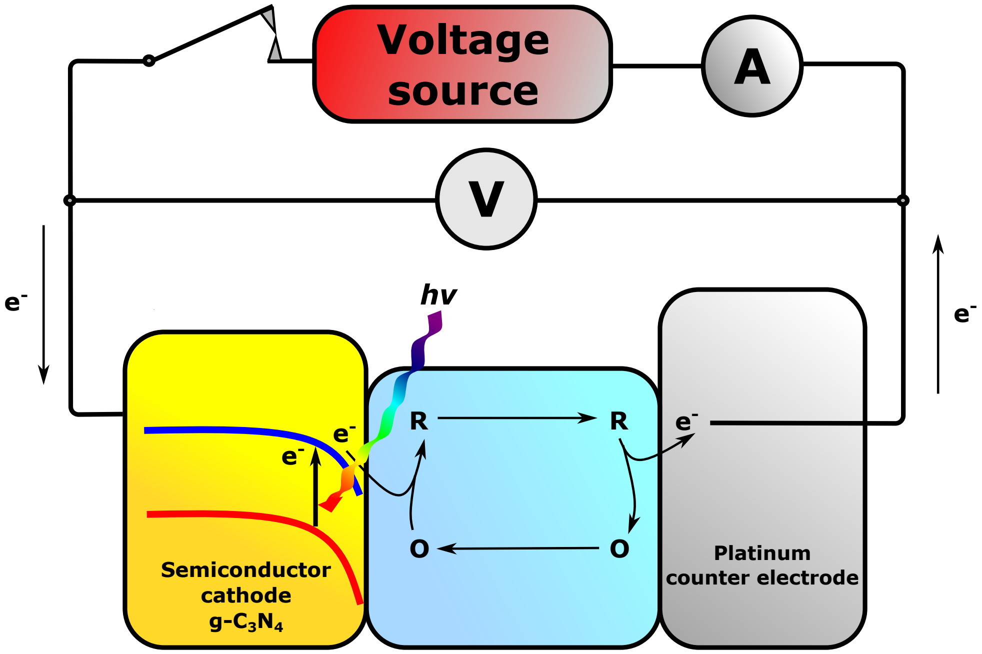

Figure 2.5: Cathodic current from semiconductor with downwards band bending. Light with energy higher than the band gap excites an electron which reacts with the ionic conductor at the interface. This reduced species can be oxidized at the counter electrode to give off an electron and close the electrical circuit.

For a single semiconductor particle in solution, there is no externally applied voltage, and there is no counter electrode. Both processes of donors receiving holes and acceptors receiving electrons must occur at the same time on the particle [3]. An illustration of this is given in Figure 2.6 below. A photon of sufficient energy creates a hole and an electron, both of which must so proceed to oxidize and reduce ionic components in solution, respectively. In the figure the way it is drawn, there is a strong intrinsic overpotential for the electron to reduce the oxidized species O, while there is a lower overpotential for the hole to oxidize the reduced species R. This means that the placement of the band edges favorizes the reduction of the oxidized species. Note that the terminology differs from ordinary electrochemistry, as this overpotential is solely dependent on the band gap, band edge positions and the redox potential for the redox-pair. For a system like this, the electrons generated by incident photons are powerful reductants, but the generated holes are not particularly strong oxidants. As both oxidation and reduction must occur at the same time for this system, the slowest process determines the overall reaction rate [3]. This can be somewhat remedied by adding a hole scavenger, such as methanol, to the solution.

This system is applicable to a semiconductor such as graphitic carbon nitride in water under illumination.

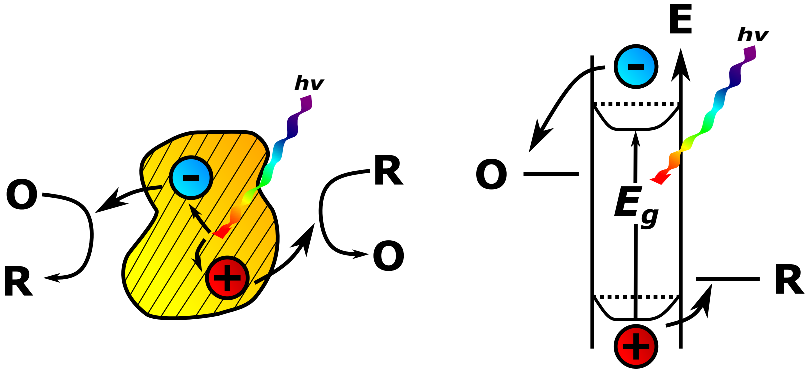

Figure 2.6: Energy diagram for a single n-type semiconductor particle with upwards band bending. The incident light creates both a hole and an electron, both of which need to react with solution components. The slowest process determines the overall reaction rate. In the figure, there is a bigger overpotential for the reduction reaction than the oxidation reaction, making the oxidation reaction the rate limiting step.

Furthermore, the figure illustrates upwards band bending. This is beneficial for the oxidation of the reduced species, due to the increased hole availability at the surface of the particle [9]. This is not a trivial observation: as the reduction reaction has the largest overpotential for this system, the upward band bending contributes to alleviating the rate limiting step of this mechanism, which is the oxidation reaction. It is therefore beneficial for this system to increase the upwards band bending to the benefit of the oxidation reaction and detrimental to the reduction reaction, precisely because of the large overpotential for the reduction reaction/low overpotential for the oxidation reaction. Given this knowledge, one could investigate the design choices which optimizes these parameters. For a small n-type semiconductor particle, the band bending from the surface to the center is given by [9]:

$$V_{\mathrm{BB}}(r) = \frac{kT}{6e}\left(\frac{r_0}{L_{\mathrm{D}}}\right)^2 = \frac{er_0^2 N_{\mathrm{D}}}{6\varepsilon_{\mathrm{r}}\varepsilon_0} \qquad (2.1)$$

where V_{BB} is the voltage difference from the center of the particle to a distance r as a consequence of the band bending, r_0 is the particle size, k is the Boltzmann constant, T is the temperature, e is the elementary charge, L_{D} is the Debye length, N_{D} is the dopant concentration, ε_{r} is the relative dielectric constant and ε_0 is the vacuum permittivity. For an unspecified semiconductor particle, there are three parameters that can be engineered in order to give the desired band bending. These are the particle size r_0, the doping concentration N_D and the relative dielectric constant ε_r from choice of material. For the sake of this project, only the particle size will be elaborated upon. From the expression, one sees that the band bending increases in magnitude as the particle size increases in magnitude. The takeaway from this is that for single semiconductor particles, the band bending in larger particles will benefit the oxidation reaction, while the band bending in smaller particles will benefit the reduction reaction (by being less present). For the previously sketched scenario, where the oxidation reaction was the limiting mechanism, one should thus opt for larger particles in such a system in order to have increased hole availability from the increased band bending in larger particles.

This does not take into consideration differences in electrochemically active surface area in smaller and larger particles. One could easily envision a trade-off for the sketched scenario, but there are findings in literature where only big particles reach the necessary overpotential for a half-reaction, while smaller particles of the same semiconductor would not give the desired reaction, in which the authors attribute this effect to the band bending effects of bigger particles [9].

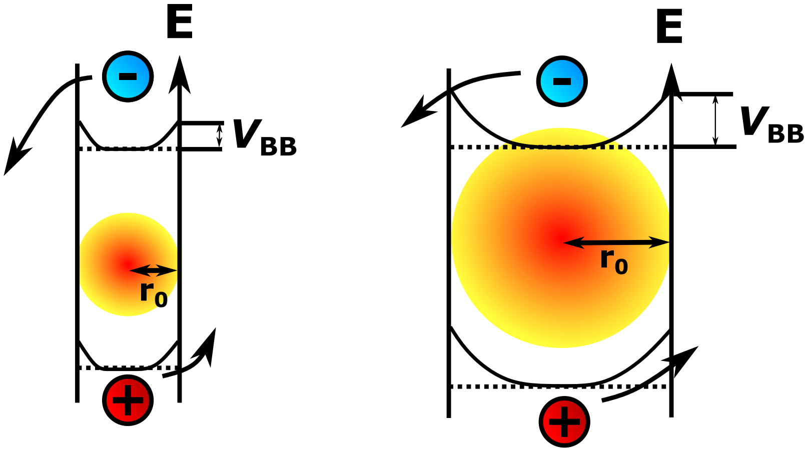

Figure 2.7: Band bending for a big and small particle. At an increased distance r from the center of the particle, the band bending increases. This is beneficial for oxidation reactions and detrimental to reduction reactions.

Additionally, the theory concerning semiconductor-metal interfaces must be detailed, as depositing co-catalysts, such as platinum, creates such an interface. In such a system, the photoexcited electrons would pass through the deposited co-catalyst and from there enter the electrolyte, similar to moving through the external circuit. An advantage of this approach is that the reduction reaction would now mainly happen on the co-catalysts, with its properties reigning supreme over the semiconductor catalyst properties for this particular reaction. The hole would, as before, enter the solution from the semiconductor particle. It could be pointed out that this system is now a junction between a semiconductor and a metal, which is in itself a photovoltaic cell [3]. Figure 2.8 below illustrates the schematics of this system.

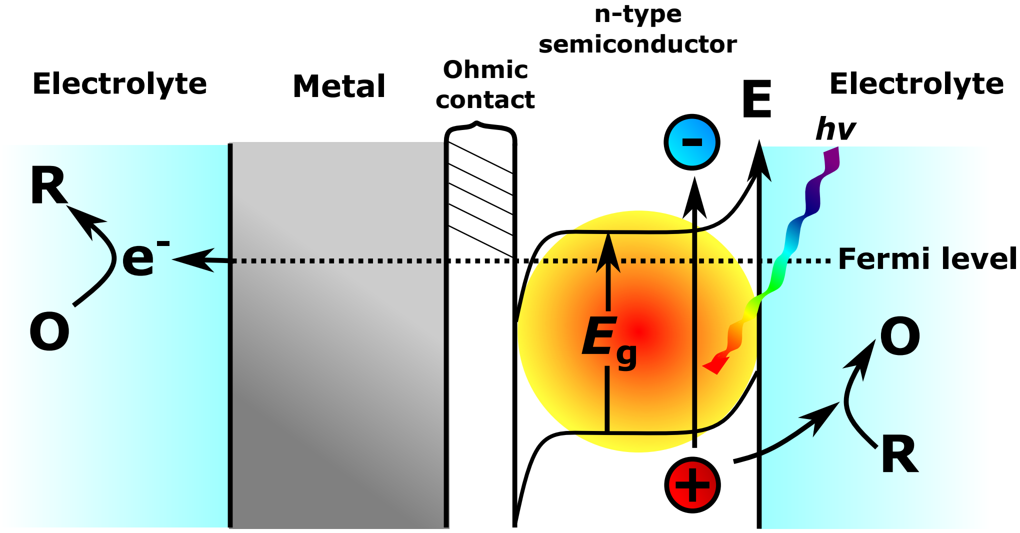

Figure 2.8: The semiconductor-metal interface. The photoexcited electron moves through the deposited co-catalyst metal and participates in a reduction reaction with the electrolyte. The hole participates in an oxidation reaction from the semiconductor surface.

For an n-type semiconductor system with a high overpotential for the reduction reaction and a smaller overpotential for the oxidation reaction, the following conclusions can be drawn:

- The oxidation reaction is the limiting reaction due to its lower overpotential.
- Upwards band bending will improve the overall reaction rate due to the increased availability of holes, but to the detriment of the reduction reaction.
- Larger semiconductor particles will facilitate upwards band bending due to the increased size of the space charge region.

- It is uncertain whether larger surface areas are more beneficial to the overall reaction rate than the increased band bending expected from larger particles.
- Co-catalysts such as platinum will mainly improve the reduction reaction, and should not have a significant impact on the overall reaction rate if the oxidation reaction is the rate limiting reaction.

2.1.3 Photocurrent transients and band edge unpinning

The overall rate constants for water reduction and water oxidation by photogenerated minority carriers are considerably small [11]. As a consequence, these minority charge carriers will accumulate close to or at the surface, and subsequently be at risk for recombination losses with the majority charge carrier. The build up and decay of minority charge carriers at the surface of a semiconductor can be investigated by the photocurrent response from chopped light illumination, where the shapes of the resulting curves indicate the underlying processes. For an ideal system where there are no recombination losses, one expects all the generated charge carriers to participate in reactions with the redox pair in solution. For such an idealized system, the expected photocurrent response would trace out a graph similar to that of the unit step function; when the light is turned on, photocurrent is registered and constant, and the photocurrent stops immediately when the illumination source is turned off. This is illustrated in Figure 2.9.

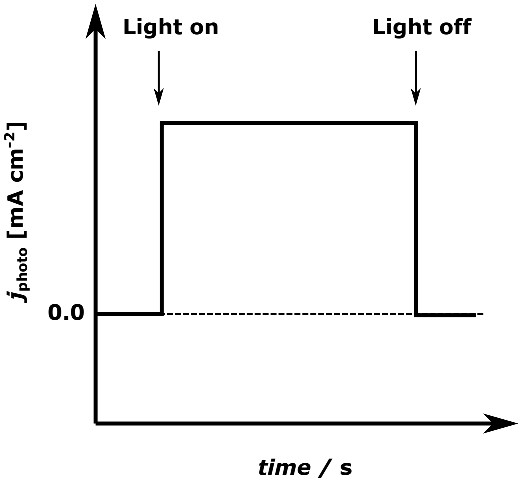

Figure 2.9: Ideal photocurrent behavior. The graph illustrates an idealized system where the charge carriers are generated and consumed immediately under illumination, and the photocurrent disappears instantly when the illumination is removed.

Instead, what is often seen is an initial spike with a certain decay and stabilization while the illumination is present, and an overshoot in the opposite direction when the light is turned of, before decaying towards zero. See Figure 2.10 below.

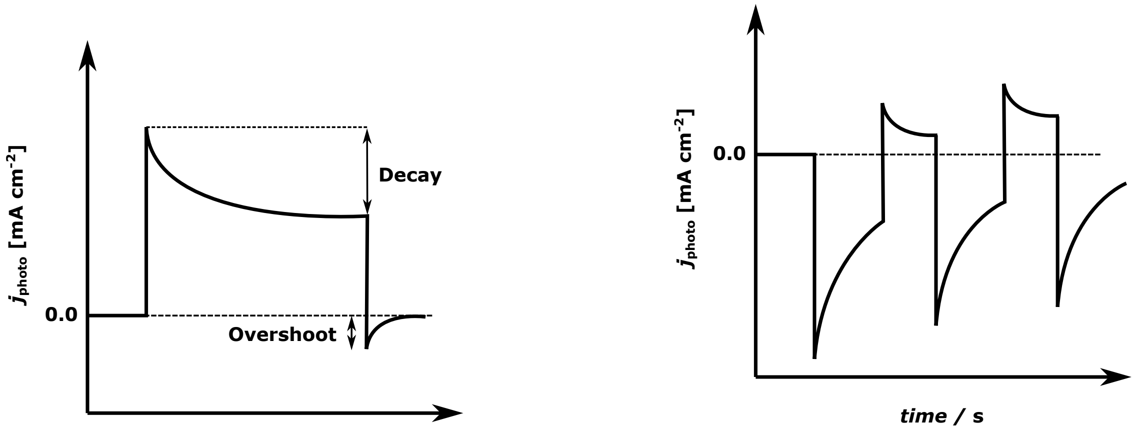

(a) An anodic photocurrent response with an initial spike decaying towards an equilibrium, with an overshoot when the light is turned of, followed by a new equilibrium.

(b) A cathotic photocurrent response with an initial spike followed by a large equilibrium settlement, followed by an overshoot with a decay towards a new equilibrium. Each subsequent measurement rises slightly in the diagram.

Figure 2.10: Examples of anodic and cathodic photocurrent responses with different internal mechanisms and subsequent graphs.

The two subfigures Figure 2.10a and 2.10b above are mostly similar in essence and share many of the same characteristics, but for anodic and cathodic processes. Importantly, they both spike when the illumination is turned on, and they both decay towards an equilibrium. When the illumination ends, they overshoot – meaning the photocurrent passes through zero – before moving towards equilibrium at zero. Note that in both cases, the overshoot is much smaller than the decay. They differ, however, on the speed at which they converge towards equilibrium. The magnitude of the spikes is associated with the RC time constant, where one considers the electrode and electrolyte to be two components in series with a capacitor interface. The RC time constant is thus related to the charging of the space charge region of the semiconductor.

Figure 2.10b shows a system where there is a cathodic spike initially, which decays, and is followed up by an overshoot which is noticeably smaller than the initial response. The current response is also somewhat reduced for each subsequent on-off cycle.

The following section will detail the mechanisms that give rise to these shapes.

1. There is no light, and thus there is no photocurrent response.
2. The light is switched on, giving a sudden spike in photocurrent.
3. The initial spike decays towards an equilibrium.
4. The light is turned off, and a spike moves in the opposite direction, through zero, thus overshooting.
5. The system decays towards equilibrium.

Initially, there is no irradiation, and thus no current (1). The sudden response in the diagrams to the onset of the lighting is due to generation and separation of charge carriers, where the holes – in n-type semiconductors – migrate to the surface of the species to oxidize donors while electrons move through the external circuit, as detailed in earlier chapters (2). The congregation and build up of minority charge carriers – holes – at or near the surface will lead to an increased flow of electrons into the surface, leading to recombination and subsequently reducing the photocurrent. This is the mechanism of the first decay after the initial on-spike. An equilibrium is reached after some time due to the holes, which are reaching the surface, are now being balanced and consumed by electrons from both recombination and by charge transfer (3). The measured current is necessarily related to the current passing through the semiconductor/electrolyte interface [11]. When the light is turned off, no more holes are being produced. But the remaining ones will continue to be consumed by existing electrons from both recombination and charge transfer, which explains the overshoot that passes through zero (4). The overshoot decays towards an equilibrium as the remaining holes get consumed by electrons (5).

However, this cannot be the full picture. From this explanation alone, one should expect that the initial rise in photocurrent should be exactly the same but opposite magnitude of the off-spike. This is often not the case, which is especially clearly drawn in Figures 2.10a and 2.10b. What is not accounted for at this point, is that the accumulation of holes towards the surface of the semiconductor is affecting the potential distribution across the semiconductor/electrolyte junction. This affects the potential drop in the Helmholtz layer as well as in the space charge region. This in turn affects the band edges and band bending, as these are in fact dependent on these voltages. This phenomena is referred to as light-induced band edge unpinning

[11], and explains why the loss of symmetry occurs for most systems investigated. In addition, some decays are remarkably slower than other forms of decay. This is usually attributed to trapping of holes in surface states. Presence of trapping will reduce the photochemical activity of the electrode due to fewer charge carriers being able to participate freely in reactions [12].

In addition, shapes like the one in 2.10a have been empirically shown to be dependent on the intensity of the light, with the pattern marked with the black arrow emerging. See Figure 2.11 below. The opposite pattern is observed with increased voltages, as shown in the same figure with the green arrows [11] [12].

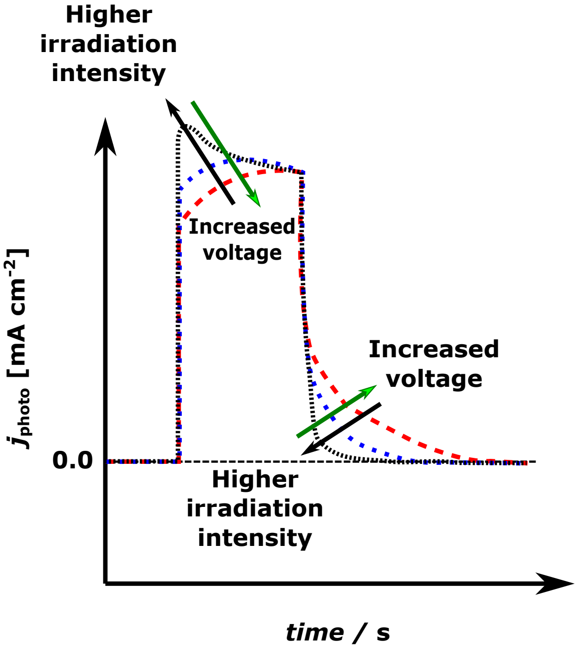

Figure 2.11: Photocurrent responses to intensity and applied potential. The illustration shows that with high intensity radiation and/or low applied voltages, the first spike in the diagram is more intense and decays downwards, while at low intensity and/or high voltage, the first spike converges towards equilibrium in an upwards motion. The decays after the light is switched off is also affected by these parameters, all of which indicate band edge unpinning.

Furthermore, some studies suggest that even more factors contribute to complicating the picture. It has been suggested that the rising nature of Figure 2.10b may be due to a local change in pH with production of either hydrogen or oxygen. At photoanodes with oxygen production, the reduced pH that the OER locally brings forth is expected to shift the flatband potential positively, with a subsequent reduced band bending at a given applied voltage. In a similar manner, an analog mechanism is proposed for photocathodes with a local increase in pH as a result from the HER, moving the flatband potential negatively and thus increasing band bending at a given applied voltage. This could thus be a measureable indication of successful gas evolution as a result of illumination. With sufficient stirring, these effects should be negligible. The slow rise after the initial spike is attributed to a combination of charge carrier build up at the surface, as well as trapping mechanisms that are slowly remedied.

In either case, it is evident that chopped light illumination methods can give much insight into the mechanisms and properties of the investigated materials. Gas evolution is indicated by rising extremities for each subsequent measurement, the presence of trapping can be investigated from the shapes of the curves, while effects and behavior of charge separation can be investigated with inspection of the curves under different applied voltages. This last part due to the electric field interacting with the free charges [11] [12].

2.2 Sonochemical production and deposition of nanoparticles

Ultrasound is sound waves of particular frequencies, defined between 16 kHz and 500 MHz in liquids [13]. The lower spectrum (20-100 kHz) is called low frequency or power ultrasound, and is best suited for mechanical applications of ultrasound. The frequency range from 100 kHz to 1 MHz is where sonochemical reactions are the most present. The main reason for sonochemical effects are due to *cavitations*, which is the process of bubble formation, growth and violent collapse as a result of the expansion and contraction of the medium. The bubble collapse is very high in energy density, reaching pressures of 2000 atm and temperatures of 5000 K, effectively transforming the low energy density of the ultrasonication into intense chemical environments. For processes in water, this will lead to a sonochemical pyrolysis, or sonolysis, of the water molecules, creating hydrogen radicals, H• and hydroxyl radicals, OH•. A proposed reaction mechanism is as follows, with ultrasound being symboled by))) [14]:

$$\mathrm{H_2O} \xrightarrow{)))} \mathrm{H\bullet} + \mathrm{OH\bullet} \tag{2.2}$$

$$\mathrm{RH} + \mathrm{\bullet OH(\bullet H)} \xrightarrow{)))} \mathrm{R\bullet} + \mathrm{H_2O(H_2)} \tag{2.3}$$

$$m\mathrm{M^{n+}} + \mathrm{n}m\mathrm{H\bullet} \longrightarrow (\mathrm{M^0})m + \mathrm{n}m\mathrm{H^+} \tag{2.4}$$

$$m\mathrm{M}^{\mathrm{n}+} + \mathrm{n}m\mathrm{R}\bullet \longrightarrow (\mathrm{M}^0)m + \mathrm{n}m\mathrm{R'} + \mathrm{n}m\mathrm{H}^+ \tag{2.5}$$

In this system, RH is a radical's scavenger, R• is the secondary radical and R' is the deprotonated form of this. The hydrogen and hydroxyl radicals, H• and OH• are direct dissociation results of the ultrasound in the solution, according to Equation 2.2. R• is created when the radicals take possession of the hydrogen of the RH in Equation 2.3, and these react with the metal ions M to form nonvalent metal particles M^0 according to Equation 2.4 and 2.5.

For platinum ions, it has been shown that the reduction of the metal ion can happen following a two-step mechanism, initially reducing Pt^{4+} to Pt^{2+}, and then reducing Pt^{2+} to Pt^0 [13] [15]. This process can then be used to create carbon supported electrocatalysts, as research has shown that ultrasound preparation of the metal particles creates nanosize particles which are well dispersed on the support without altering the structure of said support. Sonochemical production of nanoparticles has multiple advantages when compared to other methods of reducing metals such as platinum. Using $\mathrm{NaBH_4}$ as a reduction agent, for example, gives decent nanoparticles, but the particles sizes are difficult to control without additives, such as surfactants [15]. Furthermore, the surfactants should be removed to ensure that they do not hinder or occupy active sites after nanoparticle generation. Ultrasound thus offers an additive free method with *in-situ* generation of reducing radicals at room temperature and improved control over particle size.

2.3 Methods

2.3.1 Mott-Schottky plots and band edge determination

In a Mott-Schottky diagram, the squared inverse capacitance is measured against the voltage between the electrode surface and bulk electrolyte. The plot can yield information about the flatband potential, if the semiconductor is n-type or p-type, as well as the majority charge carrier density. This is derived from the one-dimensional Poisson's equation for charge density and potential difference in a phase [5]:

$$\frac{\mathrm{d}\phi}{\mathrm{d}x^2} = -\frac{\rho}{\varepsilon\varepsilon_0}$$

where ϕ is the potential difference, ρ is the charge density removed a distance x from the semiconductor-electrolyte junction, ε is the semiconductors dielectric constant and ε_0 is the permitivity of free space. The Mott-Schottky equation can be derived from this by using Boltzmann distribution for electrons in the space charge region and Gauss' law for the electric field within the space charge region to the surface of the interface. The final result is

$$\frac{1}{C^2} = \frac{2}{\varepsilon\varepsilon_0 A^2 e N_\mathrm{D}}\left(V - V_\mathrm{fb} - \frac{k_\mathrm{B}T}{e}\right) \tag{2.6}$$

where C is the capacitance of the semiconductor interface, A is the area of the interface, N_D is the number of donors, V is the external voltage, k_B is the Boltzmann constant, T is the temperature in Kelvin and e is the electronic charge. Thus, when plotting $\frac{1}{C^2}$ against V, extrapolating linearly from the resulting graph to the intercept on the V-axis will yield the V_fb. The slope of this line will give N_D when ε and A are known values. Positive slopes are associated with n-type semiconductors, and negative slopes are associated with p-type semiconductors.

2.3.2 Diffuse light spectroscopy, Tauc-plots and band gap determinations

When illuminating a semiconductor, it will absorb the photon radiation with wavelengths shorter or equal to that of its band gap energy. This absorbance can be measured. The purpose of a Tauc plot is to determine the band gap of a material based on its absorbing characteristics. Consider the relation given below, known as the Tauc relation [16]:

$$(\alpha h\nu)^{1/\mathrm{n}} = K(h\nu - E_g) \tag{2.7}$$

where α is the absorbance coefficient, h is Planck's constant, ν is the frequency of the incident light, n is a factor denoting the nature of the photon transition (direct or indirect semiconductor), K is a proportionality constant, $h\nu$ is the energy of the incident light and E_g is the band gap of the material. The experimental technique yields wavelengths and absorbance data, and thus by plotting $h\nu$ on the horizontal axis and $(\alpha h\nu)^2$ on the vertical axis, one can extrapolate the linear section of the resulting plot to determine its intersection with the horizontal axis. This will be the band gap E_g for a *direct band gap material.* Tauc plots will reveal whether the material is a direct or indirect semiconductor based on the shape of the resulting curve: direct band gap materials have linear extrapolations when the absorbance is squared, while indirect band gap materials show linear sections when taking the square root of the absorbance. It has been shown more explicitly that for direct band gap semiconductors, the absorbance can be written as [17]:

$$\alpha \approx A^* \sqrt{h\nu - E_\mathrm{g}} \tag{2.8}$$

while for an indirect band gap material, the following relation holds true [18]:

$$\alpha \propto \frac{(h\nu - E_\mathrm{g} + E_\mathrm{P})^2}{\exp(\frac{E_\mathrm{P}}{kT}) - 1} \tag{2.9}$$

where E_{P} is the energy of the phonon assisted transition. From these relations, it should be trivial to see that plotting either α^2 or $\alpha^{1/2}$ vs $h\nu$ should give linear sections, and thus one can infer the nature of the transition to be direct or indirect.

2.3.3 Cyclic and Linear Sweep Voltammetry

Cyclic voltammetry is a measuring technique where the voltage is varied for an electrochemical system and the resulting current is measured. It is usually applied in a three-electrode system, where the applied voltage is directed to the working electrode and the subsequent current is the one measured at the working electrode. It is denoted as cyclic due to sweeping the voltage back and forth between an upper and lower potential multiple times to observe if there are any changes in the subsequent voltammograms. Voltammetry is a powerful technique that can give detailed information about diffusion coefficients, reaction mechanisms, reversibility of reactions, electron stoichiometry, active surface area and identification of materials [19]. Figure 2.12a below shows how the voltage is varied with time.

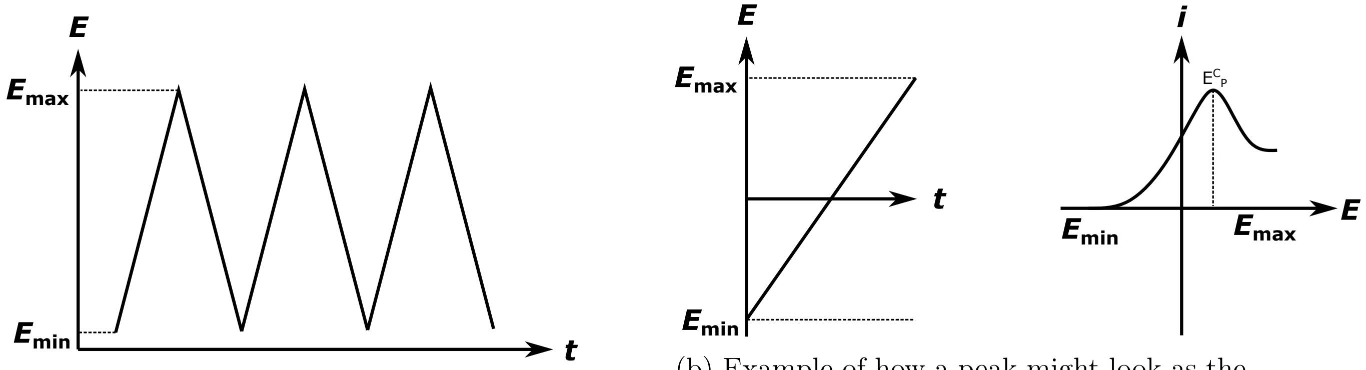

(a) Voltage sweeping pattern. A cycle can be repeated as many times as desired between an upper and lower voltage.

(b) Example of how a peak might look as the voltage is changing with time. Note that the current peak does need to correspond with upper applied voltage.

Figure 2.12: Figures illustrating voltages, time and measured current.

As the voltage increases in Figure 2.12b, the current starts flowing. At these more reactive potentials, the equilibrium for a reversible reaction will be shifted from the reduced species towards the oxidized species, in a manner similar to that of the equations below:

$$\mathrm{O} + \mathrm{e}^{-} \longleftarrow \mathrm{R}$$

$$\ce{O + e- <<=> R}$$

$$\ce{O + e- <=> R}$$

$$\ce{O + e- <=>> R}$$

$$\ce{O + e- -> R}$$

For a fast electron transfer, noticeably faster than the sweep rate, equilibrium will be achieved at all stages. We can consider Nernst Law,

$$E = E^0 + \frac{RT}{nF} \ln \frac{[\mathrm{O}]}{[\mathrm{R}]} \tag{2.10}$$

where E is the applied voltage difference, E^0 is the standard potential, R is the ideal gas constant, T is the temperature, n is the number of electrons in the reaction and [O] & [R] are the concentrations of the species O and R, respectively [20]. With a changing applied voltage, the current at the surface of the electrode starts flowing and traces out a graph similar to that in Figure 2.12b. A peak occurs when, with a sufficiently large diffusion layer, the flux of reactants to the surface of the electrode is not fast enough to satisfy the Nernst equation requirements. Thus the current starts to halt and drop. The rate at which the voltage is varied, is called the scan rate (V/s), and the height of the peaks increase with increased scan rates. With lower scan rates, the diffusion to the electrode is adequate to to satisfy conditions of Nernst equation. During higher scan rates, there is less time for the system to instill an equilibrium.

Linear sweep voltammetry (LSV) works in a similar manner to that of cyclic voltammetry, but the applied potential is not reversed and repeated. Commonly, the sweep rate is also much lower for LSVs than for CVs. LSVs are often in the interval $\nu \in (0\ \mathrm{mV\ s^{-1}}, 20\ \mathrm{mV\ s^{-1}}]$, while CVs are often in the interval $[10\ \mathrm{mV\ s^{-1}}, 500\ \mathrm{mV\ s^{-1}}]$. By visual inspection of CVs and LSVs, one can often deduce at which potentials interesting electrochemical events take place.

A very typical and famous voltammogram is the cyclic voltammogram of a platinum electrode in an aqueous solution, as in Figure 2.13 below.

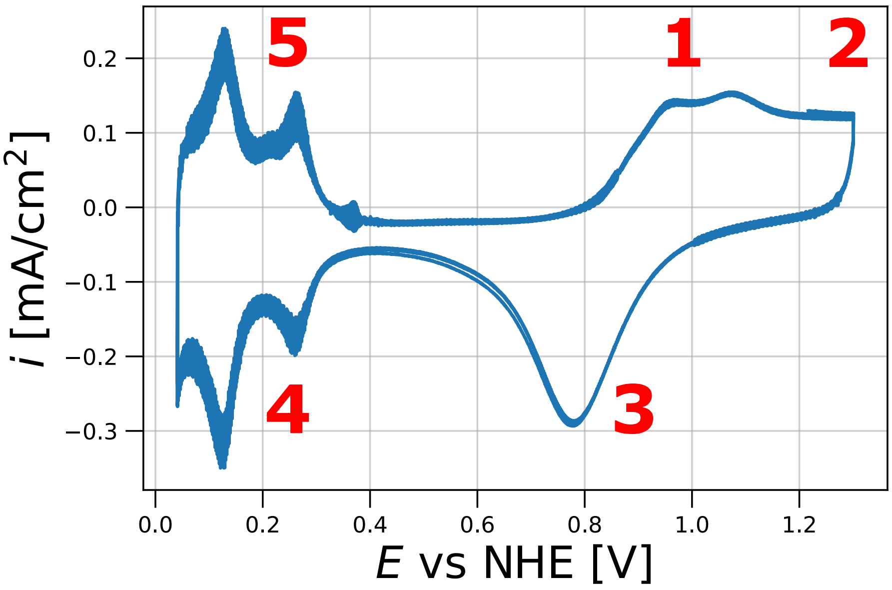

Figure 2.13: A typical cyclic voltammogram for a platinum electrode in aqueous solutions.

Five particularly electrochemically interesting areas are enumerated in the figure, and the events at these locations are as follows:

Peak 1, formation of hydroxide:

$$\mathrm{Pt(s) + H_2O \longrightarrow Pt{-}OH(s) + H^+(aq) + e^-} \tag{2.11}$$

Peak 2, formation of oxide

$$\mathrm{Pt{-}OH(s) + H_2O \longrightarrow Pt{-}O(s) + H^+(aq) + e^-} \tag{2.12}$$

Peak 3, deforming of oxide

$$\mathrm{Pt{-}O(s) + 4\,H^+(aq) + 4\,e^- \longrightarrow Pt(s) + 2\,H_2O} \tag{2.13}$$

Peak 4, adsorption of hydrogen

$$\mathrm{Pt(s) + H^+(aq) + e^- \longrightarrow Pt(s) + H(ads)} \tag{2.14}$$

Peak 5, desorption of hydrogen

$$\mathrm{Pt(s) + H(ads) \longrightarrow Pt(s) + H^+(aq) + e^-} \tag{2.15}$$

2.3.4 Electrochemical impedance spectroscopy

The concept of impedance is very similar to that of resistance for regular electric circuits. For a resistor with direct current (DC), Ohm's law states:

$$E = RI \tag{2.16}$$

where E is the voltage, R is the resistance and I is the current. Impedance is the same concept extended to alternating current (AC):

$$E = ZI \tag{2.17}$$

where Z is the impedance [5]. This means that one can determine the impedance of the system or electrical component by varying the voltage, and measure the subsequent variation in current. The voltage can then be described as

$$E(t) = |E| \sin(\omega t) \tag{2.18}$$

where $|E|$ is the amplitude of the potential and ω is the angular frequency, equivalently written $\omega = 2\pi \cdot f$. The current response will then be

$$I(t) = \sin(\omega t + \theta) \tag{2.19}$$

where θ is the phase shift. This is interpreted as when the potential changes, the current response may trail behind in its response, which is accounted for in this quantity. The impedance can then be written as

$$Z = \frac{E(t)}{I(t)} = \frac{|E| \sin(\omega) t}{\sin(\omega t + \theta)} \tag{2.20}$$

As per Euler's formula applied to these equations,

$$\exp(\mathrm{j}\phi) = \cos\phi + i \sin\phi \tag{2.21}$$

trigonometric functions like these can be represented with real and imaginary parts. The potential may be written as:

$$E_t = E_0 \exp(j\omega t) \tag{2.22}$$

with the current written as

$$I_t = I_0 \exp(j\omega t - \phi) \tag{2.23}$$

All in all, the impedance in complex form can thus be represented accordingly:

$$Z(\omega) = \frac{E}{I} = Z_0 \exp(j\phi) = Z_0(\cos\phi + j\sin\phi) \tag{2.24}$$

with the real and imaginary components being written as:

$$\mathrm{Re}(Z) = Z_0 \cos\phi, \quad \mathrm{Im}(Z) = Z_0 \sin\phi \tag{2.25}$$

Now consider some common electrical components and their impedance representation. A regular resistor is independent of phase changes – it will change its response concurrently and linearly with the input, be that current or voltage. There is no phase shift or *reactive part*. A capacitor has ideally no resistance; they have reactive impedance. The frequency is inversely proportional with the impedance. A capacitor is mathematically represented with

$$Z_C = \frac{1}{j\omega C} \tag{2.26}$$

where j is the imaginary unit. i is not used, in order to avoid confusion with current density, which is often a relevant quantity for experiments of this nature. Note how the impedance of a capacitor is small for high frequencies and large for low frequencies. This becomes important when describing a Randles cell below. Additionally, Nyquist plots should be explained, as they are very common for EIS measurements and are very information dense. These diagrams plot the imaginary part Z_{im} as a function of the real part Z_{re}. This means that quantities that have no imaginary part, *i.e.* no phase dependency, will be strictly plotted on the Z_{re}-axis, which is the case for resistors. Equivalently, ideal capacitors are strictly plotted along the Z_{im}-axis. A single plot on the graph is one impedance measurement for one frequency. A resistor in series with a capacitor will then yield a vertical line displaced proportionally to the resistance of the resistor, with a height proportional to the capacitance of the capacitor.

A Randles cell is a famous RC-circuit for which the setup can be seen in Figure 2.14 [21]. This basic structure is of great importance in many electrochemical systems, as the solution resistance R_{s}, charge transfer resistance R_{ct}, double layer capacitance C_{dl} and a diffusion quantity named Warberg element Z_{W} can be modelled in this way, and any other arbitrary circuit model equivalent of the electrochemical system can be implemented and built upon from this model. In a Nyquist plot (ignoring the Z_{W}), this particular setup will yield a semicircle. This is because at high frequencies, the path of least impedance for electrons will be through the capacitor, which converges towards zero at high frequencies, and at low frequencies it will give high resistance, making the electrons travel through the resistor. At an intermediary frequency, elements of both paths is observed as there is a shift in values for both axis.

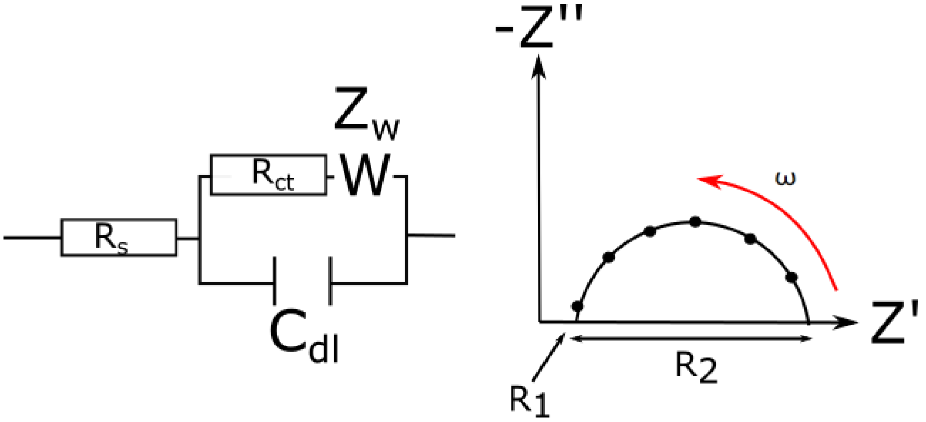

Figure 2.14: A Randles cell and an example of a Nyquist plot. Note that the Warburg element is excluded in the Nyquist plot, as there is no 45° tail leading to the top-right of the illustration.

When retrieving EIS data, one can use software to model an equivalent circuit for the electrochemical system. An infinite amount of systems can potentially be fitted to data, so it is important to be wary of physical interpretation of the applied model. When a model is fitted, one can determine quantities such as the charge transfer resistance, double layer capacitance and ohmic resistance.

2.3.5 XRD – X-Ray Diffraction

X-rays are electromagnetic waves with a wavelength in the magnitude of 10^{-10} m, which is similar to that of atomic and molecular bond lengths and lattice constants. By illuminating a powder sample with X-rays, the light will diffract through the sample, and by consequence of the present lattice planes, crystallography, and quality of the sample, one can determine a range of characteristic data of the sample [22]. XRD analysis is a “fingerprinting technique”. By peak analysis, widths, relative intensities and so forth, one can determine the structure and identity of a sample, for example by comparison with database entries.

2.3.6 EDX – Energy-Dispersive X-Ray Spectroscopy

Energy-dispersive X-ray spectroscopy, or EDX, is a characterization method that that gives information on the elemental composition of a sample [23]. A beam of X-ray radiation is focused on the sample, and the element will interact by either exciting core electrons or remove them all together. When the element relaxes back to its original state, it will emit characteristic X-ray radiation. From this, one can assess the elemental composition of the sample based on the amount and energy of the returning X-rays.

2.3.7 S(T)EM – Scanning (Transmission) Electron Microscopy

Electron microscopes are magnifying devices that can capture images at sub-nanometer resolutions. By using electrons instead of light as the source of illumination, the resulution of the photos are better due to the fact that particles, *i.e.* electrons have shorter wavelengths than photons, following the De Broglie equation [24]. The depth of focus is also improved when using electrons. By using magnetic fields, a system of lenses for magnification can be emulated and give structural insight of the surface of the sample. As the probing particle is an electron, one must be aware of the surface aspects of a sample. Non-conductive species can be coated with carbon to improve resolution, while organic matter can be coated with gold to avoid charging of the surface, which will reduce the quality of the surface imaging.

2.3.8 TGA – Thermogravimetric analysis

Thermogravimetric analysis is an experimental technique which is as simple as it is elegant and useful. The weight of a sample is considered as a function of increased temperature. By assessing how much a sample is reduced in weight at different temperatures, one can evaluate the chemical reactions paths, temperature stabilities, oxidation and evaporation and so forth. Samples in air might increase in weight if oxygen reacts to form oxides on the surface of the sample, while a TGA in argon gas by comparison should not yield such weight increments.

3 Experimental

A flowchart summarizing the production steps of the electrode and material system can be seen in Figure 3.1 below. Note that the top-down direction is the main indicator of the procedural order, while dotted steps indicate alternative production routes that have been investigated in this project, or steps that can be done somewhat interchangeably and still yield results of similar nature.

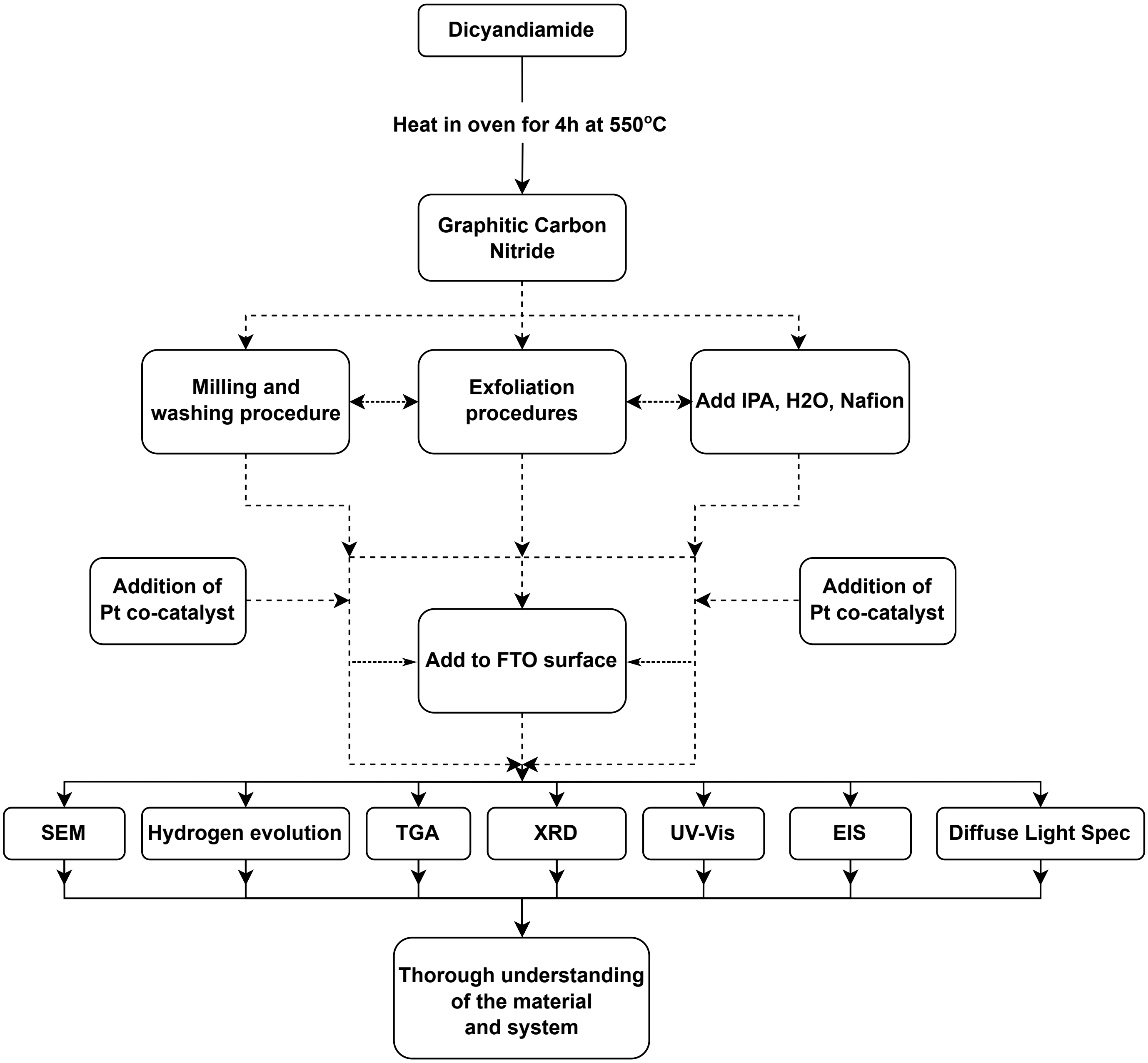

Figure 3.1: Flowchart for the synthesis and characterization of a graphitic carbon nitride electrode.

The following sections will explain in detail how every step was carried out and present relevant instrument data.

3.1 Synthesis of graphitic carbon nitride

Graphitic carbon nitride was prepared by a simple one-step heating process. Granular dicyandiamide in a crucible was inserted as-is into a pre-heated Carbolite CTF 12/65/550 horizontal tube furnace at 550°C for four hours before being quenched in air and cooled to room temperature. The apparatus had a small throughput of synthetic air during the heating process. The resulting powder was then milled to smaller particle sizes. This will throughout this project be referred to as bulk graphitic carbon nitride, or bulk g-C_3N_4.

3.2 Exfoliation of bulk graphitic carbon nitride

3.2.1 Heat exfoliation

Heat exfoliation was performed by inserting bulk g-C_3N_4 into a Carbolite CTF 12/65/550 horizontal tube furnace at room temperature. The g-C_3N_4 may or may not have been washed as per procedure detailed in later chapters prior to exfoliation. The temperature was raised to 500°C with a heat ramp of 5°C per minute and then heated at this temperature for two hours with no throughput of air. The powder was then quenched in air and milled. This will throughout this project be referred to as heat exfoliated graphitic carbon nitride, or heat exfoliated g-C_3N_4.

3.2.2 Ultrasound exfoliation

A solution of 500 mg g-C_3N_4, 150 mL deionized H_2O and 50 mL 96% ethanol was prepared. A 20 kHz QSonica Q700 sonicator system was used on 350 W with a 63 mm probe, where the ultrasound probe was 2.5 cm below the beaker containing the g-C_3N_4-solution. The temperature was regulated with a recirculating chiller from QSonica, which cooled the water that the probe was in direct contact with and that the beaker with g-C_3N_4-solution was placed in. The sonication was continuous for this experiment, and the process lasted for 60 minutes.

This process provides 3 versions of graphitic carbon nitride. Bulk g-C_3N_4 still remains at the bottom of the beaker. By centrifuging the liquid solution (as described in later sections), one gets a yellow powder and a purple-transparent liquid. Both of these contain appreciable amounts of ultrasound exfoliated g-C_3N_4.

3.3 Deposition of platinum with sonochemistry

An aqueous solution of 82 mg g-C_3N_4 and 1.4 mg $PtCl_4$ solution was prepared with deionized water and 0.8 mol dm^{-3} ethanol. The solution was stirred for 10 minutes with an electromagnetic stirrer, and purged for 10 minutes with Ar-gas. A plate transducer was utilized to produce the ultrasound waves, with a frequency of 488 kHz being in direct contact with the solution and graphitic carbon nitride. The solution was isolated from the atmosphere and bubbled with Ar-gas. A cooling jacket was used to regulate the temperature with a water cooler. An ultrasonic amplitude of 100% was utilized, giving approximately 69.5 W of acoustic power to the solution. Other weights of g-C_3N_4 and $PtCl_4$ may be used to achieve different weight percentages.

3.4 Deposition of platinum with NaBH4

0.078184 g g-C_3N_4 and 0.0337 g $PtCl_4$ was added to 50 mL of deionized water and stirred. 5.67 mg $NaBH_4$ was added to a separate vessel with 20 mL of deionized water before being added dropwise to the primary solution under rigorous stirring. This will ideally yield a 20wt% catalyst-cocatalyst system. $NaBH_4$ is added in surplus to ensure that all the platinum is reduced in solution. When the drops are made, the solution should turn dark locally with the production of platinum nanoparticles. Other weights of g-C_3N_4 and $PtCl_4$ may be used to achieve different weight percentages.

3.5 Hydrogen gas production and measurement

A roundbottom flask with 90 mL deionized water and 10 mL 95% methanol was mixed with 50 mg g-C_3N_4, sealed with a septum and stirred with an electromagnetic stirrer while illuminated by an AM1.5 solar simulator. The system was kept at 18°C with a cooled water bath. The atmosphere inside the flask would be analyzed by extracting 1 mL of gas after prolonged solar exposure and inserting this into a gas chromatograph.

3.6 Washing procedure

All washing procedures followed the following steps: liquids containing a powder of interest would be centrifuged at 12 000 rpm for 10 minutes until all powder was retrieved. The liquids were discarded. When bulk amounts of powders were retrieved, they would be transferred to a centrifuge tube with equal volumes of deionized water and 96% ethanol, shaken and centrifuged. The liquids would be discarded and this process would be conducted a total of 3 times. This will be referred to as the washing procedure for this project.

Washing of powders was conducted at different stages of the synthesis to evaluate the effect this had on measured properties. As per Figure 3.2, a washing procedure could be conducted after the initial synthesis of bulk g-C_3N_4, after an exfoliation process, or both. These will be referred to as A powders, B powders or A & B powders, accordingly.

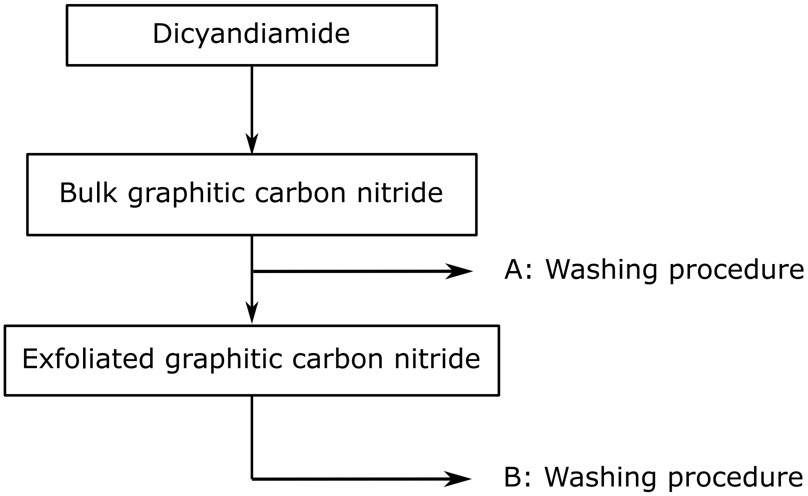

Figure 3.2: Washing procedure scheme of graphitic carbon nitride. Samples washed after the initial synthesis of bulk g-C_3N_4 are denoted as A, samples washed after an exfoliation stage is denoted as B, while samples washed after both synthesis steps are denoted as A & B.

3.7 Preparation of film solution

The as-produced graphitic carbon nitride will not stick to surfaces without an adhesion agent or other forms of processing. It was found that adding 10 mg of graphitic carbon nitride to a mixture of 475 µL water, 475 µL isopropanol and 50 µL Nafion – in that order – alleviates this problem. These values are also shown in Table 3.1. The graphitic carbon nitride was mixed in the solution by 10 minutes of electromagnetic spinner stirring, followed by submerging the solution in a 42 kHz VWR ultrasound bath for a minimum of 30 minutes.

The resulting mixture was drip coated onto a 2x2 cm^2 masked window on a 3x3 cm^2 FTO substrate. This process can be repeated to achieve the desired thickness of the film. The film would need to dry for multiple hours in room temperature for each layer.

Material	Amount
Graphitic carbon nitride	10 mg
Water	475 µL
Isopropanol	475 µL
Nafion	50 µL

Table 3.1: Film solution mixture.

The instrumental methods given below were used on either dried films or directly on the graphitic carbon nitride powder.

3.8 UV-Vis of sonicated samples

The sonication process was initialized at the aforementioned operating conditions, and samples were extracted after 0, 5, 10, 20, 40 and 60 minutes. The samples and consequent color changes can be observed in Figure 3.3 below. Each sample needed to be diluted in order to not max out the cap of the instrument, *i.e.* letting light through so that it could indeed be analyzed. 1 mL of KI was added in excess to every sample so that the remaining Pt^{4+}-ions would create a PtI_6^{2-}-complex, which gives a known peak of 495 nm in the UV-Vis curves.

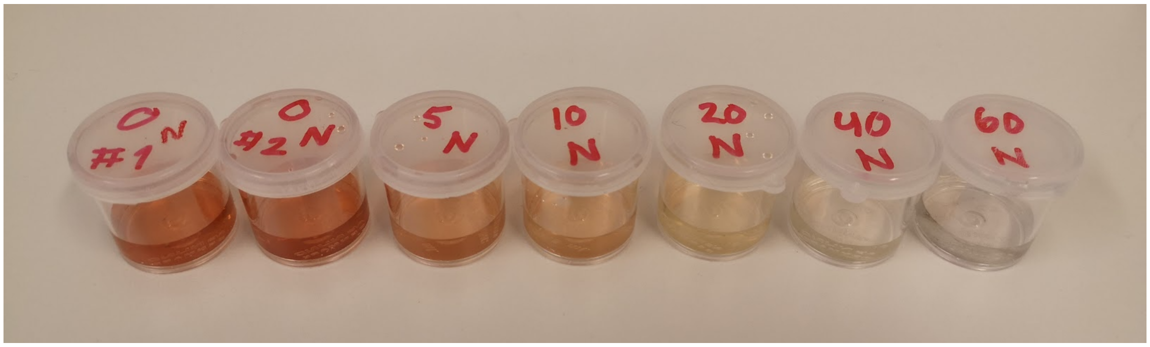

Figure 3.3: Samples of Pt in solution for UV-Vis.

3.9 Instrumentation

3.9.1 UV-Vis of sonicated samples

The UV-Vis samples were analyzed with a Thermo Scientific Evolution 220 UV-Vis spectrophotometer for wavelengths between 200 nm and 800 nm at a scan rate of 100 nm/min.

3.9.2 S(T)EM and EDX

The graphitic carbon nitride with platinum nanoparticles were investigated with a Hitachi High-Tech SU9000 in brightfield mode, with an acceleration voltage of 30 kV and an emission current of 0.7 μA. Elemental characterization was performed with the Oxford Ultim Extreme 120 mm^2 EDS detector.

3.9.3 TGA – Thermogravimetric analysis

A NETZSCH STA F3 449 Jupiter was used to analyze both the chemical reaction path from dicyandiamide to graphitic carbon nitride. Dicyandiamide was heated from 25°C to 550°C with a heating rate of 10°C min^{-1}. This temperature was held for 240 minutes. The temperature was then raised to 650°C for one hour to burn off the remaining powder. The temperature was then lowered to 25°C. All steps had an air gas flow of 20 mL min^{-1}.

3.9.4 XRD – X-Ray Diffraction

For all samples, a Cu-K$_\alpha$ Bruker D8 A25 DaVinci X-ray Diffractometer with Lynx-Eye™ Super-Speed Detector and 90 position sample changer was used. Bragg-Brentano geometry, θ-θ operating mode, 2.5° primary and secondary Soller slits and a V6 variable divergence slit were utilized. A step length of 0.010° per step was used from 10° to 80°.

3.9.5 Diffuse light spectroscopy and Tauc plots

A UV-Vis spectroscopy setup equipped with an integrating sphere was used. The samples were investigated by placing the absorbance measuring device directly on top of the samples, while also correcting for any background noise. The absorbance was measured as a function of wavelength, from approximately 200nm to 1300nm with a monochromator.

3.9.6 Electrochemical measurements: CV, LSV, EIS and Mott-Schottky

A three electrode setup was used for all measurements. Each experiment was conducted with EC-Lab software from BioLogic, with voltage ranges and amount of measurements for each experiment as detailed in each respective figure. The experiments were conducted in 1 M H_2SO_4. Ag/AgCl was used as the reference electrode. The investigated films were drip coated on glassy carbon electrodes, which rotated at 1600 rpm during experiments. For the Mott-Schottky analysis, the scan frequencies were 1 kHz, 1.7 kHz and 3 kHz, and the sine amplitude V_a was set to 10 mV.

3.9.7 Photocurrent measurements

A Zahner XPot external potensiostat was utilized with a Zahner PECC photoelectrochemical cell with a transparent window in the front which lets light from the CIMPS LED potentiostat radiate directly at the sample. The light intensity used in this project was mainly 75 W m^{-2}, and the electrolyte was 1.0 M Na_2SO_4.

4 Results

4.1 Color changes after heat exfoliation

Figure 4.1 below shows two samples of graphitic carbon nitride. The sample on the left is pristine, bulk g-C_3N_4, while the sample on the right is heat exfoliated. The vials contain approximately equal volumes of g-C_3N_4, but the heat exfoliated sample weighs 46% less than the pristine bulk g-C_3N_4.

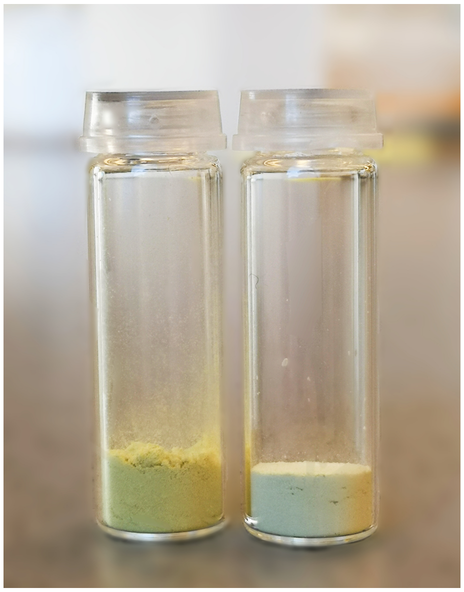

Figure 4.1: Bulk graphitic carbon nitride on the left and heat exfoliated g-C_3N_4 on the right. Though similar in volume, the exfoliated powder weighs 46% less than the bulk sample.

It is evident that the exfoliated sample has lost most of the characteristic yellow color. Furthermore, although the vials have similar volumes, their weights differ tremendously. The weight of the powder in the left vial is 0.2643g, while the other weighs 0.1440g, making the exfoliated sample 46% lighter. The color change and weight reduction is in accordance to literature [26].

4.2 XRD

Figure 4.2 below shows an XRD diffractogram with values ranging from 0^o to 80^o on the horizontal axis and arbitrary units of absorption on the vertical axis. The two measurements in the figure are for bulk graphitic carbon nitride and heat exfoliated graphitic carbon nitride. It is observed that the heat exfoliated sample has shifted its main peak one degree to the right, which is a sign of successful exfoliation [26]. The two peaks correspond to the stacked layers of graphitic carbon nitride and the in-plane repeating unit, correspondingly at 27^o and 13^o [25].

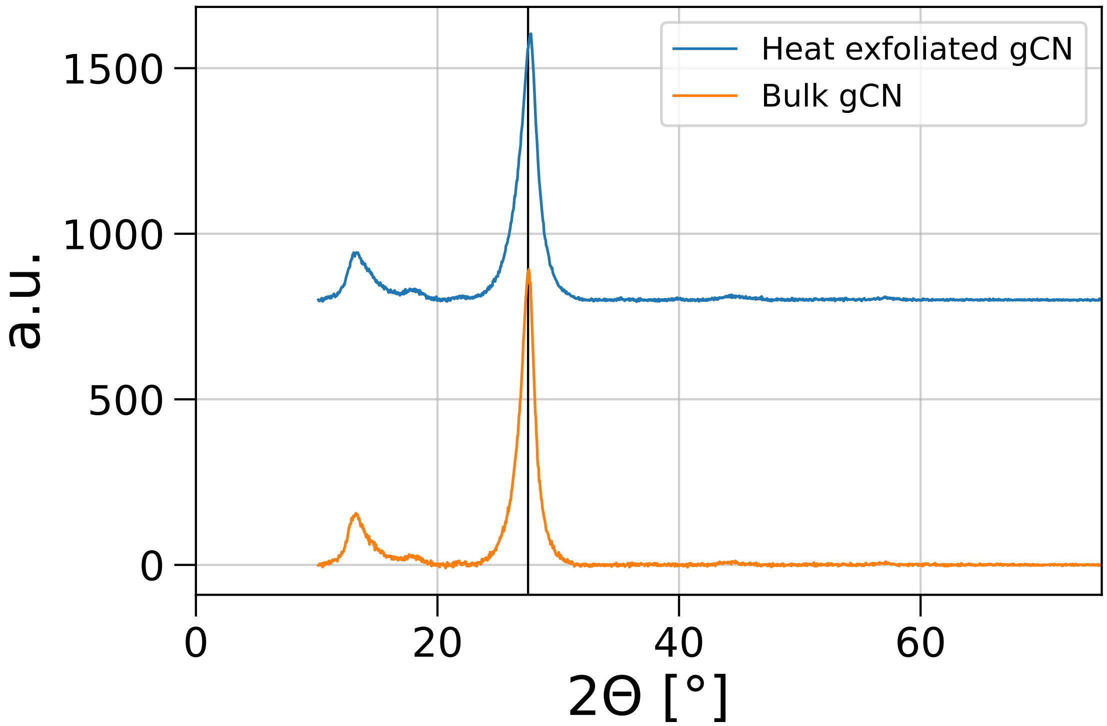

Figure 4.2: X-ray diffractogram of heat exfoliated graphitic carbon nitride and bulk g-C_3N_4. It is observed that the main peak of the heat exfoliated sample has shifted one degree to the right in the diagram, indicating exfoliation.

4.3 UV-Vis for platinum reduction on graphitic carbon nitride

Figure 4.3 below shows the absorbance in arbitrary units along the vertical axis and the irradiated wavelengths along the horizontal axis for UV-Vis curves taken at different time intervals during an ultrasound platinum deposition process. The sample taken at 0 minutes of ultrasonication shows the most intense peak at 495 nm, indicating the largest presence of Pt^{4+} in all of the measurements. For each subsequent measurement in time, this peak disappears virtually completely, showing that after 40-60 minutes of ultrasonication, no Pt^{4+} was in the ultrasonicated solution. Peaks at 388 nm are among others attributed to Pt^{2+} [15]. The data shows that after 60 minutes, there is virtually no Pt^{2+} in solution, strongly suggesting that all platinum ions have been reduced to metallic platinum. The data series for the sample taken at 60 minutes show that there is virtually no deviation from the background measurement, indicating that there are almost no absorbing particles or ions in solution after 60 minutes of ultrasonication. Note that for the graph at 0 minutes, the tail ends of neighboring peaks overlap with the expected peak area for Pt^{2+}. This is not a confirmation of the presence of Pt^{2+}, and needs to be considered when doing the data analysis.

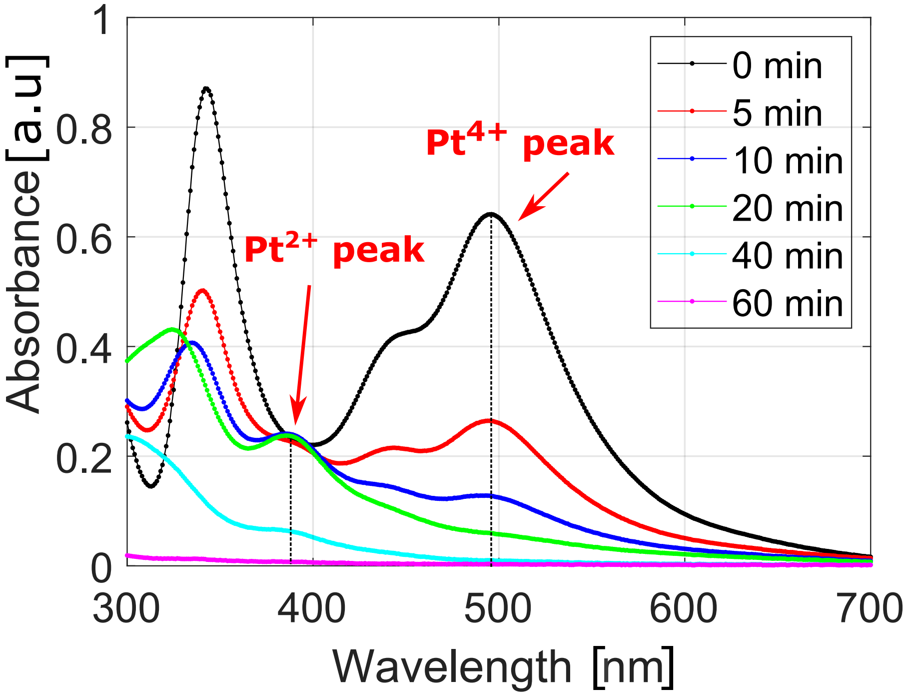

Figure 4.3: UV-Vis of Pt reduction. The peak at 495 nm, belonging to the Pt^{4+}-ion, gradually disappears for increased sonication times. Peaks at 388 nm first rise, then fall with increased time. After 60 minutes, virtually no ions are detected in the solution.

The graphs in Figure 4.4 below show different quantifications of ions and particles as calculated from the data in Figure 4.3. Figure 4.4a shows the calculated mass of solid platinum particles developed in milligrams on the vertical axis and the measured time in minutes on the horizontal axis for two experiment runs. The red markers show the development of Pt(s) production with graphitic carbon nitride in solution, while the blue markers show the mass of Pt(s) without g-C_3N_4 in solution. It shows that platinum reduces faster and more when g-C_3N_4 is present during the ultrasonication.

This might indicate that graphitic carbon nitride helps catalyze the reduction of platinum.

Figure 4.4b shows the calculated concentrations of Pt^{2+} in millimolar on the vertical axis and the measured time in minutes on the horizontal axis for two experiment runs. The red markers show the development of Pt^{2+} with graphitic carbon nitride present in solution, while the blue markers show the concentration of Pt^{2+} without g-C_3N_4 in solution. It it observed that for the first 20 minutes, there is more Pt^{2+} in solution for the g-C_3N_4 sample, while after 20 minutes there is a smaller concentration of Pt^{2+} in solution. This could imply that graphitic carbon nitride initially aids the reduction of Pt^{4+} into Pt^{2+} the first 20 minutes, and also further contributes to reducing Pt^{2+} into Pt(s) for the remainder of the experiment run.

Figure 4.4c shows the normalized concentration of Pt^{4+} along the vertical axis and the eloped time in minutes along the horizontal axis for two experiment runs. The red markers show the development of Pt^{4+} with graphitic carbon nitride present in solution, while the blue markers show the concentration of Pt^{4+} without g-C_3N_4 in solution. It is observed that when normalizing the results, the differences between the two systems virtually disappear, so the basis to claim that g-C_3N_4 speeds up the process is reduced from this result. However, it could be mentioned that the transition from Pt^{4+} to Pt^{2+} most likely will not be sped up by the presence of g-C_3N_4, but for the solidification process of Pt^{2+} to Pt(s), there will be some level of energy barriers related to the nucleation of nanoparticles. These may be catalyzed by having an active surface area present, such as g-C_3N_4. Thus the Pt^{4+} reduction is identical in the two systems, but the Pt^{2+} reaction could, and is indeed, somewhat faster in the system which has g-C_3N_4 present in solution, as can also be spotted in 4.4b.

Figure 4.4d shows the calculated concentrations of the three different forms of platinum measured in millimolar along the vertical axis and the eloped time in minutes along the horizontal axis with graphitic carbon nitride present in all solutions. The red markers show the development of Pt^{4+}, the blue markers show the concentration of Pt^{2+}, while the green markers show the concentration of metallic Pt in solution. Initially, there is only Pt^{4+}. As Pt^{4+} rapidly decreases in concentration, primarily Pt^{2+} concentrations but also Pt(s) increases. This trend continues for all samples up until and including 20 minutes. After 40 minutes, the concentration of Pt^{2+} decreases greatly, the concentration of Pt^{4+} is virtually non-present and the concentration of Pt(s) continues to rise. After 60 minutes, there is only negligible amounts of of Pt^{4+} and Pt^{2+}, but appreciable amounts of Pt(s). This strongly indicated that all the platinum ions have been reduced to solid platinum.

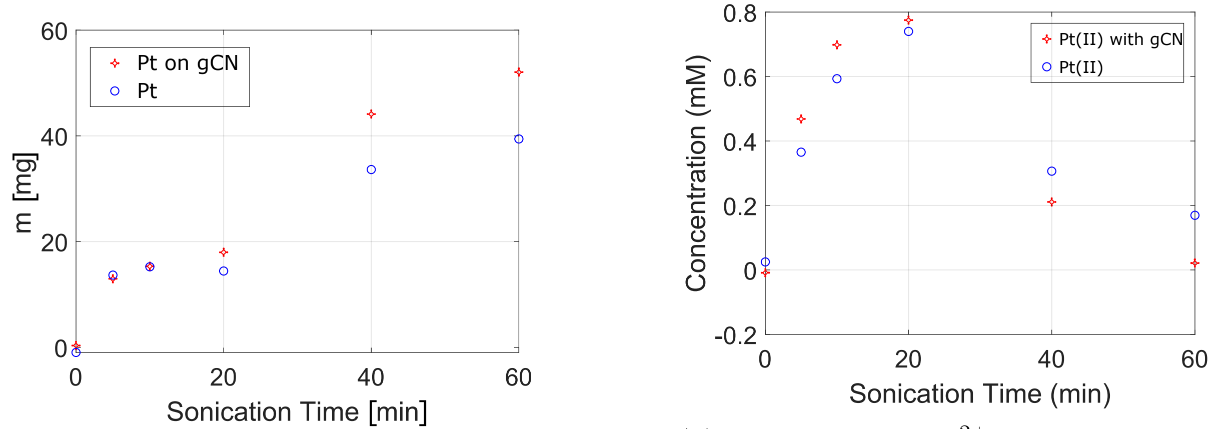

(a) Development of Pt(s) in solution with and without g-C_3N_4. The sample with g-C_3N_4 produces Pt(s) faster than the solution without, possibly indicating that g-C_3N_4 helps catalyze the reduction of Pt-ions.

(b) Development of Pt^{2+} in solution with and without g-C_3N_4. The sample with g-C_3N_4 first produces Pt^{2+} faster than the solution without, and then further reduces these faster than the solution without g-C_3N_4, possibly indicating that g-C_3N_4 helps catalyze the reduction of Pt-ions.

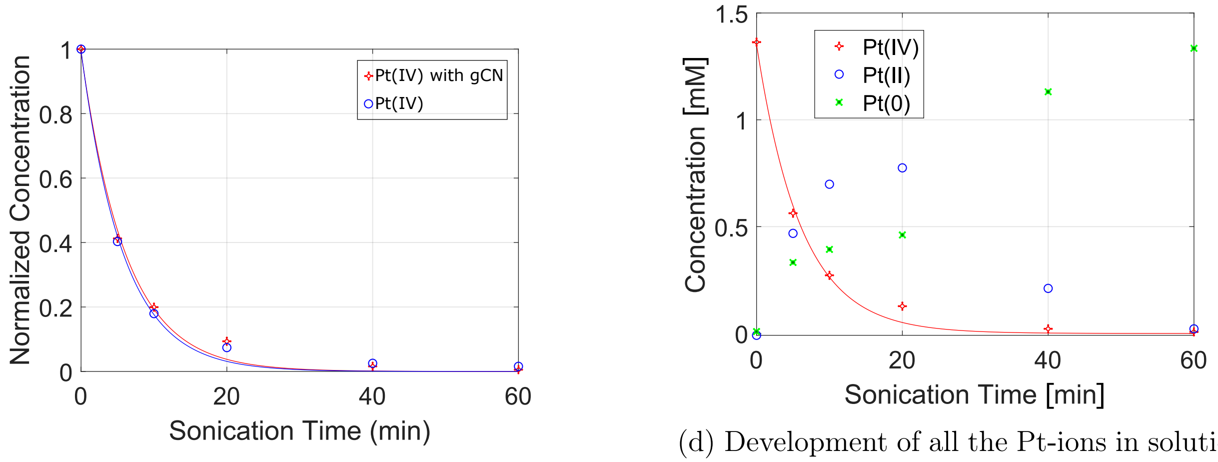

(c) Development of Pt^{4+} in solution with and without g-C_3N_4. The normalized graphs show that there are virtually no differences between the two runs.

(d) Development of all the Pt-ions in solution with g-C_3N_4. The results show that at first, there is only Pt^{4+} in solution, before producing Pt^{2+} and Pt(s). After 60 minutes, virtually all of the ions have been reduced to metallic platinum.

Figure 4.4: Calculated data for all the Pt-ions based on the UV-Vis measurements. The data shows that after 60 minutes of ultrasonication, virtually all the platinum is reduced into solid Pt.

4.4 TGA

The results in Figure 4.5 below indicate the reaction path and thermal stability for graphitic carbon nitride, with the temperature in °C on the horizontal axis and the change in weight percentage along the vertical axis. For dicyandiamide, the first significant drop-off in weight is around 240°C. This is attributed to volatilization of amino groups, moisture, impurities and the subsequent condensation to melamine [27]. Tri-s-triazine, the monomer of the polymeric graphitic carbon nitride is produced at 340°C, and these polymerize to graphitic carbon nitride around 550°C.

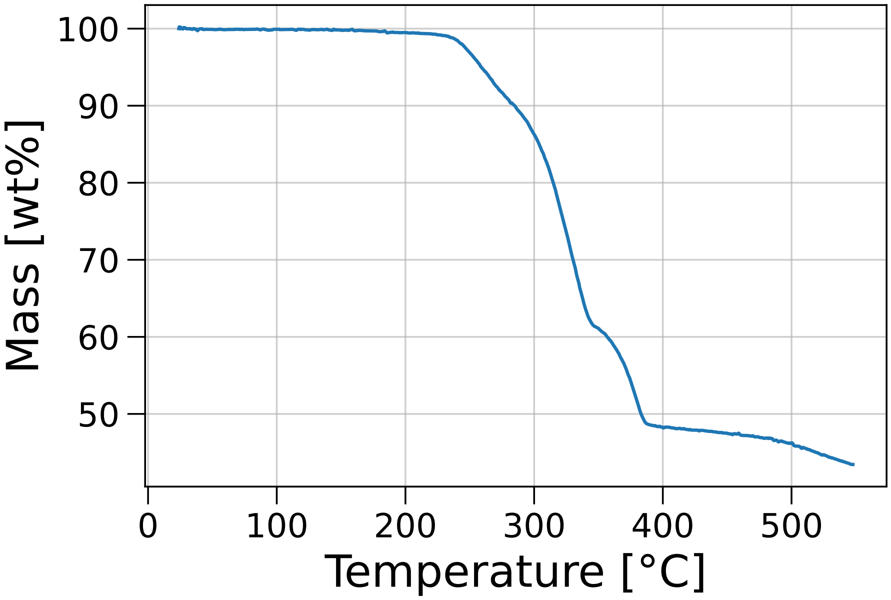

Figure 4.5: TGA of dicyandiamide to graphitic carbon nitride. The changes in weight percentage happen at temperature intervals that fits with reported values in literature.

4.5 Cyclic Voltammetry, Linear Sweep Voltammetry and Electrochemical Impedance Spectroscopy

4.5.1 Graphitic carbon nitride without co-catalysts

Figure 4.6 below is a cyclic voltammogram of bulk and exfoliated graphitic carbon nitride in a 1 M H_2SO_4 solution in the voltage range of -0.2 V to 1.4 V relative to the Ag/AgCl reference electrode with a scan rate of 100 mV/s. The heat exfoliated sample demonstrates currents as much as fives times larger than the bulk sample. Their shapes are similar, but the heat exfoliated sample has more pronounced areas of interest. Similarly for the ultrasound exfoliated sample, the current peaks are more pronounced and around twice as large than for the bulk sample.

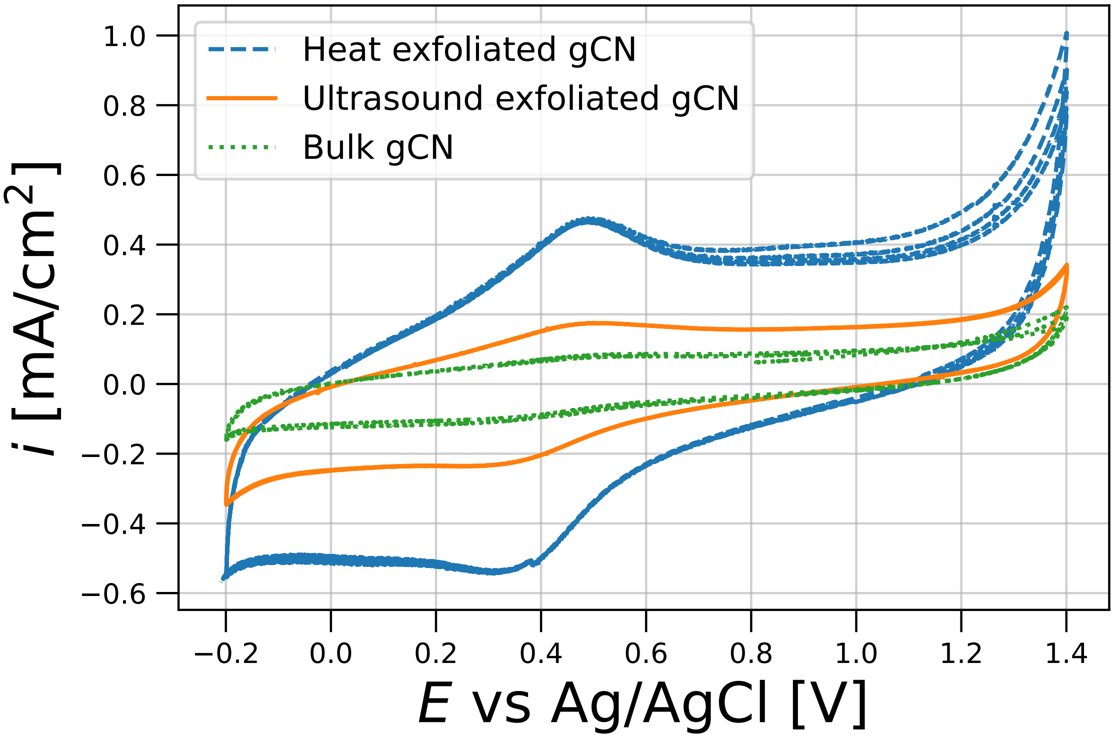

Figure 4.6: Cyclic voltammograms of bulk and exfoliated graphitic carbon nitride. The heat exfoliated sample is consistently reading at values five-fold larger than that of the bulk sample, while the ultrasound exfoliated sample has approximately twice as large currents.

Figure 4.7 below is a linear sweep voltammogram of bulk and exfoliated graphitic carbon nitride in a 1 M H_2SO_4 solution in the voltage range of -0.1 V to -0.4 V relative to the Ag/AgCl reference electrode with a scan rate of 2 mV/s. The heat exfoliated sample demonstrates currents more than twice as large as the bulk sample, while the ultrasound exfoliated sample shows currents almost ten times larger than that of the bulk.

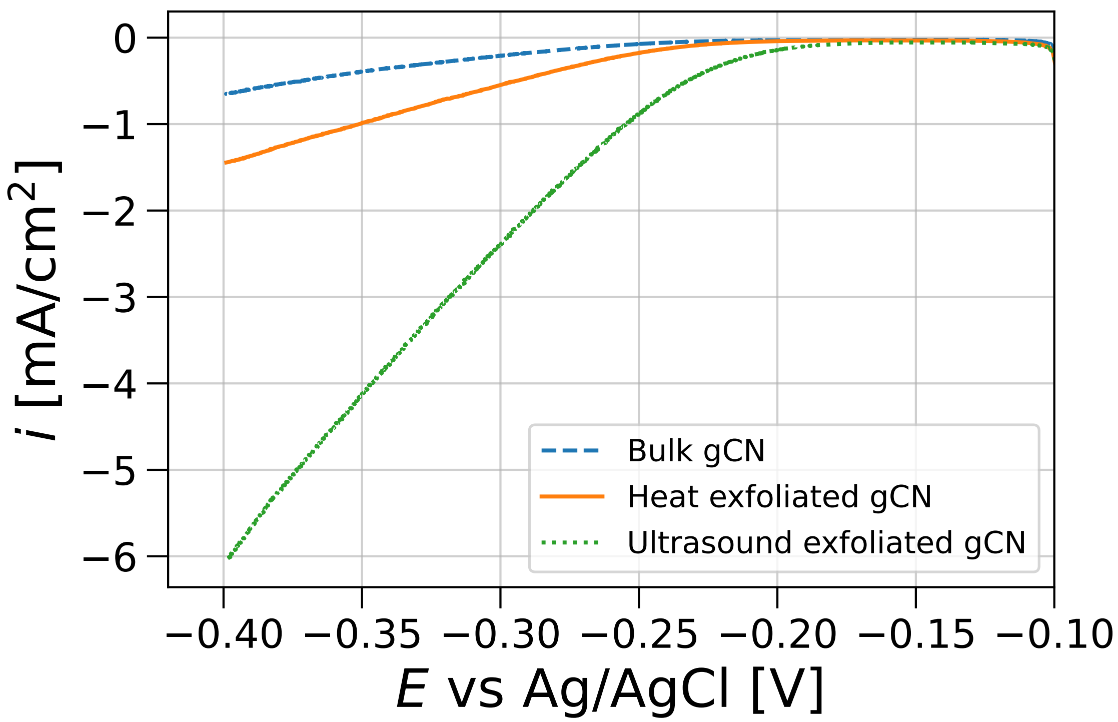

Figure 4.7: Linear sweep voltammograms of bulk and exfoliated graphitic carbon nitride. The heat exfoliated sample is consistently reading at values twice than that of the bulk sample. The ultrasound exfoliated sample reaches currents almost 10 times larger than that of bulk.

Figure 4.8 below is an EIS of bulk and exfoliated graphitic carbon nitrides in a 1 M H_2SO_4 solution in the frequency range 1 mHz to 100 kHz. The diameter of the semicircle corresponding to the heat exfoliated sample is half of that of the bulk sample, while the ultrasound exfoliated sample is half of that diameter.

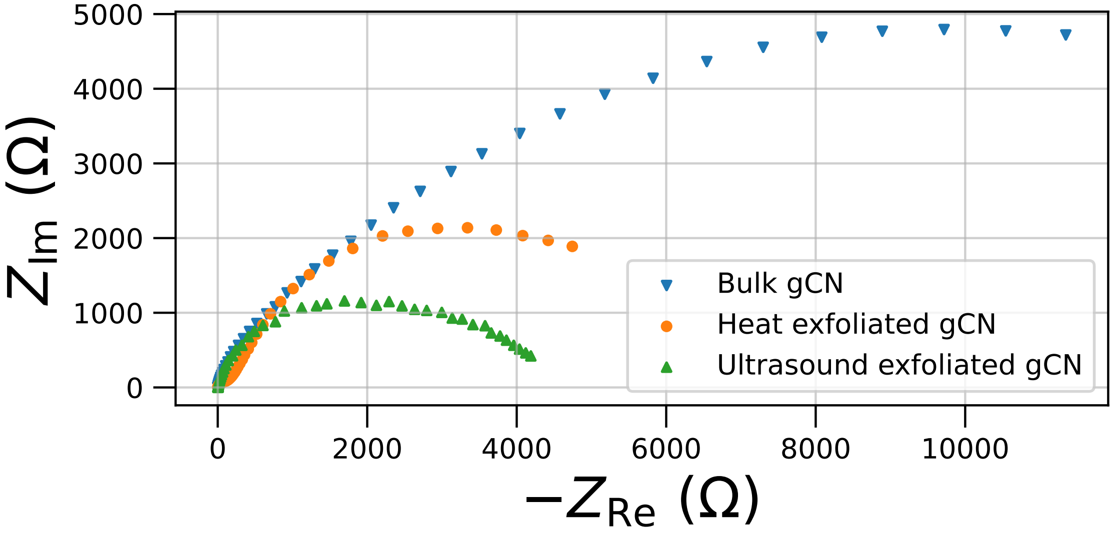

Figure 4.8: EIS of bulk and exfoliated graphitic carbon nitride. The radius of the ultrasonicated sample semicircle is the smallest, being half of the heat exfoliated semicircle radius size. The bulk radius is twice as large as this again.

4.5.2 Graphitic carbon nitride with platinum as co-catalyst

Figure 4.9 below is a cyclic voltammogram of bulk graphitic carbon nitride (C), ultrasonicated g-C_3N_4 (B) and ultrasonicated g-C_3N_4 with 1wt% Pt from an ultrasound deposition (A). The experiments were run in a 1 M H_2SO_4 solution in the voltage range of -0.2 V to 1.4 V relative to the Ag/AgCl reference electrode with a scan rate of 100 mV/s. Bulk g-C_3N_4 has the lowest currents and least pronounced peaks, while the sample with 1wt% Pt outperforms bulk and ultrasonicated g-C_3N_4 by a factor of 6 and 2 respectively towards the lower voltage range. It is observed that the sample with platinum has a drastic spike in current towards the hydrogen evolution area.

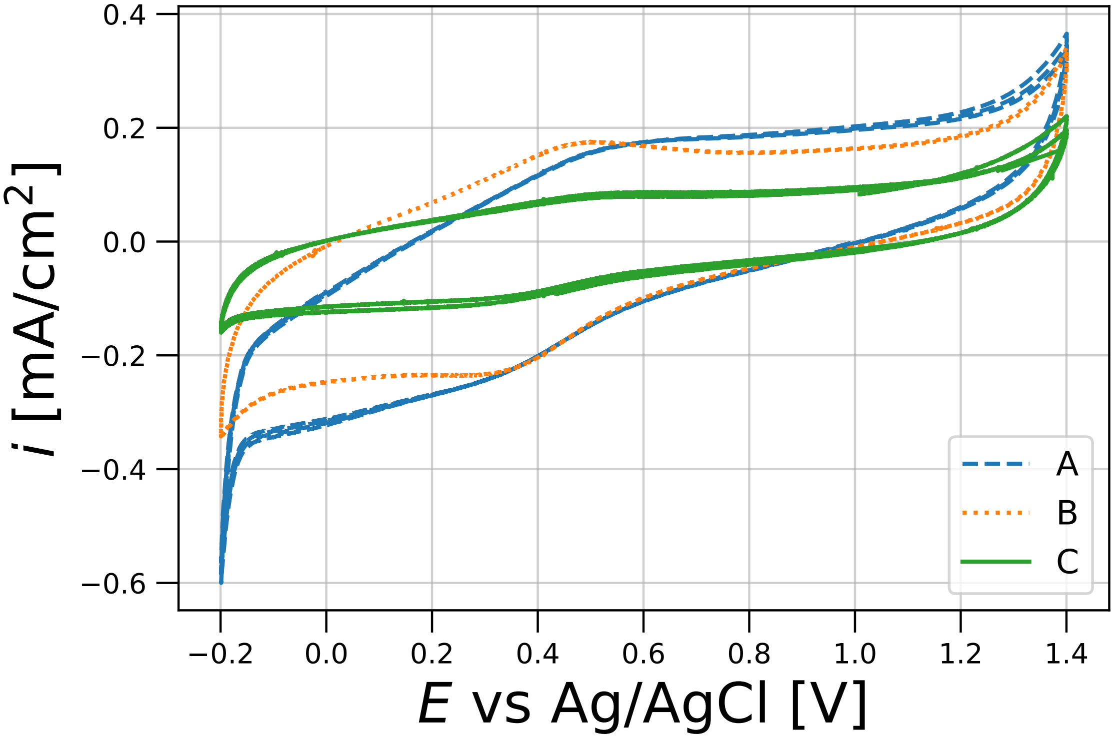

Figure 4.9: Cyclic voltammograms of bulk and exfoliated graphitic carbon nitride. (A) shows ultrasound exfoliated g-C_3N_4 with 1wt% Pt from an ultrasonication. (B) shows ultrasound exfoliated g-C_3N_4, while (C) shows bulk g-C_3N_4. The ultrasound exfoliated sample is reading at values twice than that of the bulk sample in the hydrogen evolution area. The ultrasound exfoliated 1wt% Pt sample reaches currents more than 3 times than that of bulk in the hydrogen evolution area.

Figure 4.10 below is a cyclic voltammogram of bulk graphitic carbon nitride, bulk g-C_3N_4 with 20wt% Pt from $NaBH_4$ reduction and bulk g-C_3N_4 with 20wt% Pt from an ultrasound deposition. The experiments were run in a 1 M H_2SO_4 solution in the voltage range of -0.2 V to 1.4 V relative to the Ag/AgCl reference electrode with a scan rate of 100 mV/s. Bulk g-C_3N_4 has the lowest currents and least pronounced peaks, and is perceived as virtually flat when compared to the other two samples. The bulk sample with Pt from $NaBH_4$ shows a voltammogram of similar nature to that of the pure platinum electrode, but with especially strong hydrogen production peaks. The bulk sample with Pt from ultrasonication shows a voltammogram also of similar nature to that of the pure platinum electrode, but with especially strong hydrogen production peaks, as well as more pronounced desorption of hydrogen peaks.

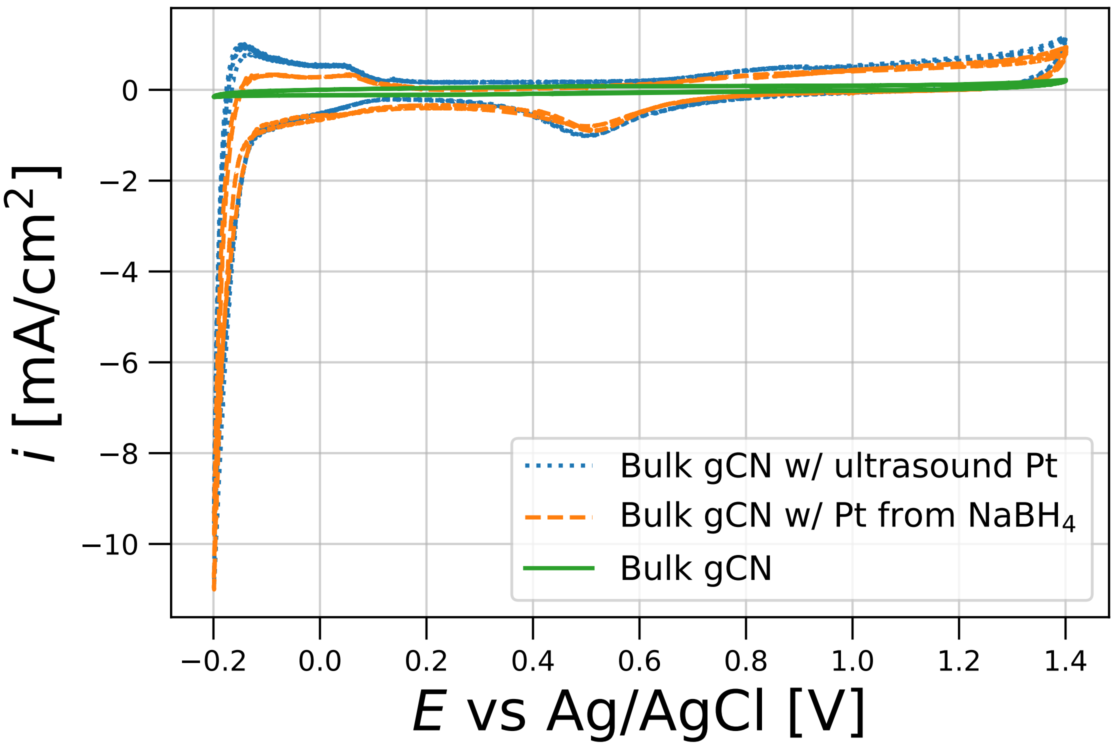

Figure 4.10: CV of bulk and exfoliated gCN with Pt. The voltammogram shows that the bulk g-C_3N_4 does very poorly electrochemically when compared to any sample that has platinum on it. Both the ultrasound-Pt sample and $NaBH_4$-Pt greatly outperforms the bulk sample, with ultrasound-Pt giving better results for the desorption of hydrogen as well.

Figure 4.11 below is a linear sweep voltammogram of bulk graphitic carbon nitride without Pt, ultrasound exfoliated g-C_3N_4 with 1% Pt, bulk g-C_3N_4 with 20wt% Pt from $NaBH_4$ and with 20wt% Pt from ultrasound. The measurements were made in a 1 M H_2SO_4 solution in the voltage range of -0.1 V to -0.4 V relative to the Ag/AgCl reference electrode with a scan rate of 2 mV/s. The bulk sample without platinum shows virtually no electrochemical activity in relation to the 20wt% samples. The 1wt% sample shows some increase in current densities at the lowest voltage, 12 times larger than that of the bulk sample. The $NaBH_4$ sample reaches current densities 235 times larger than the bulk without platinum, and the sample with 20wt% Pt from ultrasound shows current densities 292 times larger than the bulk without platinum. These results are also summarized in Table 4.1.

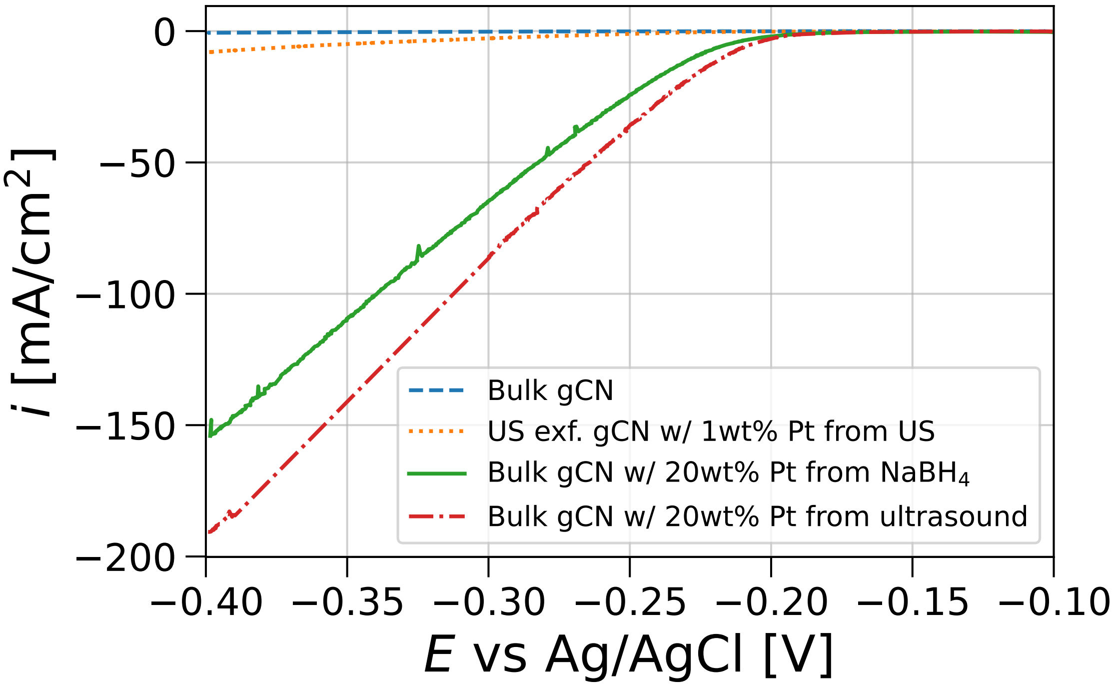

Figure 4.11: CVs of graphitic carbon nitrides with different amounts of Pt and Pt deposition method. It is evident that large weight percentages of platinum dramatically increases the current densities, but a small amount of 1wt% is also beneficial to the electrochemical properties.

	Bulk gCN	1wt% Pt	NaBH$_4$-Pt gCN	Ultrasound-Pt gCN
i at -0.4V [mA cm^{-2}]	-0.654	-8	-154	-191
Relative to bulk	1	12	235	292

Table 4.1: Current densities at -0.4V vs NHE

Figure 4.12 below is an EIS of bulk g-C_3N_4 with platinum from NaBH$_4$ and ultrasound in a 1 M H_2SO_4 solution in the frequency range 1 mHz to 100 kHz, showing the negative real impedance measured in ohms along the horizontal axis and the imaginary component measured in ohms along the vertical axis. The two samples show similar EIS results, with each of them distinctly having two semicircles of similar magnitudes. An equivalent circuit fitting of this system, for example with two Randles cells in series, would give numerical data that would show that the charge transfer resistances of the graphitic carbon nitride and the platinum would be of similar magnitude at this specific applied potential.

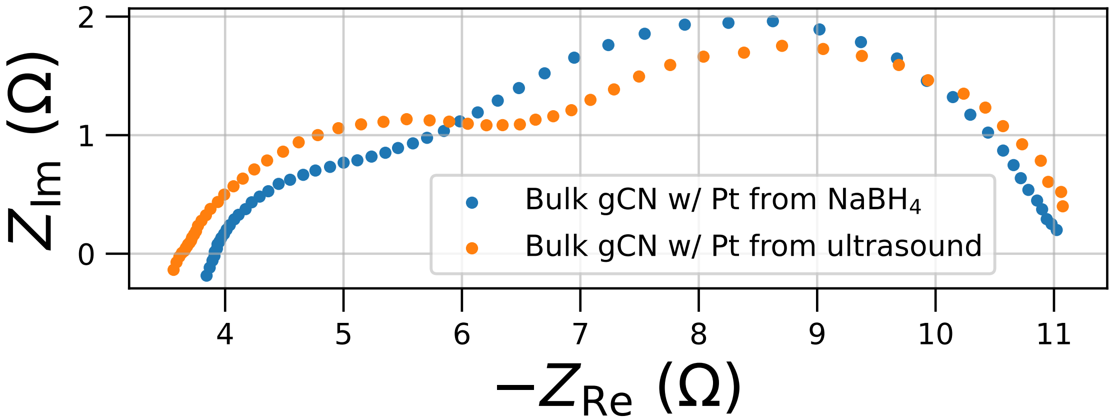

Figure 4.12: EIS of bulk g-C_3N_4 with Pt from two different deposition methods. The similar dimensions for the two samples show that they have similar charge transfer resistances, and that the system could reasonably be interpreted to be dependent on the charge transfer resistance of the g-C_3N_4 and the platinum as two different faces for charge transfer.

Figure 4.13 below is a cyclic voltammogram of different graphitic carbon nitrides with 20wt% platinum deposited with ultrasonication. The experiments were run in a 1 M H_2SO_4 solution in the voltage range of -0.2 V to 1.4 V relative to the Ag/AgCl reference electrode with a scan rate of 100 mV/s. The bulk and the heat exfoliated g-C_3N_4 samples show similar voltammograms. However, the ultrasound exfoliated sample with ultrasound deposited Pt shows a tremendous similarity to that of the standard platinum electrode in an aqueous solution. It is evident that the combination of ultrasound exfoliation and ultrasound deposition creates a catalyst-cocatalyst system which is able to utilize the available platinum for electrochemical properties to a much larger extent than the other samples created.

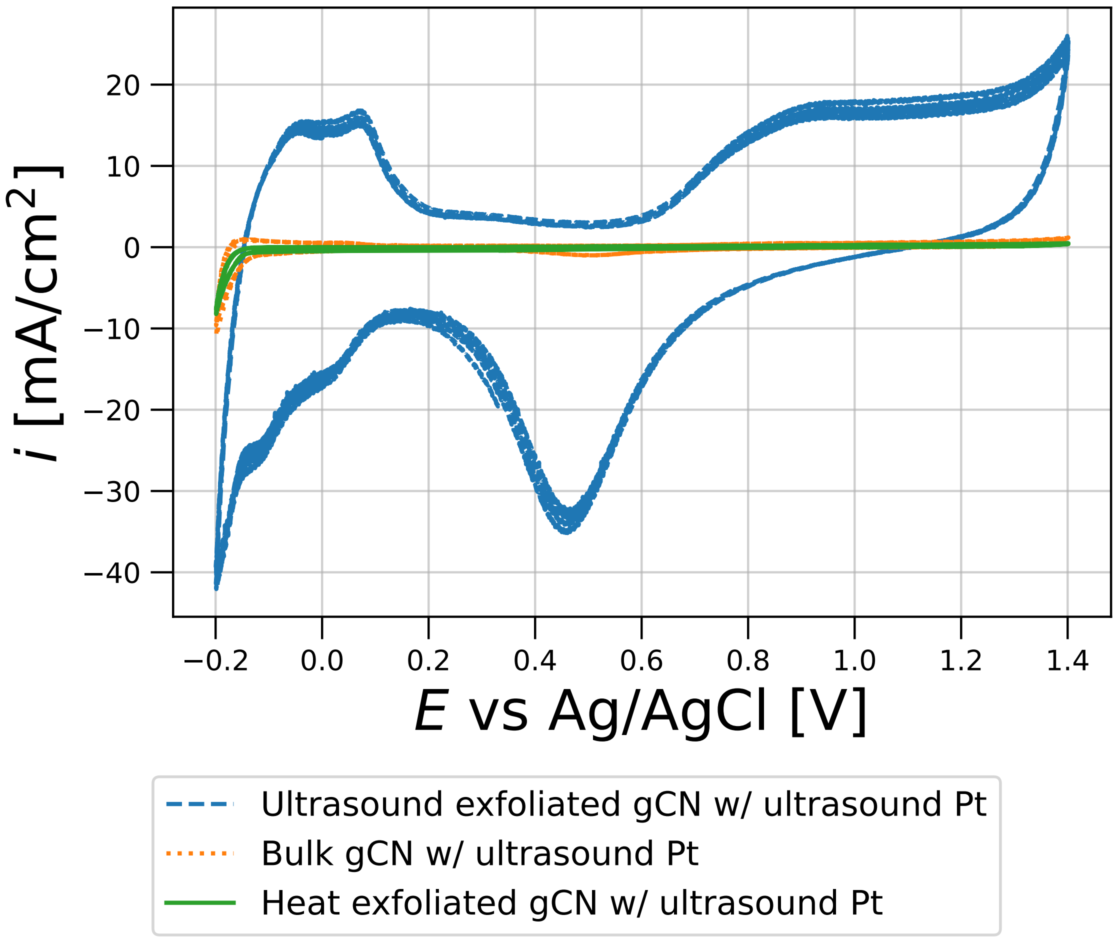

Figure 4.13: CV of different nitrides with ultrasonicated platinum. The ultrasound exfoliated sample with ultrasound Pt has a striking similarity to that of the platinum electrode in aqueous solutions, and has far superior current densities when compared to the other samples in this run.

Figure 4.14 below shows the EIS of bulk g-C_3N_4, ultrasound exfoliated g-C_3N_4, ultrasound g-C_3N_4 with 1wt% Pt from ultrasonication, and ultrasound exfoliated g-C_3N_4 with 20wt% Pt from ultrasonication. The measurements were made in an 1 M H_2SO_4 solution in the frequency range 1 mHz to 100 kHz, showing the negative real impedance measured in ohms along the horizontal axis and the imaginary component measured in ohms along the vertical axis. All of the resulting graphs show semicircle behavior, where the diameter of the semicircles drastically reduces in magnitude for each improvement in production parameters. It is observed that the bulk g-C_3N_4 has the largest, and thus worst, charge transfer resistance of all the measured samples by far. When exfoliated by ultrasound, the charge transfer resistance is drastically reduced by nearly an order of magnitude. With 1wt% Pt on these improved samples, the charge transfer is reduced by an appreciable manner again. With 20wt% Pt, the charge transfer resistance has fell by nearly 3 orders of magnitude when compared to the bulk sample with no platinum. This shows that the charge transfer resistances neatly decreases with the expected pattern, and that each subsequent production parameter presented here leads to better electrochemical activities than the previous version.

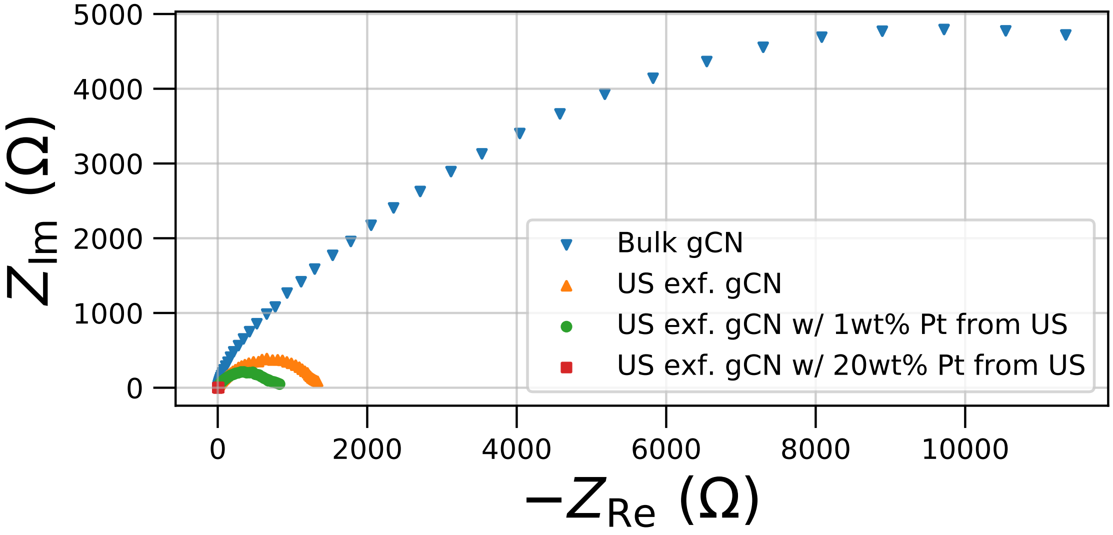

Figure 4.14: EIS of graphitic carbon nitrides with gradual improvements in production parameters. Whereas it is observed that the bulk g-C_3N_4 has the largest semicircle behavior in the plot, the ultrasound exfoliated sample with 20wt% Pt has a semicircle diameter which is three orders of magnitude smaller. The samples showing intermediary results follow an expected order, with exfoliated samples being better than bulk samples, and exfoliated samples with 1wt% Pt showing better results than that as well.

4.6 Effects of the washing procedure

Note first Figure 3.2 from the Methods chapter, which indicates that samples noted with "A" are washed after the primary fabrication of the bulk powder, samples noted with "B" are washed after heat exfoliation, and samples noted with "A & B" are samples that are washed once for every step.

Figure 4.15 below is a linear sweep voltammogram of graphitic carbon nitrides with different washing procedures and exfoliation. The measurements were made in a 1 M H_2SO_4 solution in the voltage range of -0.1 V to -0.4 V relative to the Ag/AgCl reference electrode with a scan rate of 2 mV/s. It shows that the two samples that perform the worst, are the samples that have been washed after the exfoliation step. The best performing sample was washed only after the initial synthesis of bulk g-C_3N_4. The sample that was washed both after the initial synthesis step and the exfoliation performed better than the one only washed after the exfoliation. This shows that washing after the primary heating step benefits the electrochemical properties of the material, presumably by removing all remaining precursors before exfoliation, leading to a more exfoliated end result.

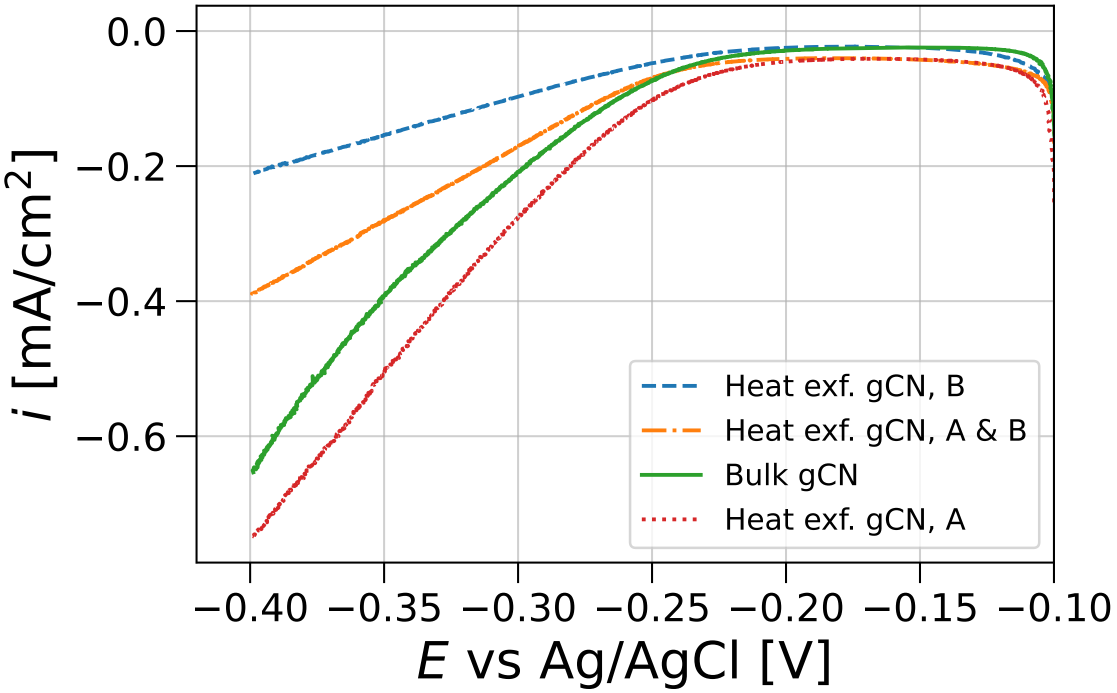

Figure 4.15: LSV of samples with different washing procedures. The sample that was washed exclusively after the primary synthesis step from dicyandiamide to graphitic carbon nitride performance the best, while samples that were washed after exfoliation show detrimental results compared to the bulk sample.

Figure 4.16 below shows the EIS of graphitic carbon nitrides with different washing procedures and exfoliation. The measurements were made in an 1 M H_2SO_4 solution in the frequency range 1 mHz to 100 kHz, showing the negative real impedance measured in ohms along the horizontal axis and the imaginary component measured in ohms along the vertical axis. All of the resulting graphs show semicircle behavior, although somewhat less clearly so than for other measurements in this project. The sample that was washed after the primary heating step, but not after exfoliation, shows the smallest charge transfer resistance, while the sample that was washed after the heat exfoliation performed the worst with its large relative charge transfer resistance. This is in accordance with what was seen in the LSV, but the sample that was washed after both heating steps performs better than the bulk sample in this measurement.

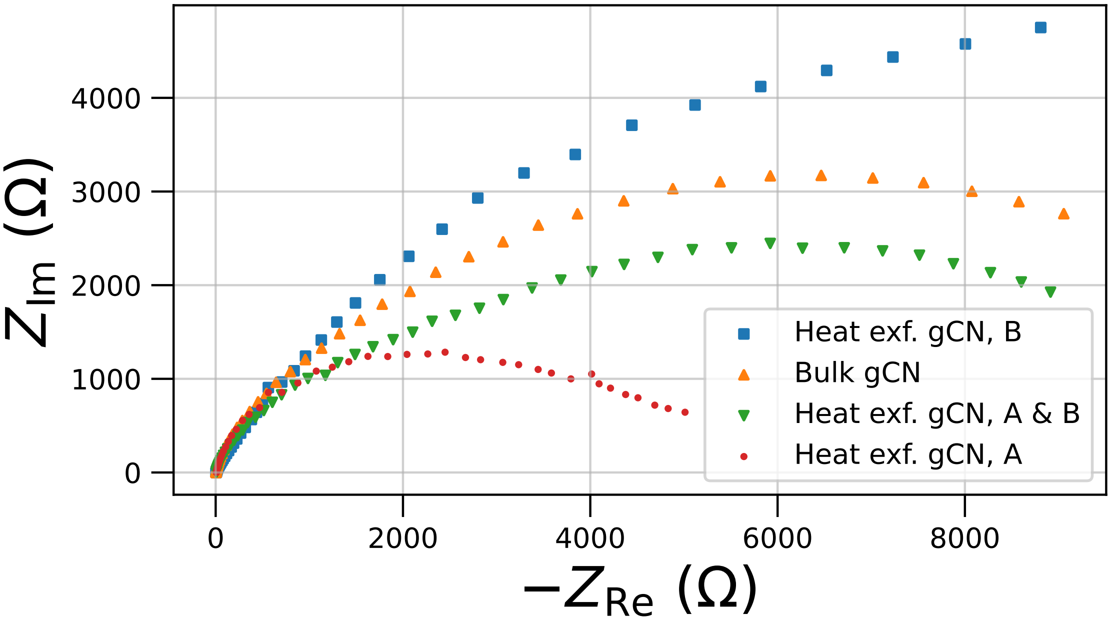

Figure 4.16: EIS of samples with different washing procedures. The worst performing sample was washed after the exfoliation, while the best performing sample was washed only after the initial heating step.

4.7 S(T)EM-imaging and EDX results

Figure 4.17 below is a S(T)EM image of bulk graphitic carbon nitride, with a scale bar of 2 μm and with an accelerating voltage of 30.0 kV. The image shows that bulk g-C_3N_4 is very layered – graphitic – as seen in the left and back part of the image.

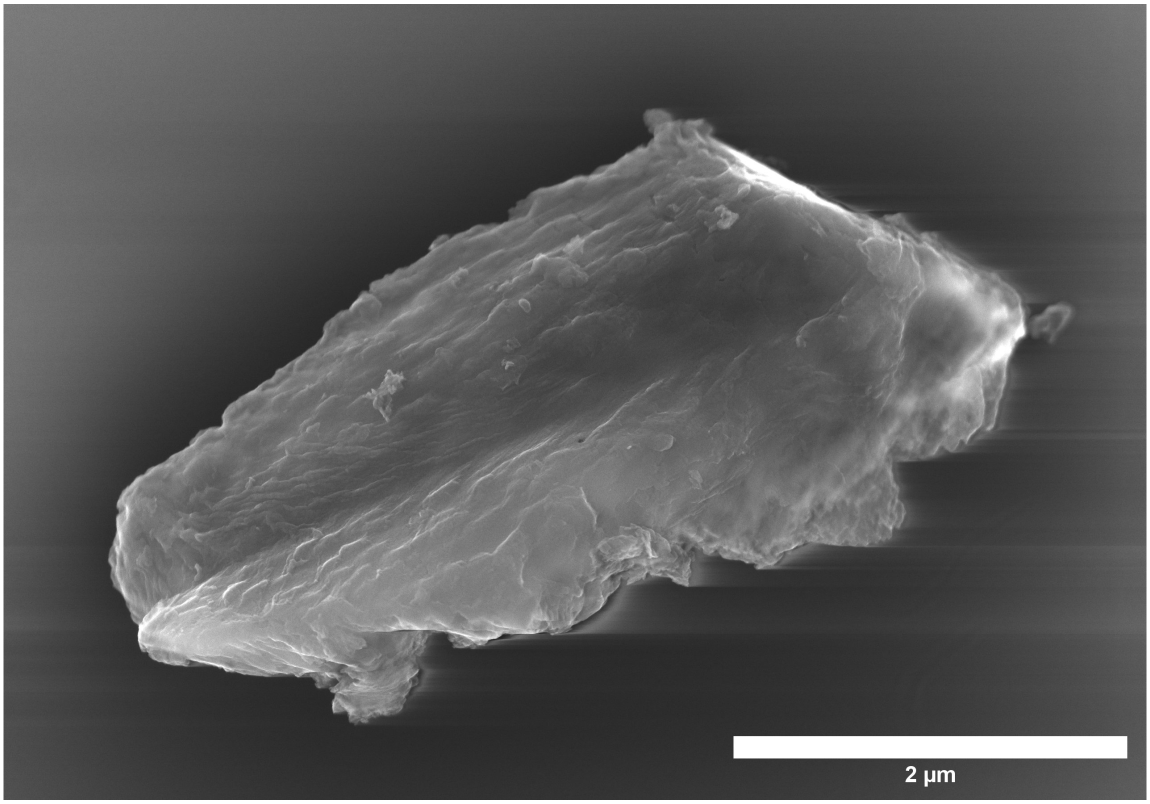

Figure 4.17: S(T)EM imaging of bulk g-C_3N_4. The image clearly displays the layered nature of bulk g-C_3N_4 in the left parts of the picture. This makes bulk g-C_3N_4 neither transparent nor optimized for surface utilization.

Figure 4.18 below is a bright field S(T)EM image of bulk graphitic carbon nitride, with a scale bar of 100 nm and with an accelerating voltage of 30.0 kV. The image shows that bulk g-C_3N_4 is not transparent in these measurements due to the many layers.

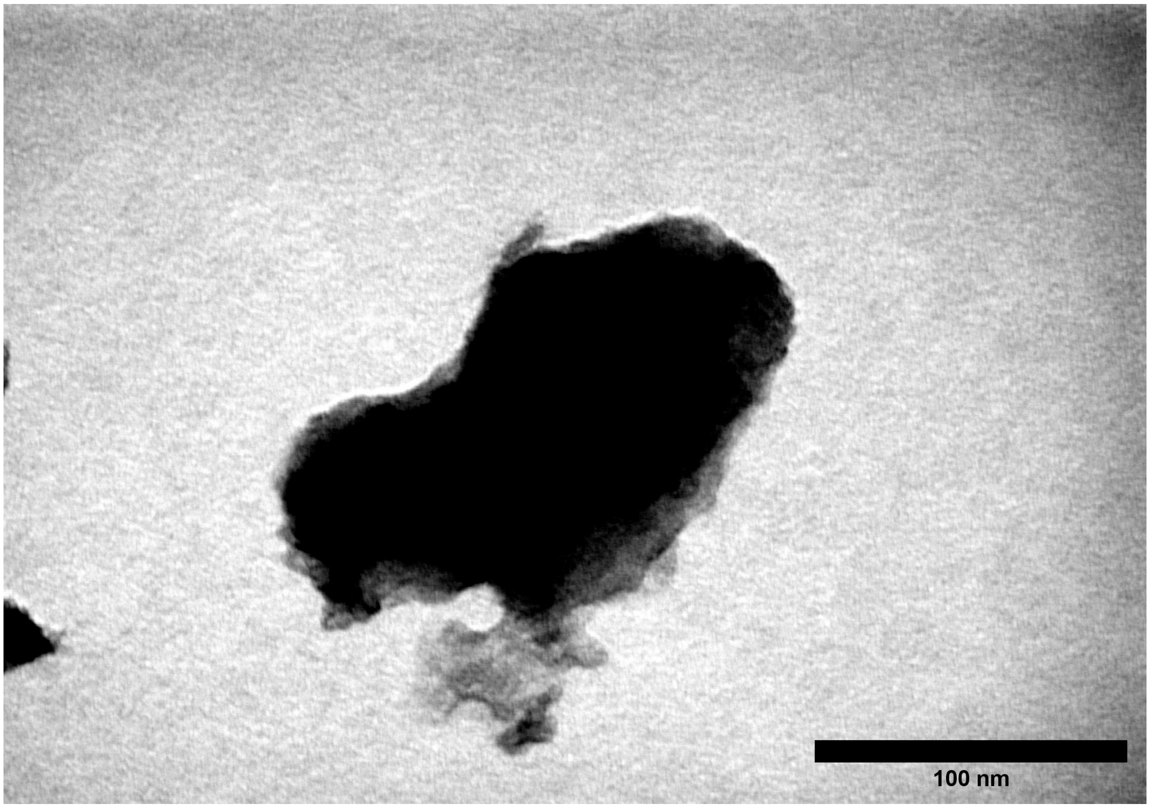

Figure 4.18: Bright field S(T)EM imaging of bulk g-C_3N_4. The image shows that even for particles as small as a few hundred nm across, bulk samples are not transparent.

Figure 4.19 below is a S(T)EM image of bulk graphitic carbon nitride with 20wt% Pt deposited with ultrasound, with a scale bar of 300 nm and with an accelerating voltage of 30.0 kV. It can be seen on the image that the platinum nanoparticles have a tendency to clump together with bulky surface areas. The particles are not spread evenly on the entire particle. EDX results confidently show that the brighter parts are platinum, and that the assumed g-C_3N_4 particle consists mainly of carbon and nitrogen.

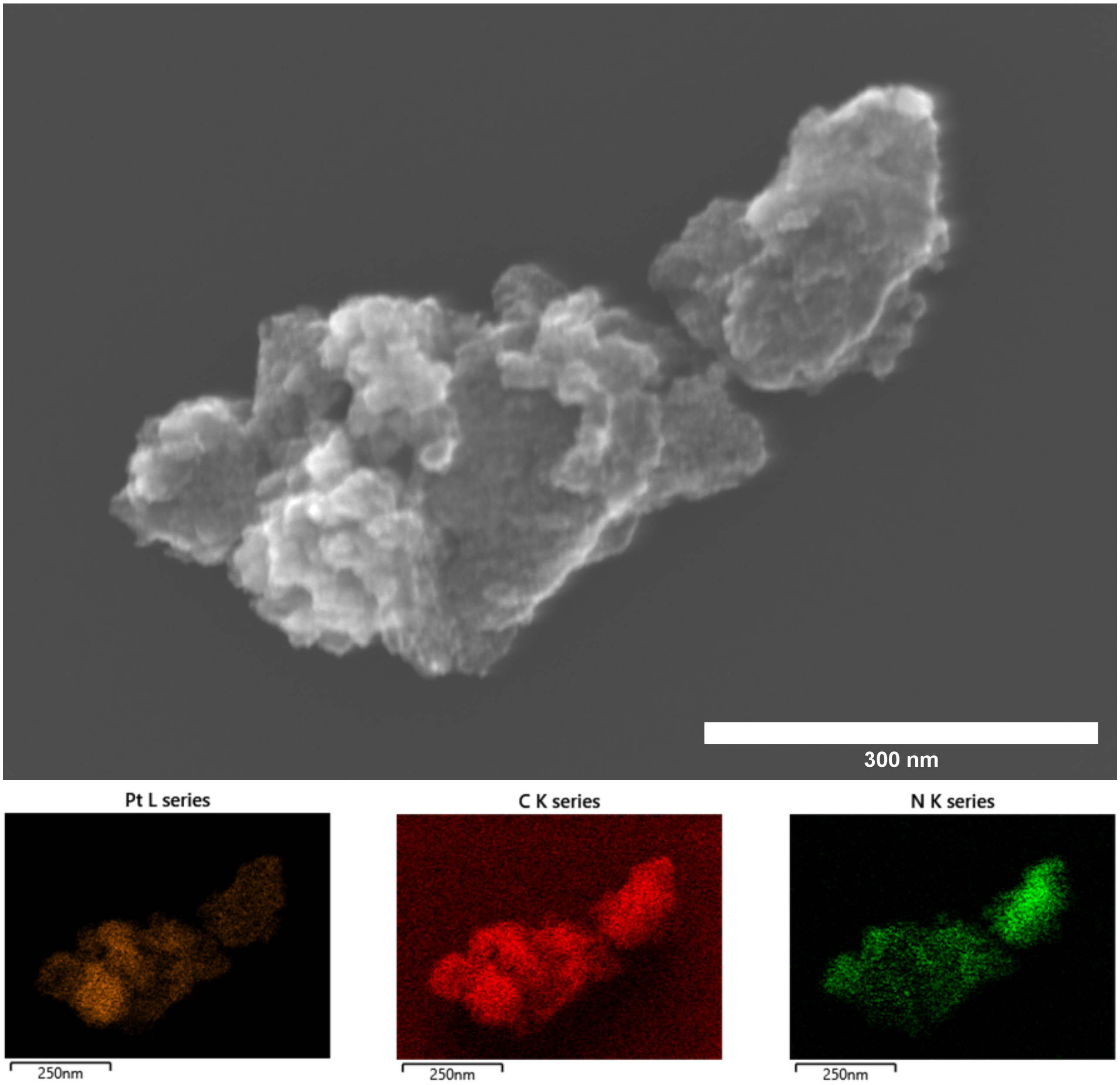

Figure 4.19: S(T)EM imaging and EDX of g-C_3N_4 and Pt. The upper image shows how Pt clusters on bulk g-C_3N_4. The leftmost EDX image below confirms that the adhered particles are platinum, and the two others confirm the carbon and nitrogen content of the assumed g-C_3N_4 particle.

Figure 4.20 below is a bright field S(T)EM image of ultrasound exfoliated graphitic carbon nitride with 1wt% Pt deposited with ultrasound, with a scale bar of 200 nm and with an accelerating voltage of 30.0 kV. The image shows that the particle truly is exfoliated, as it is very transparent in the image, being thus only a few sheets thick. It can also be seen that the platinum nanoparticles now have a tendency to either clump together in denser areas, or spread out around the perimeter of the particle. In both cases, the platinum nanoparticles are substantially better spread out than on the bulk particles.

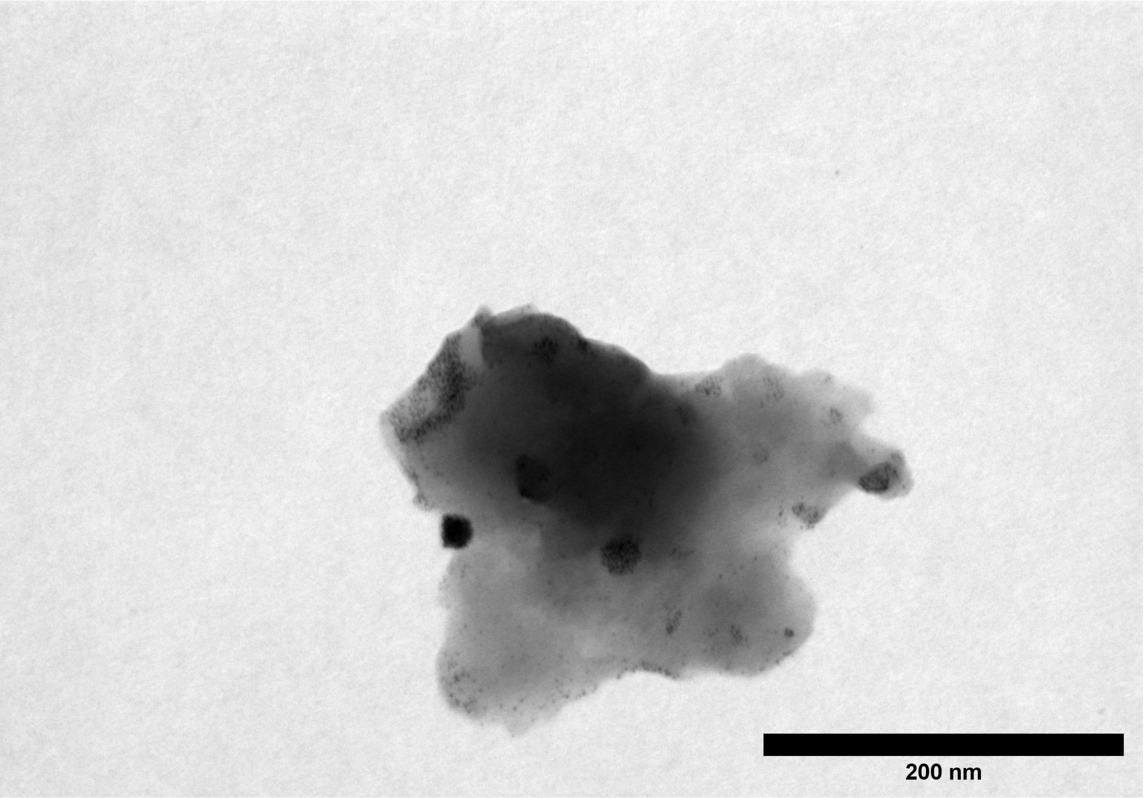

Figure 4.20: Bright field S(T)EM of exfoliated g-C_3N_4 with Pt. The image shows that the exfoliated particle has a more even distribution of platinum nanoparticles than what was observed on bulk g-C_3N_4.

Figure 4.21 below is a bright field S(T)EM image of ultrasound exfoliated graphitic carbon nitride with 1wt% Pt deposited with ultrasound, with a scale bar of 100 nm and with an accelerating voltage of 30.0 kV. It shows in greater detail that individual nanoparticles either clump together or spread out on the perimeter of the particles.

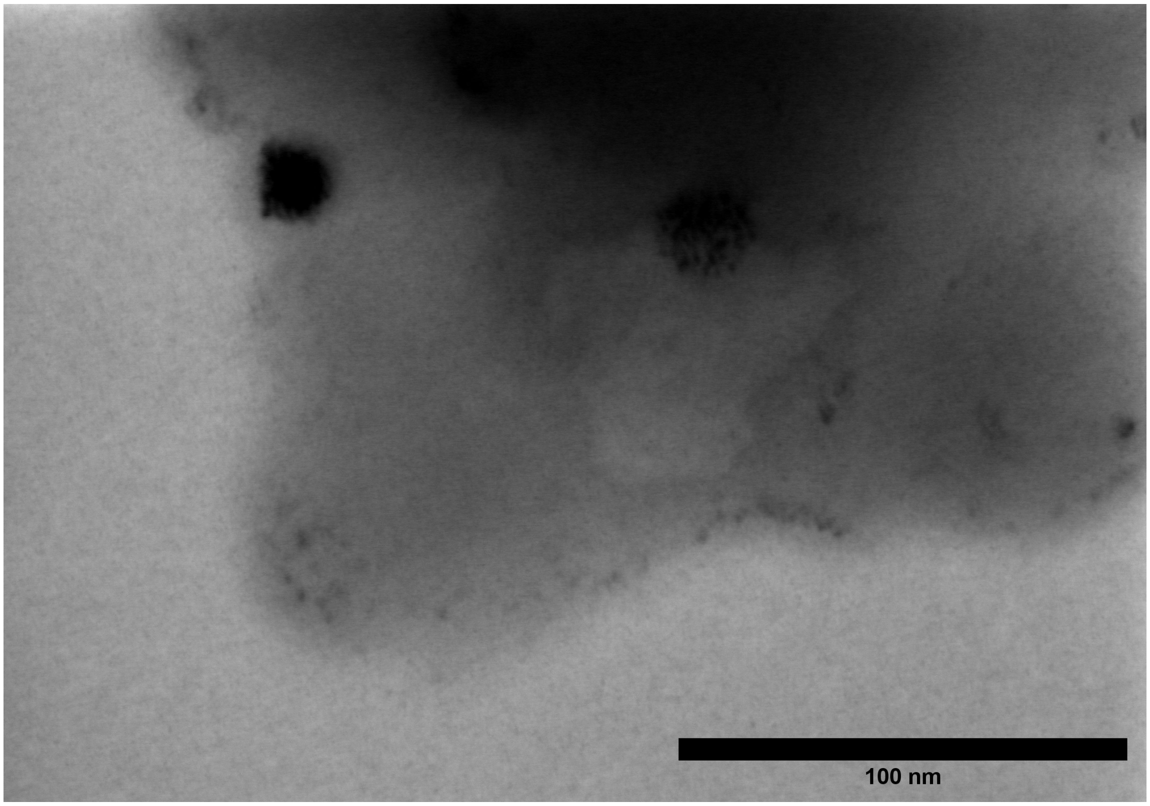

Figure 4.21: More bright field S(T)EM of exfoliated g-C_3N_4 with Pt. There seems to be individual nanoparticles quite evenly distributed along the edges of the exfoliated g-C_3N_4.

Figure 4.22 below is a bright field S(T)EM image of ultrasound exfoliated graphitic carbon nitride with a scale bar of 250 nm and with an accelerating voltage of 30.0 kV. It also exemplifies that the exfoliation process has flaked off layers of the particle so that the layered nature becomes very visible. The overlapping of different regions in the image and the resulting brightness indicate that some regions of the particle consists only of single sheets.

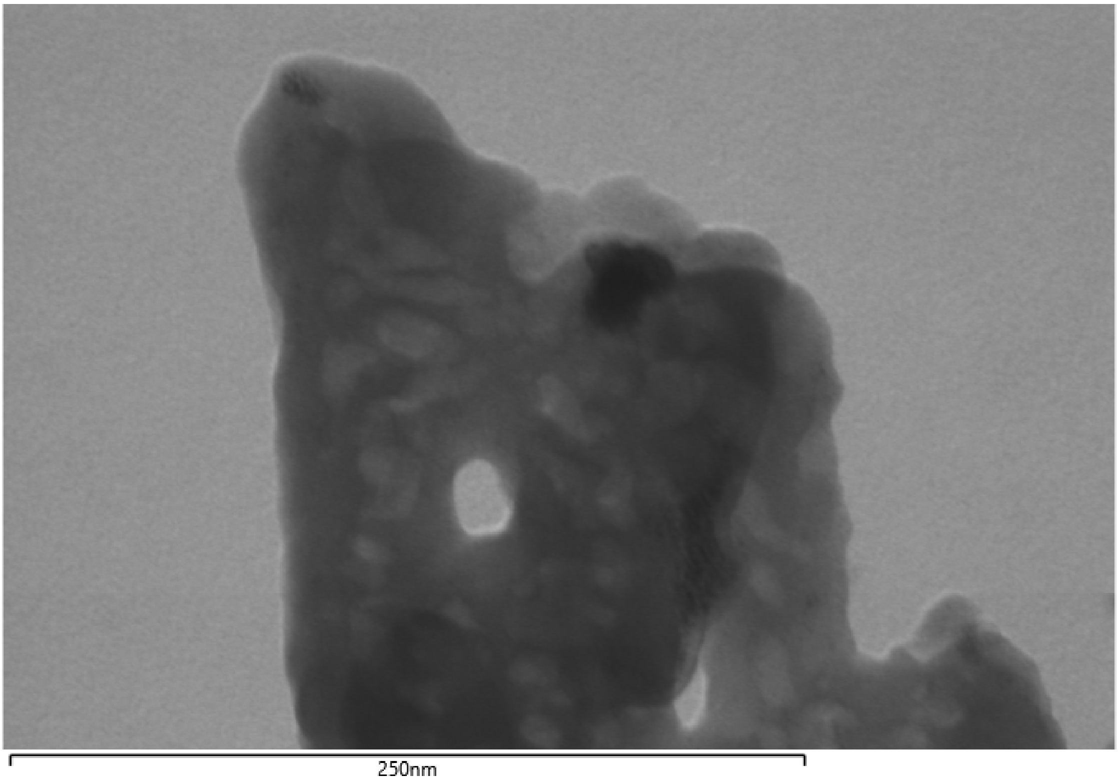

Figure 4.22: S(T)EM imaging of thinly layered exfoliated g-C_3N_4. The overlapping of individual sheets can be observed and confirm that the particle has been substantially exfoliated by the ultrasound procedure.

Table 4.2 below shows the results from an elemental composition EDX measurement for a graphitic carbon nitride sample. The results show that the measured values and the expected stoichiometric values correspond well, indicating that the material produced and utilized in this project is the expected graphitic carbon nitride.

	Measured value	Ideal value
Carbon	0.60	0.57
Nitrogen	0.40	0.43

Table 4.2: The table shows the measured values from an EDX sample of graphitic carbon nitride, and its ideal molar fraction value. The values show that the analyzed material with high certainty is g-C_3N_4.

4.8 Mott-Schottky analysis

A Mott-Schottky plot for a representative graphitic carbon nitride sample in 1M H_2SO_4 is shown in Figure 4.23. The plot shows the applied voltage in volts relative to a Ag/AgCl reference electrode on the horizontal axis and the negative squared measured capacitance on the vertical axis for three different frequencies. The measurements show positive slopes, indicating that the sample is n-type semiconductor in the measured voltage range. There is a frequency disparity, meaning the extrapolations do not converge towards the same value, with a spread typically between 0.1V and 0.2V for all the measured samples. The flatband for this particular sample was determined to be between -1.03 V and -1.12 V. The flatband potentials for all the different samples in this solution were determined to be between -1.00 V and -1.22 V, as summarized in Table 4.3 in the next section.

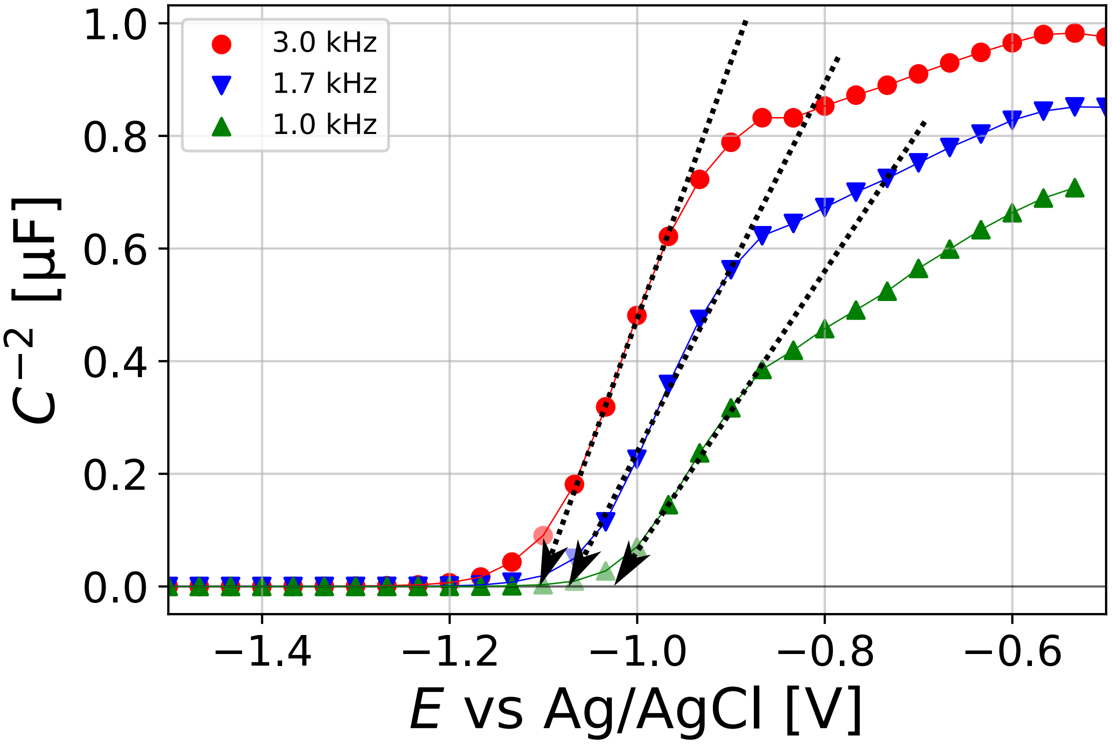

Figure 4.23: A Mott-Schottky for a representative g-C_3N_4 sample. The upwards slope confirms that the material is an n-type semiconductor. The flatband potential V_{fb} for this particular sample is between -1.03 V and -1.12 V.

4.9 Diffuse light absorption spectra, Tauc plots and band gap determinations

Figure 4.24 below shows a diffuse light absorption spectrum for a representative graphitic carbon nitride sample. It displays the irradiated light wavelengths in nanometers along the horizontal axis and the absorption along the vertical axis in arbitrary units. The figure illustrates how the material gradually starts to absorb light when the wavelengths of the incident light is shorter than 500 nm. It also shows that the material reaches peak absorption around 410 nm, and absorption steadily decreases when the wavelength is further shortened.

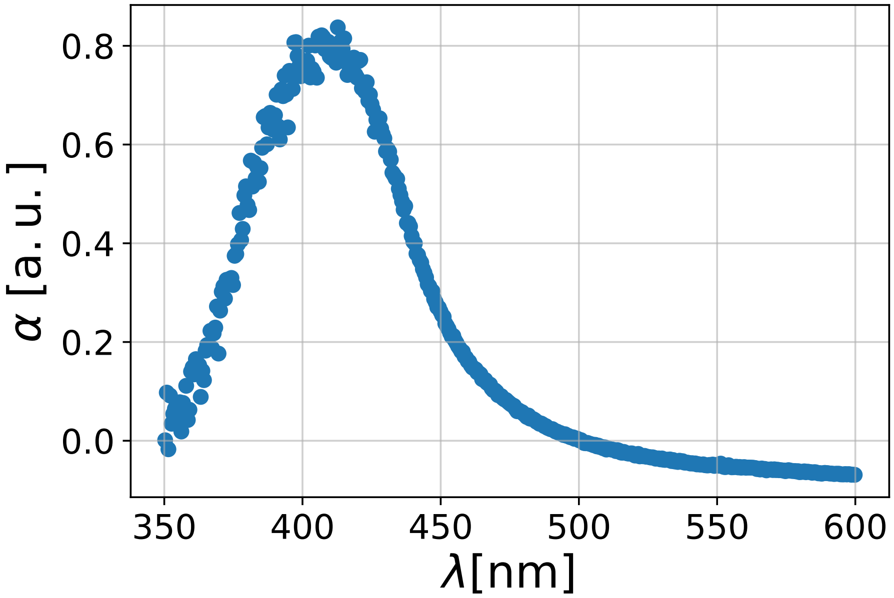

Figure 4.24: Absorption spectrum for a graphitic carbon nitride sample. The material displays significant absorption of visible light and towards the UV-area of the spectrum.

Figure 4.25 below shows a Tauc plot for a representative graphitic carbon nitride sample. It displays the irradiated light energy in electron volts along the horizontal axis and the absorption along the vertical axis in arbitrary units. The figure illustrates how the material gradually starts to absorb light when the energy of the incident light has energy larger than 2.77 eV, which is determined to be the band gap of this particular sample. It also shows that the material reaches peak absorption around 3.1 eV, and absorption steadily decreases when the energy is further increased. Note that the values on the vertical axis is raised to the power of two, and gives a section of linear increase in the Tauc plot. This means that the material is a direct band gap semiconductor.

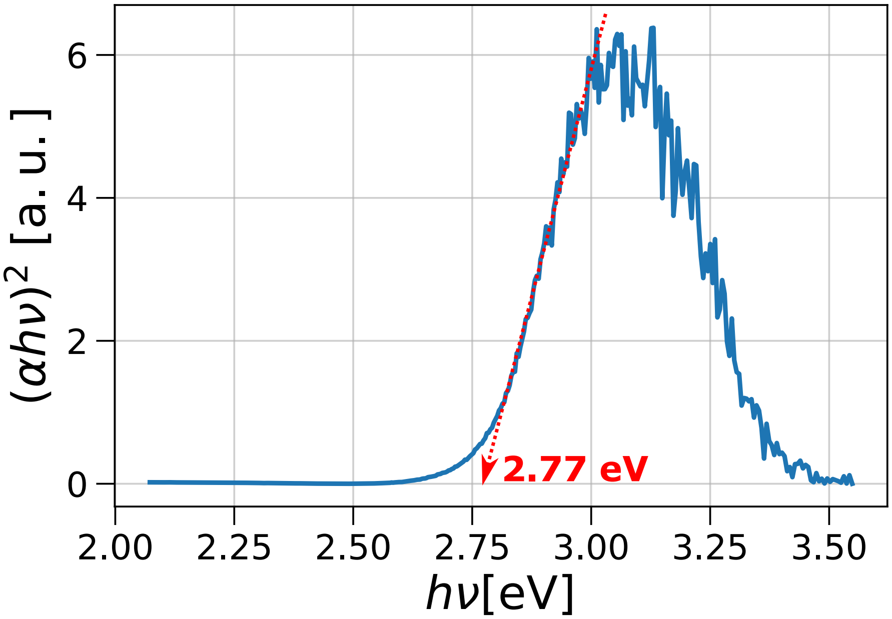

Figure 4.25: Tauc plot for a graphitic carbon nitride sample. The material has a band gap of 2.77 eV, and from the onset of this energy the material will absorb incident light. The material absorbs a significant portion of the visible light and some towards the UV part of the spectrum.

Figure 4.26 below shows a selection of materials in an energy diagram, with their band gap, flatband potential and calculated valence bond energy illustrated in relation to the HER and OER. By the data in this diagram, all the materials are suited for water splitting, as the conduction band energy and valence band energy supersedes that of the HER and OER reactions. From left to right, it is observed that the size of the band gap increases. This means that the band gap can be tuned between the two measured extremities to fit experimental needs. Bulk g-C_3N_4 has the smallest band gap measured, at 2.66 eV. Ultrasound exfoliation increases the band gap, as does the washing procedures and heat exfoliation. All the materials have a large overpotential for the hydrogen evolution reaction and a smaller overpotential for the oxygen evolution reaction.

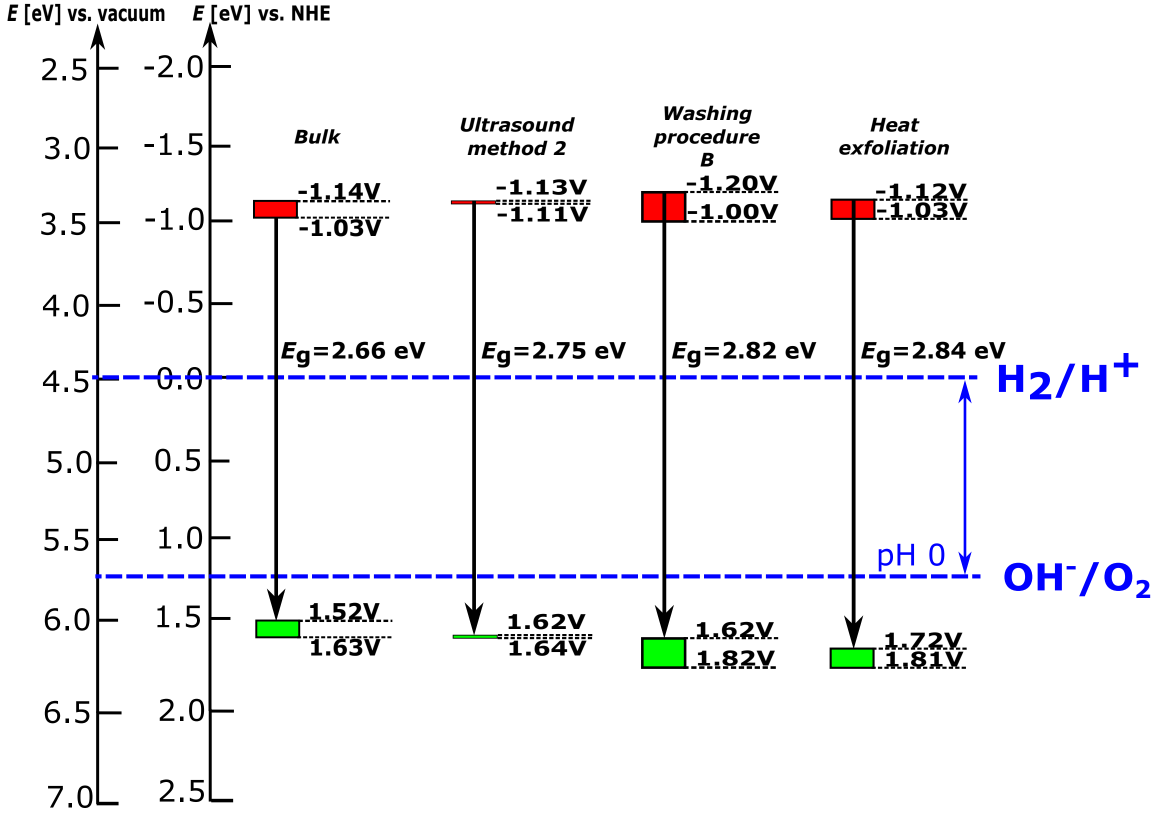

Figure 4.26: Selected energy diagrams for graphitic carbon nitride. The figure shows that the band gap increases from left to right with the different production parameters, giving the possibility of tuning the band gap. The diagram shows that all the materials have a high overpotential for hydrogen evolution, and a smaller overpotential for evolving oxygen.

A full version of this diagram with all samples measured in this project is listed in the Appendix in Figure A.1. One can see that the band gaps for the differently produced samples range from 2.66 eV to 2.84 eV. This corresponds to the wavelength range 466 nm to 436 nm. The pristine, bulk sample had the smallest band gap, which means that this is the sample that would be susceptible to absorb the largest portion of the solar spectrum. One increment up in the band gap size are the ultrasonicated samples, with band gaps in the energies around 2.75 eV. Further increasing the band gap, one has the heat exfoliated samples *with* a washing procedure, whose energies surpass 2.80 eV. Lastly, heat exfoliated samples without cleaning procedures have the largest band gaps measured in this project with 2.84 eV. These results show that there is a systematic difference in the preparation method of the graphitic carbon nitride and the subsequent band gap. The order, from small to bigger band gaps, goes pristine bulk < ultrasound exfoliation < heat exfoliation with cleaning < heat exfoliation without cleaning. An unfortunate consequence of the band gap exclusively increasing in size, is that these results do not suggest a preparation method that would increase the span of the solar spectrum that could be absorbed in a sample. They strictly limit the portion of the sunlight which can be absorbed.

Table 4.3 below denotes all of the measured band gaps, flatband potentials and calculated valence bonds. A selection of this data has been used to make Figure 4.26, while in the Appendix in Figure A.1, all the materials are illustrated in one diagram. The table clearly shows the trend detailed in the previous paragraph.

	Band gap	**Flatband potential**	**Valence band**
Bulk	2.66 eV	[-1.14V, -1.03V]	[1.52V, 1.63V]
Ultrasound method 3	2.71 eV	[-1.17V, -1.03V]	[1.54V, 1.68V]
Ultrasound method 2	2.75 eV	[-1.13V, -1.11V]	[1.62V, 1.64V]
Ultrasound method 1	2.80 eV	[-1.22V, -1.07V]	[1.44V, 1.59V]
Washing proc. B	2.82 eV	[-1.20V, -1.00V]	[1.62V, 1.82V]
Washing proc. A & B	2.83 eV	[-1.09V, -1.04V]	[1.74V, 1.79V]
Washing proc. A	2.84 eV	[-1.13V, -1.06V]	[1.71V, 1.78V]
Thermic exfoliation	2.84 eV	[-1.12V, -1.03V]	[1.72V, 1.81V]

Table 4.3: Band gaps, flatband potentials and valence band positions for a range of samples in 1 M H_2SO_4. There is a trend from a smaller band gap for bulk g-C_3N_4 to a larger band gap for heat exfoliated g-C_3N_4, giving the possibility of tuning the band gap.

Figure 4.27 below shows the spectral irradiance and wavelength absorption of graphitic carbon nitride in the same figure. It is observed that graphitic carbon nitride absorbs light towards the lower end of the solar spectrum, missing the peak irradiance wavelengths by about 100nm.

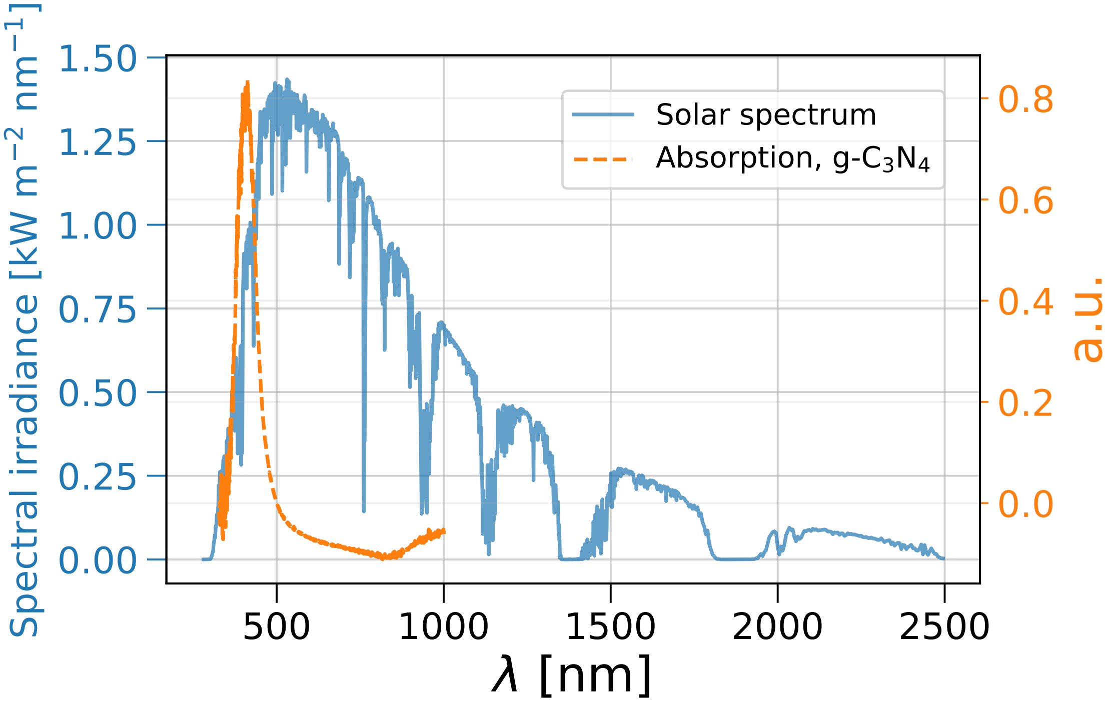

Figure 4.27: Figure showing the wavelengths of photons hitting the Earth at sea level, as well as graphitic carbon nitride's absorption in the same spectral range. These do coincide, but preferably the g-C_3N_4 absorption area should be shifted towards the right in the figure in order to utilize a larger portion of the solar irradiance.

4.10 Photoelectrochemistry

Figure 4.28 below shows the photoelectric response as a function of illumination time and illumination, with the eloped time in seconds on the horizontal axis and the current density in μA cm^{-2} along the vertical axis. The measurements are done in a 1 M Na_2SO_4 solution with monochromatic light with intensity 75 W/m^{-2} and an applied voltage of -0.1 V. The light off-on cycle lasts 5s:5s. It is observed that the recorded photocurrent is cathodic. The onset of the photocurrent response matches decently with that discovered in the diffuse light spectroscopy, with an appreciable response picking up from around 500 nm and shorter wavelengths.

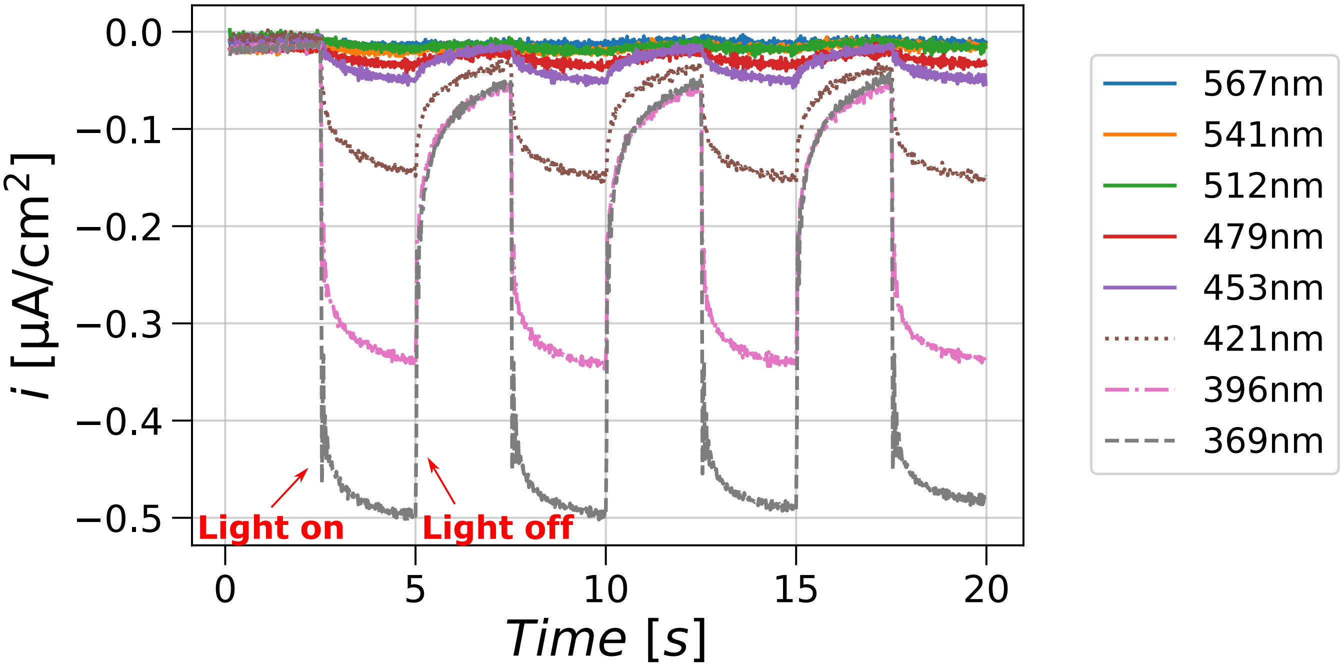

Figure 4.28: Photoelectric response with time. The observed photoresponse is reduced in magnitude with increasing wavelengths, corresponding with the band gap of the material.

Figure 4.29 below shows the photoelectric response as a function of illumination time and illumination for samples with different applied voltages, with the eloped time in seconds on the horizontal axis and the current density in μA cm^{-2} along the vertical axis. The measurements were done in a 1 M Na_2SO_4 solution with monochromatic light with intensity 75 W/m^{-2}. The light off-on cycle lasts 5s:5s. It is observed that the photocurrent response is anodic when the applied voltage is above 0.35 V and cathodic when the applied voltage is below 0.35 V. A graph tracing out this behavior is shown in Figure 4.30.

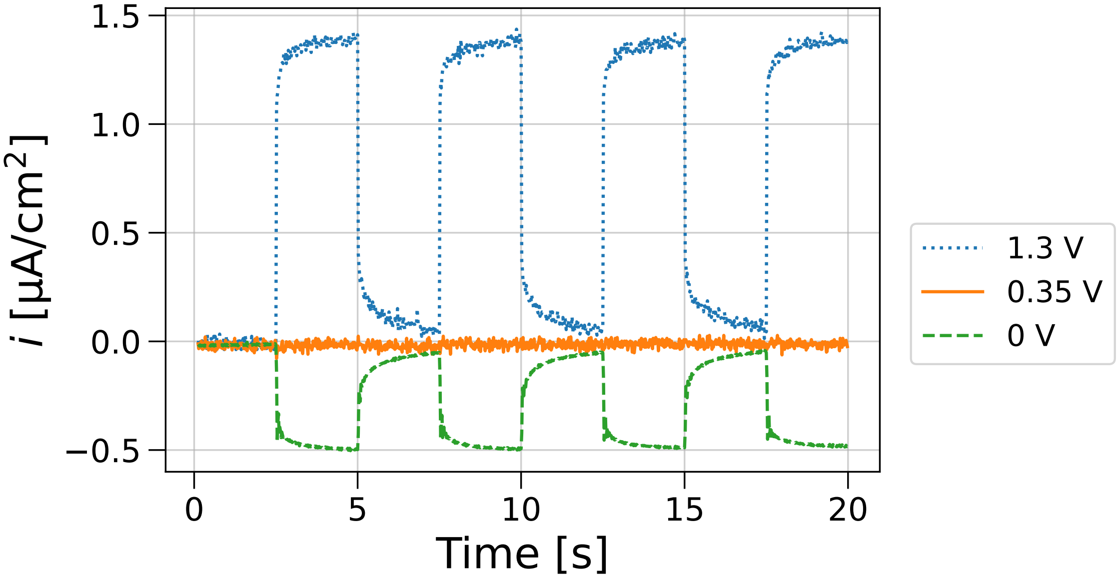

Figure 4.29: Photoelectric response when g-C_3N_4 is subject to different applied voltages. It is seen that the photocurrent switches from anodic to cathodic at around 0.35 V.

Figure 4.30 below shows the photoelectric response as a function of the applied voltage and illumination, with the applied voltage in volts on the horizontal axis and the current density in µA cm^{-2} along the vertical axis. The measurements were done in a 1 M Na_2SO_4 solution with monochromatic light with intensity 75 W/m^{-2}. It is observed that the photocurrent response switches from anodic at high voltages to cathodic responses at lower voltages. This is in accordance with litterature [29], which also shows that the onset potential in 0.3 V for similar conditions and reference electrodes.

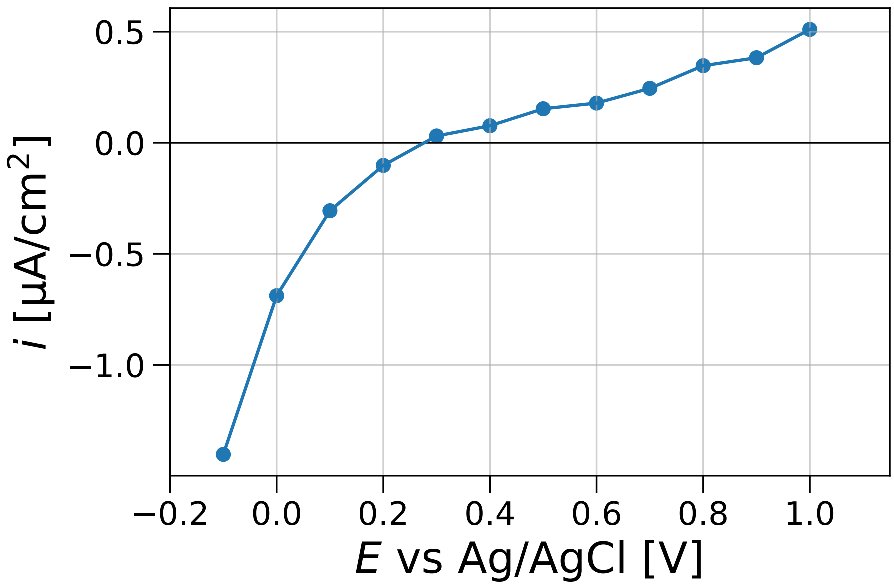

Figure 4.30: Photoelectric response at different applied voltages. The material changes from anodic to cathodic behavior in the onset potential of 0.3 V.

Figure 4.31 below shows the photoelectric response as a function of illumination time and illumination for a sample with 0.3 V applied voltage, with the eloped time in seconds on the horizontal axis and the current density in µA cm^{-2} along the vertical axis. The measurements were done in a 1 M Na_2SO_4 solution with monochromatic light with intensity 75 W/m^{-2}. The light off-on cycle lasts 5s:5s. The graph is characterized by a rapid spike in photocurrent followed by a slower decay, with a smaller overshoot and return to an equilibrium before the next on-off cycle starts. It is observed that this behavior follows that of which is described by Figure 2.10a in the Theory section. The trace of the graph thus indicates that electrons and holes are generated with the onset of the lighting, separated, and that there is a combination of recombination and charge transfer happening in and on the g-C_3N_4. The shape also indicates that band edge unpinning is happening for the system.

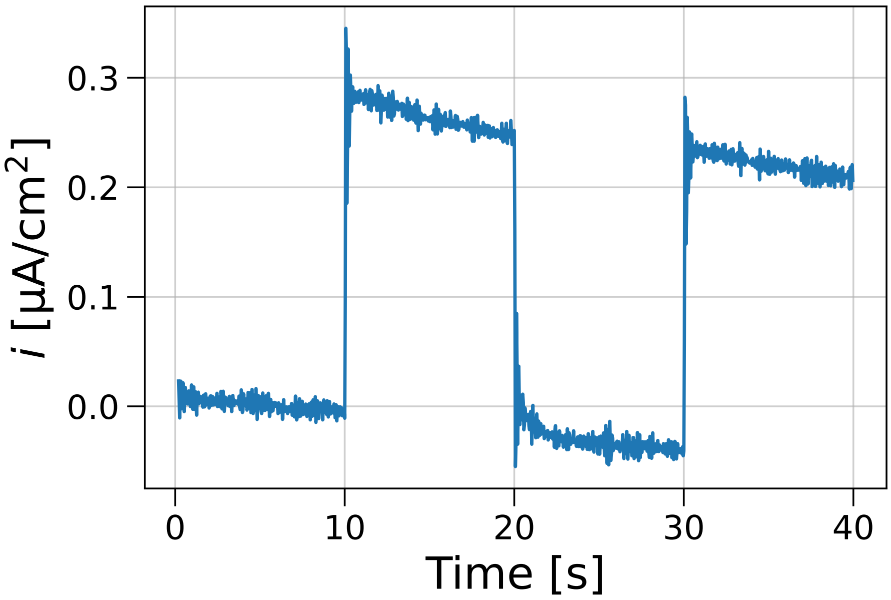

Figure 4.31: Photoelectric response for a graphitic carbon nitride electrode. The shape indicates that there are processes of charge carrier generation, separation, recombination and band edge unpinning.

Figure 4.32 below shows the photoelectric response as a function of illumination time and illumination for a sample with 0.7 V applied voltage, with the eloped time in seconds on the horizontal axis and the current density in µA cm^{-2} along the vertical axis. The measurements were done in a 1 M Na_2SO_4 solution with monochromatic light with intensity 75 W/m^{-2}. The light off-on cycle lasts 5s:5s. The graph is characterized by a rapid spike in photocurrent followed by a upwards movement towards an equilibrium, with a smaller overshoot and return to an equilibrium before the next on-off cycle starts. It is observed that this behavior follows that of which is described by Figure 2.11 in the Theory section: the graph shifts its shape due to the increase in applied voltage. The change in shape is partly described by the changes in the Helmholtz layer, and indicates all of the same processes as described for Figure 4.31 above.

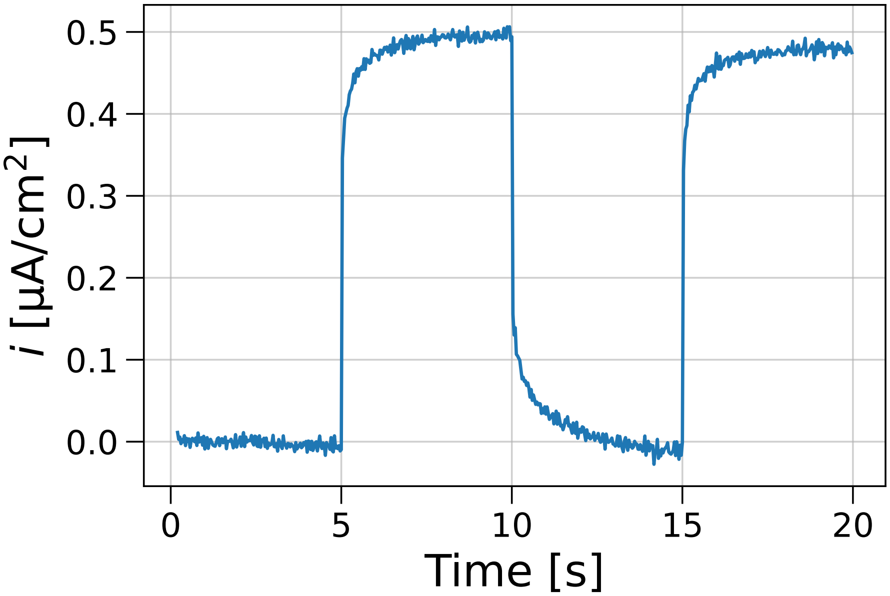

Figure 4.32: Photoelectric response for a graphitic carbon nitride electrode. The shape indicates that there are processes of charge carrier generation, separation, recombination and band edge unpinning, as well as a higher applied voltage than for other measurements.

Figure 4.33 below shows the photoelectric response as a function of illumination time and illumination for a sample with -0.5 V applied voltage, with the eloped time in seconds on the horizontal axis and the current density in µA cm^{-2} along the vertical axis. The measurements were done in a 1 M Na_2SO_4 solution with monochromatic light with intensity 75 W/m^{-2}. The light off-on cycle lasts 5s:5s. The graph is characterized by a rapid spike in photocurrent followed by a large upwards movement towards an equilibrium, with a smaller overshoot and return to an equilibrium before the next on-off cycle starts. It is observed that this behavior follows that of which is described by Figure 2.10b in the Theory section: the graph moves slightly upwards for each subsequent measurement, indicating that the pH changes upwards due to the production hydrogen gas, which would rid the local area of H^+-ions.

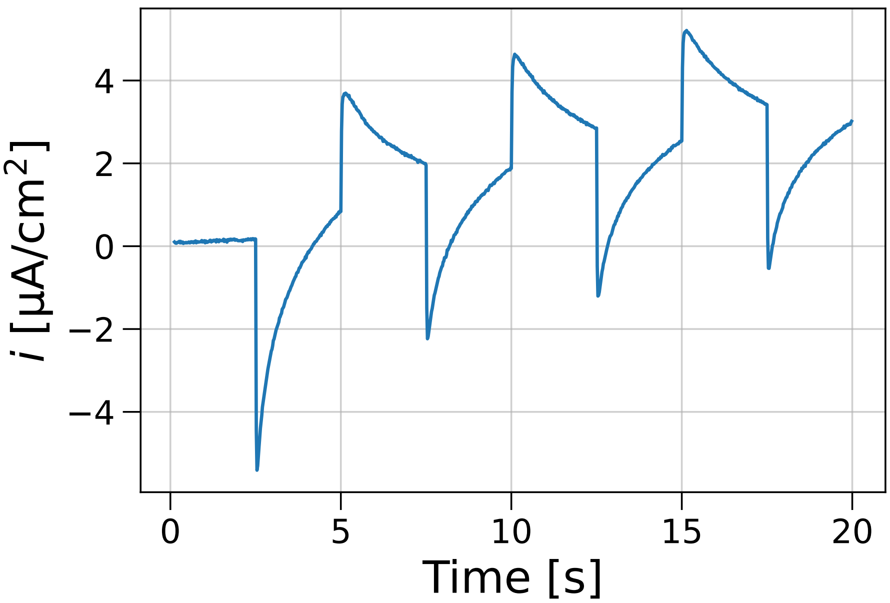

Figure 4.33: Photoelectric response for a graphitic carbon nitride electrode. The shape indicates that there are processes of gas evolution, pH changes, charge carrier generation, separation, recombination and band edge unpinning.

Figure 4.34 below shows the measured evolved hydrogen in micromoles for a 52mg graphitic carbon nitride sample in a mixture of 90mL distilled water and 10mL methanol as a function of time when undergoing simulated solar illumination, with stirring being turned on after 150 minutes. The data clearly shows how the system produces hydrogen at an elevated rate when stirring is functioning. The data indicate an evolution rate increase of almost 90% with stirring.

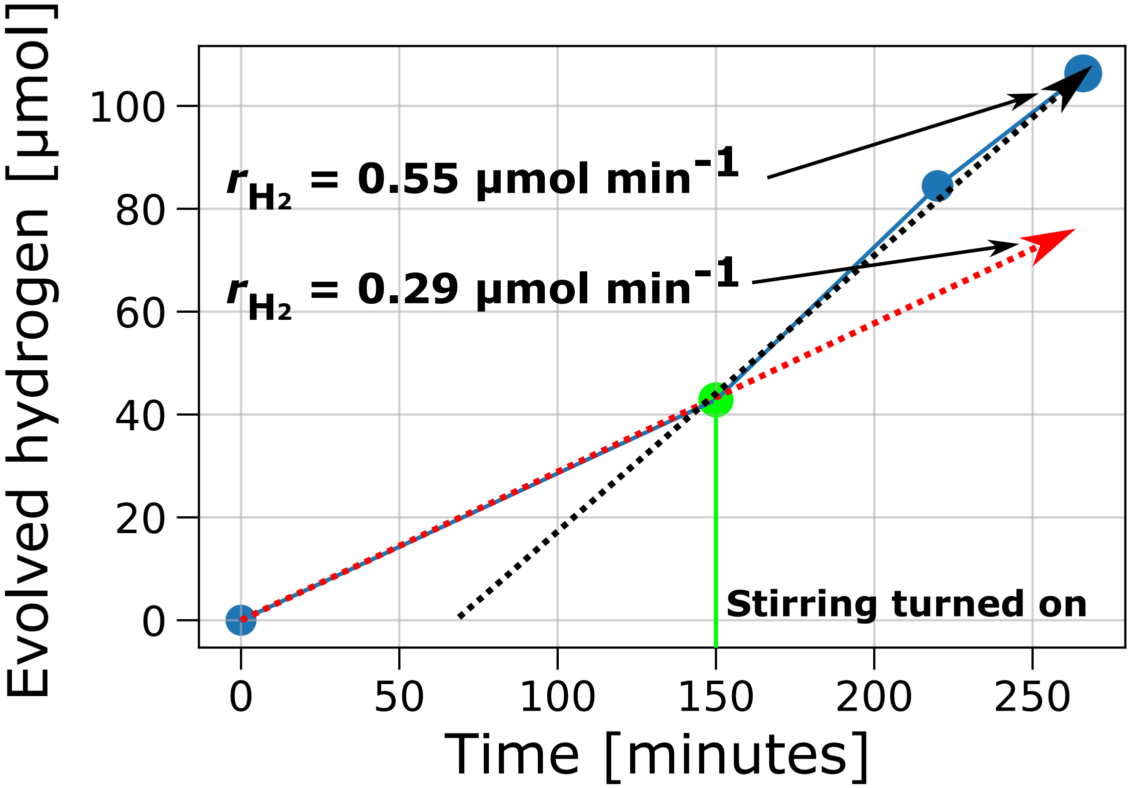

Figure 4.34: Effects of stirring on hydrogen evolution. The hydrogen evolution is very linear in the last 3 measurements, and the rate at which hydrogen evolves during these measurements is significantly larger than for the first two points, where there was no stirring.

Figure 4.35 below shows the measured evolved hydrogen in micro mole along the vertical axis and the eloped time in minutes along the horizontal axis. The solution for the bulk graphitic carbon nitride sample was a mixture of 90 mL distilled water and 10 mL methanol, while for the two other graphs the solution was 90 mL of ultrasound exfoliated g-C_3N_4 solution and 10 mL methanol. It was believed that the solution of ultrasound exfoliated g-C_3N_4, which was 50% distilled water and 50% ethanol, would increase the amount of detected hydrogen when compared to using just distilled water. This was however not the case, as seen in the graph below.

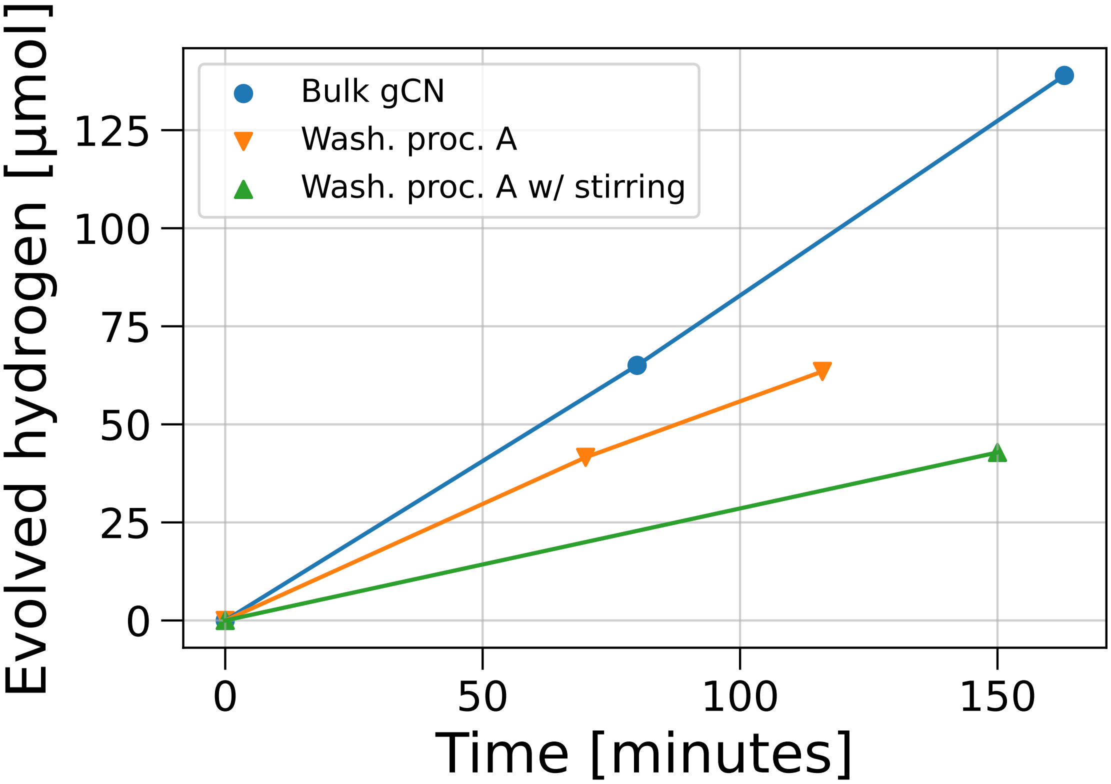

Figure 4.35: Evolved hydrogen for different samples with different parameters. It is noted that the effects of stirring is drastic, but also that the amount of evolved hydrogen is very linear over the measured time frame.

It was noticed during the illumination of the washed samples that a thin layer of graphitic carbon nitride would solidify on top of the vessel, quite possibly reducing the amount of received illumination inside the roundbottom flask, thus hampering the maximum possible outcome.

5 Discussion

To build a proper understanding of what this project has achieved, one must detail what questions it answers. The following section will elaborate upon and connect the results in such a way that a thorough understanding of the photoelectrochemical possibilities of graphitic carbon nitride will emerge. The grand question is *if graphitic* *carbon nitride is a suited material for hydrogen production from water through utilization of solar energy*, and what measures can be taken to improve the performance of the product. We will build our understanding of this subject by first addressing fundamental questions regarding the process and results, which will substantiate the conclusion of this project.

Claim: The synthesis of graphitic carbon nitride has been successful. There are multiple reasons to be confident that the produced powder is graphitic carbon nitride, and initially in bulk form. These are color changes, results from XRD, TGA, EDX and diffuse light reflectance. The most immediate result is the vivid color change from the initial white of the dicyandiamide to the characteristic yellow of graphitic carbon nitride. This is in accordance with literature [2] [32] [34]. Based on this, one can be certain that at least some dicyandiamide has been converted in the heating step. It was documented in the previous project how the shade of yellow was affected by the heating temperature. In this project, it has also been shown that different heating time also affects the color. As this is explored in the literature, for example with heat exfoliation, this further confirms the presence of g-C_3N_4. A color comparison between bulk and heat exfoliated graphitic carbon nitride is shown in Figure 4.1. The main difference between these two samples is that the heat exfoliated sample has been reheated for 2h after the original synthesis, and the color changes as expected. This is a clear indication that the original sample was graphitic carbon nitride.

It was shown in the previous project that X-ray diffractograms taken for samples prepared at different temperatures would gradually convert from dicyandiamide to graphitic carbon nitride before decomposing. In this project, as seen from Figure 4.2, it has been documented that not only is the powder the same as in literature and the previous project, but also that the heat exfoliated samples will shift its main peak 1^o to the right. This has been described by a number of papers as a confirmation of successful exfoliation [26], and is also what we were able to achieve in this project.

Considering that the TGA results showed that the weight percentages changed with the expected amounts at the expected temperatures, it seems certain that the conversion from dicyandiamide to graphitic carbon nitride is further confirmed by the TGA analysis.

An elemental composition was estimated from EDX results, with the comparison between the measured and ideal results in Table 4.2. The measured and ideal values are 0.60 & 0.57, and 0.40 & 0.43 for carbon and nitrogen respectively, giving a very reasonable verification of the elemental composition for the produced powders.

Additionally, one expects graphitic carbon nitride to show band gap properties for incident light with wavelengths shorter than 500 nm. As seen in Figures 4.24, 4.25, 4.26, 4.27 and 4.28, this is clearly the case. Specifically, diffuse light reflectance in Figure 4.24 and the subsequent Tauc plot in Figure 4.25 clearly demonstrates how the incident light begins to be absorbed by the material in the specified range, with a corresponding band gap of 2.77 eV for that particular sample. Figure 4.28 also shows how a sample starts to convert appreciable amounts of irradiance to electricity starting 479 nm. These values are retrieved from completely different measurement techniques and signal acquisition methods – namely measurement of absorption, and measurement of photocurrent, but are still in strong correspondence with each other. The results compliments each other in confirming the band gap size of the material, which is right on par from what is expected, and gives the most important confirmation of successful graphitic carbon nitride production. *It is abundantly clear that graphitic carbon nitride has been produced, as all measurement techniques even by themselves are strong confirmations.*

Claim: The exfoliation methods have been successful and improve the properties of the material. Regarding modifications of the graphitic carbon nitride, this project essentially has three versions of material to consider: bulk graphitic carbon nitride, heat exfoliated g-C_3N_4, and ultrasound exfoliated g-C_3N_4. Results from this project show that both methods of exfoliation have significant impacts on the electrochemical properties of graphitic carbon nitride. As was seen from the S(T)EM imaging in Figure 4.17 and 4.18, the layered structure of bulk graphitic carbon nitride is an inefficient utilization of the potential surface area of the material. The electrochemically active surface area can be greatly enhanced with exfoliation, and is indeed what one achieves by ultrasonication and reheating. The improvement in surface area is not quantified in this project, but it is clearly seen in the S(T)EM imaging, such as in Figure 4.22 that after exfoliation, the material is divided into singular sheets in some extreme cases, which should lead to a tremendous increase in overall surface area, boosting electrochemical properties.

Unsurprisingly, the voltammogram of the bulk sample in Figure 4.6 shows the smallest peaks and least distinct voltammogram. Both ultrasound and heat exfoliation greatly increases the currents in comparison, which is mainly attributed to the increase of surface area and reduction of recombination centers, of which g-C_3N_4 suffers greatly [2] [31]. As the flakes of the material separates more so into 2-dimensional units instead of stacked layers, it is believed that the charge transfer resistance of the system decreases due to reduced diffusion lengths for charge carriers. This would be consistent with what was expected from the S(T)EM imaging and intuition.

Further evidence of this was found in the LSV results reported in Figure 4.7. Again, bulk graphitic carbon nitride is showing the most lackluster results. Heat exfoliation has in this experiment resulted in currents twice as large, but remarkably: the ultrasonicated samples show currents almost tenfold that of the bulk powder.

EIS measurements of the three powders were also conducted and illustrated in Figure 4.8. The trend continues in the EIS measurements with bulk graphitic carbon nitride having the largest semicircle radius, implying the undesired property of having the largest charge transfer resistance. This kinetic parameter is quintessential for determining the overall performance of the system, and thus one would wish to design a material where the charge transfer resistance, and equivalently the diameter of the EIS semicircle, is as small as possible. The heat exfoliated sample has a semicircle radius half the size of the bulk sample's semicircle, and the ultrasound exfoliated sample half of that again. Evidently, the exfoliation processes in themselves contribute appreciably to making the system more kinetically akin to the transfer of charges, and ultrasound exfoliation gives the best results in both the EIS and LSV measurements. It has become abundantly clear from the S(T)EM imaging that the surface area is drastically increased, and from the electrochemical measurements that the currents become larger as a result. The mechanism is again rationalized with that in the bulk sample, charges must diffuse longer distances through the stacked layers, while the exfoliated samples ideally has no such structure. More realistically, these stacked layers are only reduced in magnitude, but still sufficiently so to have a tremendous impact on the measurements.

In essence, there should remain little doubt that electrochemical properties are greatly enhanced by the exfoliation processes. It has been demonstrably shown that the modifications of the particles happen due to the exfoliation processes, giving larger electrochemically active surface areas and higher currents. Both investigated methods of exfoliation are reasonably facile and cheap to implement and conduct. These are promising results for the potential use of graphitic carbon nitride for electrochemical and/or economic purposes.

<u>Claim</u>: *The preparation of the powders impacts the resulting properties, and washing procedures should be chosen in order to tailor the desired properties of the material.* It is evident that the washing procedures does have a non-trivial impact on performance for the resulting powder. As the powder transitions from dicyandiamide to bulk graphitic carbon nitride, and then from bulk g-C_3N_4 into an exfoliated version, it is reasonable to believe that there will remain some unconverted precursor material for each transition. Not all dicyandiamide will polymerize into graphitic carbon nitride, and not all of the bulk material will be exfoliated.

The LSV and EIS results for the different washing procedures in 4.15 and 4.16 showed that the best results are for the samples washed only after the initial synthesis of the graphitic carbon nitride, and the worst results stem from the samples washed exclusively after exfoliation. Perhaps somewhat surprisingly, this means that some washing procedures actually ended up hampering the performance of the resulting films. How may these results be rationalized? For starters, as the best results came from washing after the original heating step, and then exfoliating after this, one may envision that the washing procedure filters out excess unreacted precursors. The implication is that when the sample is heat exfoliated in a later step, all the energy goes into exfoliation, rather than converting and polymerizing the precursors. This washing procedure would lead to a higher degree of exfoliation then. As for the worst results, consider the mechanics of a centrifuge. The heaviest particles sink to the bottom, while the lighter particles may float in solution. As the solution is discarded, only the heavier particles remain. One can see how this would be detrimental to the performance of the powder if one in essence have washed away and discarded all the light, more electrochemically active exfoliated samples, and kept only the heavy bulk g-C_3N_4 as a result. The washing procedure simply does the opposite of the desired effect. This is why it performs poorly when compared to the other heat exfoliated samples. Per intuition, the powder that was washed in both steps should then perform worse than the powder only washed after the initial step, but somewhat better than the one that was only washed after the last step – this is because when washing in both steps, the precursors disappear and more of the bulk become exfoliated. If the washing procedure does not clean out *all* of the exfoliated particles, it should perform better than the one washed only after the last step. This is what is observed, and the suggested mechanism is thus in agreement with the data.

Furthermore, it was discovered that the washing procedures and associated exfoliation had noticeable effects on the band gap of the materials. As seen in Figure A.1 and Table 4.3, one can see that the band gap of the materials neatly fits the expectations of what has been discussed above. Namely that the sample that was washed after only the exfoliation, is the powder that should most resemble bulk powder; the powder washed only after the initial step should be the least similar to the bulk (as it is more exfoliated), while the sample washed in both steps should have a band gap in between these two. This is exactly what is observed in the data as well. In other words: one can tailor the electrochemical and optical properties of the material by implementing the suited washing procedure.

The overall conclusion of this is that *the recommended washing routine for optimizing electrochemical properties is washing once after the initial heating step, and no washing after exfoliation. This will remove unconverted reactants after the first step, and keep the exfoliated particles from the second step. The results indicate that* *this is the optimal way to improve the electrochemical performance of all subsequent tests. However, other washing procedures can be chosen if specific optical properties are preferred.*

Claim: The presence of platinum as a co-catalyst increases the electrochemical properties, and ultrasonication is the preferred method of depositing platinum on graphitic carbon nitride. For this project, it was chosen two methods of platinum deposition on graphitic carbon nitride. These were reduction of $PtCl_4$ with either $NaBH_4$ or ultrasonication. This would produce a catalyst-cocatalyst system where graphitic carbon nitride is denoted as the catalyst and platinum as the co-catalyst. It is extremely clear from the CV in Figure 4.10 that the presence of Pt has a tremendous effect, especially on the hydrogen evolution. When compared to the bulk sample without Pt, the currents reached with this sample is virtually negligible compared to *any* sample with Pt. Perhaps surprisingly, the presence of Pt seems to have an impact on the oxygen evolution as well, with those samples benefiting from Pt. In the measured samples, Pt seem to be a better oxygen evolution catalyst than g-C_3N_4 in its pure bulk form. This is a surprising result since platinum is considered to not be an efficient catalyst for oxygen evolution. Regardless, the voltammograms with Pt do share a similar shape to that of the standard platinum electrode in water as seen in Figure 2.13, but the peaks towards the lower potentials is disproportionally much larger than all the other peaks in the voltammogram, showing that the platinum in this system mainly contributes to the adsorption and production of hydrogen gas. The peak in question reaches currents almost 70 times larger in magnitude for both of the platinum enhanced samples, which had 20wt% Pt.

Similar results are expected and observed in the corresponding LSV in Figure 4.11. Here, the bulk sample without platinum has a negligible hydrogen evolution compared to the samples with Pt. The figure shows that the weight percentage of platinum is also of tremendous importance. The sample with 1wt% platinum does increase the measured currents, but not nearly to the same extent as the samples with 20wt%, which sees an increase in current density of 3 orders of magnitude. This is regardless a reasonable and expected outcome.

The EIS results shown in Figure 4.12 show that the two exfoliated samples have very similar impedance spectra, as one might expect. Noticeably, they seem to have two semicircles each, both of similar radii. An interpretation of this is that there are two systems that the charges diffuse through, and that they have similar charge transfer resistances. These two systems are consequently the platinum particles and graphitic carbon nitride respectively. The S(T)EM imaging in Figures 4.19, 4.20 and 4.21 demonstrates that this is the case, with platinum adhering in different ways for different samples. It is noted that the EDX results in 4.17 and C.1 in the Appendix illustrate that platinum, carbon and nitrogen are detected in the EDX, as expected from the experimental procedures, but that the measurement also picks up a non-trivial amount of copper and aluminum. The presence of copper is easily explained by the fact that the sample is supported on a copper-grid. Aluminum has been detected in all samples, both pristine, exfoliated, and with co-catalyst. It is suspected it is related to a detection issue with the instrumentation itself, as there is no reason to believe that there is considerable amounts of aluminum in *any* of the samples for this project. One should thus be somewhat vary of using EDX for quantitative measurements, as it is more suited for qualitative inspection.

For the bulk g-C_3N_4, ultrasound deposition of Pt seem to yield slightly better results than $NaBH_4$-Pt, but both methods enhance the electrochemical properties of g-C_3N_4 drastically and either could be used interchangeably for similar results.

Claim: The combination of ultrasound exfoliated g-C_3N_4 and ultrasound deposition of platinum yields a catalyst-cocatalyst system that greatly enhances the electrochemical usage of platinum and overall properties, and is the recommended optimal synthesis method. Initially, depositing Pt on bulk samples give all similar graphs with similar values for both methods of Pt reduction. However, when depositing Pt on samples that are exfoliated in some way, one result stands out. Looking at Figure 4.13, there are tremendous differences in the samples with Pt from ultrasound. Bulk and heat exfoliated samples with ultrasound Pt show similar results as earlier. However, g-C_3N_4 exfoliated with ultrasound, where the platinum was reduced also using ultrasound, shows a voltammogram that is strikingly similar to the voltammogram for pure platinum. It is also almost an order of magnitude larger in currents densities for the entire voltammogram. There are clear peaks for ads/des of hydrogen towards lower voltages, formation of hydroxide and oxide towards the higher voltages, as well as the deforming of oxide at the reverse scan. It is evident that this particular method of synthesizing the catalyst-cocatalyst system, which was the culmination and combination of all the most successful research parameters so far in the project, has resulted in a system where the deposited platinum is highly activated and participating in the electrochemical reactions. This is a very uplifting result for a number of reasons. Firstly, the increased currents gives a greater number of potential applications, but especially for the evolution of hydrogen. Secondly, getting more effect out of each platinum particle contributes to making the system more economic, which in turn is essential for its viability within the field of hydrogen production. The environmental impact is also greatly reduced when less platinum is needed to achieve the same effect. *The combination of ultrasound exfoliated g-C_3N_4*

and ultrasound deposited Pt yields a sample where the platinum is highly activated and participating, greatly enhancing the overall performance and is the recommended procedure from these experiments.

Claim: The band gap of the material is tuneable with basis in the synthesis steps, and all methods explored in this project gives graphitic carbon nitride materials that are suited for water splitting. Mott-Schottky analysis in parallel with the Tauc plot method gives a powerful way to investigate the flatband potential and band gap, which in essence provide all the information necessary to infer if a material is theoretically able to split water with sunlight. The selection of energy diagrams compiled in Figure 4.26 showed that all investigated samples indeed are theoretically suited for photohydrolysis. The combined information of the flatband potential, as retrieved from the Mott-Schottky method illustrated in Figure 4.23, and the band gap, retrieved from the Tauc plot method in Figure 4.25 demonstrably showed that with such a negative flatband potential and large band gap, water splitting is very achievable due to the placements of the band edges and overpotentials relative to the water half reactions. There were some frequency disparities in the Mott-Schottky plots – meaning that the three extrapolated lines did not converge to a single value. However, the discrepancies range from 0.20 V at worst to 0.02 V at best, with an average discrepancy of 0.10 V. This is a markedly better result than what was found in the prior project, where the discrepancies would representatively be around 0.5 V.

It is evident from these results that both the flatband potentials and band gaps make all of the produced samples suited for photohydrolysis, and that the band gap may be tuned within the extremities discovered in this project. When compared to the solar spectrum at sea level in Figure 4.27, one can see that although g-C_3N_4 absorbs a small portion of the spectral irradiance, g-C_3N_4 absorbs the high-energy part of the spectrum which still has relatively large intensities. Unfortunately, the tuning possibilities researched in this project strictly increases the size of the band gap, making less of the sunlight available for hydrogen production. Ideally, the produced powder would absorb larger portions of the spectrum when tuned, but this is evidently not the case. There should however be no doubt that gas production from water using sunlight is highly achievable with the researched materials.

Claim: Graphitic carbon nitride does produce hydrogen when illuminated by a solar spectrum. All characterization and electrochemistry aside, the inevitable test of success for this project is the verification of whether the produced substances actually can facilitate hydrogen evolution or not. The discovered effects that exfoliation has on the electrochemical results; the effect of Pt on the charge densities; the different washing – these procedures matter little in the end if they for one reason or another inhibit the photocatalysis of water. Figure 4.35 shows the successful hydrogen evolution results gathered from this project, and while some results were uplifting, others surprised in a negative manner. Firstly, one would expect the bulk graphitic carbon nitride to show the worst results – if any at all. It is common in literature that there is virtually no hydrogen evolution detected for pristine bulk g-C_3N_4 [2] [35]. However, it was found that our washed bulk sample produced more hydrogen than some papers report *with* co-catalysts, such as Ni/NiO [35] and Pt [33]. This would be a result to be very skeptical of at first, but given the particularly linear nature of the hydrogen evolution with illumination time ($R^2 = 0.9993$), there seems to be little reason to doubt the validity of this result. It was discovered during different measurement series that the effect of stirring can not be understated. Samples without stirring would leave all the material gathering at the bottom of the reactor, not dispersed in the solution and providing unsatisfactory results, with barely any hydrogen measureable at all. *With* stirring, however, more hydrogen was detected produced in 80 minutes than in 250 minutes without stirring. It is clear that a well dispersed mixture provides a better system for generating hydrogen.

As multiple reports have shown that a weight percentage of around 1% Pt is ideal for photoevolution of water [28], it was expected that this would also be the case in this project. However, even after prolonged exposure to irradiation, no hydrogen could be detected for this sample in our case, strongly implying that although the electrochemical properties were far superior to the bulk sample, the photoevolution properties have been hampered in some way. This might be due to the platinum blocking some of the incoming radiation, although this effect should not be of such importance as the weight percentage is so small – especially for the exfoliated samples with platinum, as the S(T)EM imaging showed that these do not block significant portions of the surface. More likely is it that the lower concentration of the catalyst-cocatalyst system in the reactor (52 mg L^{-1} for the bulk experiment, 28 mg L^{-1} for the 1wt% Pt experiment) made the rate of hydrogen evolution too small to be measurable at the relevant time scale. Combining this with frequent measurements; one is actively extracting potential hydrogen from the system, possibly not giving it sufficient time to build up a measurable concentration. There is also the possibility of gas leakage, as there is no way to make the system at hand fully foolproof. This is an experiment that should be repeated, preferably with varying weight percentages of co-catalyst in order to establish both a correlation between co-catalyst loading and hydrogen evolution, as well as seeing if the concentration of the catalyst-cocatalyst was the determining factor for not observing any hydrogen for this particular experiment. It is very unfortunate to be unable to report results with co-catalysts for this project. The ongoing research on g-C_3N_4 is very focused on platinum deposition in order to increase the rate of gas evolution but, however, due to time constraints, this was not achievable in this project. On the other hand, as discussed in the next section, although much research is on platinum and graphitic carbon nitride, it would arguably be more interesting to investigate a co-catalyst that promotes the evolution of oxygen instead of hydrogen.

Claim: In order to increase gas evolution on graphitic carbon nitride, the main co-catalyst should not be platinum, but rather a catalyst which facilitates the oxygen evolution reaction. In literature, graphitic carbon nitride is often coupled with platinum as a co-catalyst. This is because, as has been thoroughly researched in this project, graphitic carbon nitride has a suitable band gap and band edge placements for water splitting, and the assumption is then that platinum will speed up the hydrogen production in the system – leading to a viable fuel for a less carbon intensive world. However, one must consider whether this is the most rational design choice for graphitic carbon nitride. Keeping in mind that platinum is a great catalyst for hydrogen evolution, but poor catalyst for oxygen evolution, this might not actually be the best choice of material. There are multiple reasons for this. The easiest one is to consider the energy diagram, as seen in Figure 4.26. The overpotential for the reduction reaction, that is, the half reaction giving the hydrogen gas, is very large. At the same time, the overpotential for the oxidation reaction, which involves holes and oxygen gas production, is significantly smaller. For a system where semiconductor particles are dispersed in a vessel and illuminated, both of these processes must happen at the same time at the same particle. There is no external circuit nor applied voltages. The system operates at open circuit potential (OCP), so to speak. The overall reaction rate thus depends on the slowest of these two half reactions, and considering the overpotentials alone, this is clearly the OER. Adding platinum to this system does not benefit the evolution of oxygen and is thus an inefficient way of increasing the overall reaction rate, which the HER is also dependent on. Catalyzing the oxygen half reaction would therefore be a more rational approach than catalyzing the hydrogen evolution reaction for such a system. Disregarding the aspects of separating these gases after they have been produced, which is beyond the scope of this project, one could argue that this problem could be somewhat remedied by using a different setup, for example a two or three electrode system, where the hydrogen is produced at a graphitic carbon nitride electrode. For this system, the oxygen evolution problems could be addressed by having a counter electrode which catalyzes the second half reaction. But consider that in order for hydrogen to be produced at a site, it needs the electrode to provide it with electrons. The reaction happens on a cathode, in other words. Now, it has been shown that g-C_3N_4 has a very negative flatband potential, around -1.1 V. The open circuit potential is much larger than this – larger than 0.0 V, in fact – which means that the energy bands bend upwards towards the electrolyte in the energy diagrams. This means that incident light will not provide electrons to the solution; it will provide holes. Equivalently stated: graphitic carbon nitride acts as a photoanode under these conditions. Research overwhelmingly shows that most articles present anodic photocurrent responses in graphitic carbon nitride [25] [30] [32] [33]. Graphitic carbon nitride is simply in most cases not best suited for producing hydrogen as a singular electrode, and adding platinum as a co-catalyst is not properly addressing the problem at hand. By changing the voltage, one changes the photocurrent response from anodic to cathodic, but this has limited interest when considering the possibilities for large-scale production of hydrogen from this system. Graphitic carbon nitride would from this reasoning benefit more from a decent oxygen evolution co-catalyst than platinum, simply because g-C_3N_4 provides anodic currents under normal modes of operation.

Claim: Band bending in larger particles benefit gas evolution, but the increased surface area of exfoliated particles gives indecisive conclusions regarding particle size recommendations. When assessing the energy diagram for a single semiconductor particle in an aqueous solution, there are both quantitative and intuitive models that show that larger particles will perform better for graphitic carbon nitride. This is due to the placement of the band edges and the level of band bending. Figure 2.7 illustrates how the band bending favors the production of oxygen by making holes more present at the surface of the particle, and it has already been detailed how the oxidation reaction is the limiting factor for high gas production. So increased levels of band bending will be beneficial for the evolution of oxygen, and hydrogen by extension in this system. However, the electrochemical tests, i.e. the CVs, LSVs and EIS's showed that increased surface area from exfoliation drastically improved many of the desirable properties of the g-C_3N_4. In addition, the exfoliation processes increased the band gap, effectively increasing the overpotential for the oxidation reaction simultaneously. It is clear that these size-dependent aspects of water splitting – and the oxidation reaction in particular – pulls the conclusion in opposite directions, and as this project has not sought to quantify the effects of these measures, one cannot make a decisive decision on what would be best for the overall reaction rate. It can, however, be noted that the platinum deposition was significantly more successful in exfoliated samples, which might also be the case for a co-catalyst that benefits the OER. This is only speculation at the current stage of research, however, and would need further research in order to reach a conclusion.

6 Conclusion

Graphitic carbon nitride is a very promising and exciting material for providing one of the many necessary solutions for decarbonizing our world. It is cheap, made from abundant and conflict-free materials and can provide renewable energy from readily available inputs in virtually every corner on Earth. This project has successfully created graphitic carbon nitride from a simple one-step heating process from dicyandiamide, with confirmations deduced from techniques such as XRD, TGA, S(T)EM, EDX, color changes and diffuse light reflectance. The band gap, and flatband potentials from Mott-Schottky analysis in acidic solutions, showed that water splitting is very feasible, with tunable band gaps ranging from 2.66 eV for a pristine bulk sample to 2.84 eV for a heat exfoliated sample, and flatband potentials measured from -1.22 V to -1.00 V. It has been shown that ultrasound and heat exfoliation enhances electrochemical properties as noted by increased currents in CVs and LSVs as well as significant reductions in charge transfer resistances measured in EIS experiments. Washing procedures were also investigated, and it was concluded that for optimal electrochemical properties, one should wash the produced g-C_3N_4 only after the initial synthesis, and not after exfoliation. Optical properties can however be tailored with choice of washing routines, as reported in this project. Platinum was investigated as a co-catalyst, and although it certainly improves the electrochemical properties of g-C_3N_4, it was deduced from theory and photocurrent responses that it is not the recommended co-catalyst for water splitting at graphitic carbon nitride particles or electrodes without external bias, due to g-C_3N_4 usually operating as a photoanode, not photocathode. Regardless, ultrasound deposition of platinum was shown to both yield better properties for g-C_3N_4 than reducing Pt with $NaBH_4$, and that the platinum was highly activated and electrochemically participating when reduced on ultrasound exfoliated samples. As it was reasoned that the oxygen evolution reaction is the rate limiting step for the discussed reactor systems, it is recommended to investigate co-catalysts that is more suited to catalyze the oxidation half reaction in water. Decisions regarding the choice between large particles with large band bending and small particles with large surface areas can not be properly answered without more research as these two effects contributes in opposite directions. Results showed that hydrogen is actually produced when graphitic carbon nitride is illuminated by a solar spectrum, but it needs to be well dispersed in solution with stirring to ensure good utilization of the material. The possibilities for a greener future with graphitic carbon nitride providing parts of the solution is foreseeable, and the results from this project should provide many key insights on how to further develop and research this promising material with rational design philosophies going forward.

7 Further work

There is a multitude of pressing and interesting aspects to research further, in greater detail, or, simply redo with higher accuracy and reproducibility. Most interestingly would it be to do all hydrogen evolution tests multiple times, with different powders, concentrations and different co-catalyst loadings for relevant samples. As this is the most direct and telling result for a project of this nature, getting lots of data to evaluate the relationship between different production parameters and optimal gas evolution would be hugely beneficial for making further assessments. Analyzing the overall cost of the system would also be of great benefit for any potential economic application, which would reveal the true viability and potential of graphitic carbon nitride. Getting rigorous and systematic data on how the changes in production parameters affect the final gas evolution would also reduce any and all uncertainties that came with lackluster or unexpected results in this project, which mainly stemmed from either lack of time or insufficient quantities of powder material. With substantial gas evolution data, one could rely more on these data for deciding which parameters to continue researching, as opposed to depending solely on the electrochemical tests.

Two co-catalysts in particular that would be of great interest to research, would be nickel-based materials as well as iridium based materials. Both of them for the sake of increased oxygen evolution, but where the first one would intriguing due to better availability and lower prices, while the latter would be exceptionally interesting for its known great catalytic effects on oxygen evolution. Many arguments were made in this project for catalyzing the OER rather than the HER, and there is reason to believe that Ni- and Ir-based materials could be the pieces that solves this puzzle.

Another interesting aspect that was not researched in detail was the effects of pH. For the Mott-Schottky measurements in particular, it would be natural to see whether the shifts of the curves would follow Nernst's Law, or if the pH itself could alter the properties of the material to such an extent that the flatband potentials change to unexpected values. All hydrogen evolution tests were done in deionized water in order to better compare with literature values, and obviously it would be tremendously fascinating to investigate the effects of pH on fundamental quantities for g-C_3N_4 as well as its effects on the final gas evolution. An acidic solution would provide g-C_3N_4 with plentiful of H^+-ions to reduce, so coupling this with a hole scavenger during gas evolution would yield valuable insights in how low-pH environments could benefit or be detrimental to the overall gas evolution, and then naturally do the complete opposite procedure for an alkaline solution. Considering these three scenarios in relation to each other, while keeping the costs of fabrication and chemicals in mind, one would take great steps towards being able to assess the economics of the proposed system.

From the XRD results, one could further investigate using the Scherrer equation and Rietveld refinement to assess if the observed nanoparticle sizes correspond to what was observed in the S(T)EM imaging, and to characterize data about the crystallite size and quantitative data which could be compared to expectations and other measurements from this project. This could in principle be done with the existing data sets even, so it would be interesting to see whether this data would agree with conclusions drawn so far.

There are many experimental techniques which were not utilized in this project that would also expand upon the knowledge of graphitic carbon nitride and its many modifications. Surface area could be investigated with BET measurements and compared to other measurements, such as S(T)EM imaging, the charge transfer resistance and hydrogen evolution results in particular. Perhaps being able to quantify the whether smaller particles with higher surface areas are better for the overall reaction rate than bigger particles with larger band bending is a road to explore, as the conclusions were indeterminable at best in this project. For a more fundamental understanding of the chemistry and structure of g-C_3N_4, techniques such as XPS could be used in order to understand the fundamental structure and binding of atoms in the polymeric units that make up this material.

Experimentation with doping and different ways of altering the surface structure seems very promising, as many papers go into lengthy detail about the added benefits graphitic carbon nitride exhibits when certain alterations are done to both the surface structure and the molecular structure, for example porous structures or nitrogen- or phosphor substitutions in the polymer structure itself. For investigating the surface, one could compare how results from AFM (Atomic Force Microscopy) experiments would look in relation to S(T)EM and BET measurements.

However, the one thing that would be advised most strongly to investigate in greater detail, would be the actual gas production under solar light irradiation. This paper managed to make some measurements in this field, and most importantly: it was decisively proved that hydrogen gas does indeed get produced, but not enough experimental was extracted from this procedure in order to make further educated guesses, to assess whether the different production parameters would correspond to an expected increase or decrease in gas production, and so on. At this stage, these data would arguably reveal the most valuable information when compared to all that was researched in this project. The second major recommendation would be exploring effects of co-catalysts with known oxygen evolution properties. Comparing evolution rates between, say, platinum and iridium as co-catalysts would reveal key insights into one of the most rewarding questions yet to be answered. The foundations for further research and rational material design has been provided in this project, and the possibilities are both many and optimistic at this point in time and research. Retrieving hard data on the gas evolution is the natural next step, as is experimenting with different co-catalysts. From there, the road ahead will be much clearer, and new and more rewarding questions and answers may be unearthed.

A Energy diagram for all measurements

The graph on the next page shows all constructed energy diagrams for samples measured in this project. There is a consistent pattern between synthesis route and the size of the band gap. In short, the band gap expands as follows: Bulk < ultrasonicated samples < heat exfoliated with washing < heat exfoliation without washing. With increasing band gap, the overpotential for the oxygen oxidation also increases, but simultaneously the portion of the spectral irradiance that get absorbed is decreased. Note how the valence band from left to right somewhat resembles a staircase moving downward to see the improvements in the overpotential for the oxygen evolution reaction.

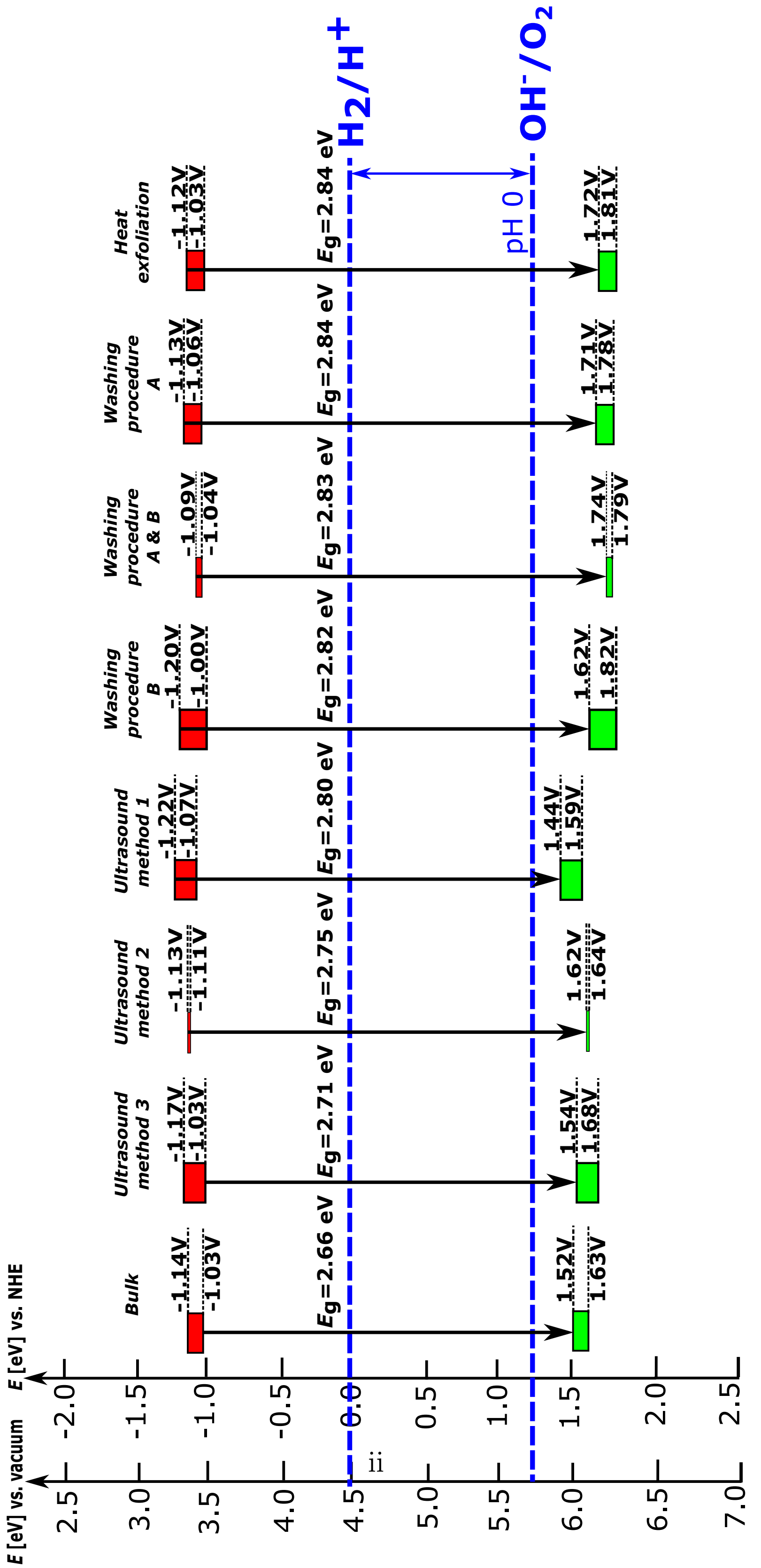

Figure A.1: All energy diagrams for graphitic carbon nitride

B Calculation of hydrogen amounts from ideal gas law

For the experimental setup used, there was 30 mL of available volume for the hydrogen to develop in. As the GC provides amount of hydrogen as a percentage of the analyzed air, one needs a way to convert this percentage into moles.

Inside the 30 mL chamber there is initially air at room temperature and athmospheric pressure. By using the ideal gas law on the background sample, one can infer the amount of nitrogen in the chamber.

Ideal gas law states:

$$PV = nRT \tag{B.1}$$

where P is pressure, V is volume, n is the number of moles, R is the ideal gas constant and T is the temperature. By rearranging, this becomes:

$$n = PV/RT \tag{B.2}$$

Filling in for these values with reasonable assumptions, one gets:

$$n = \frac{1 \text{ atm} \cdot 30 \cdot 10^{-3} \text{ L}}{0.08205 \text{ L atm mol}^{-1} \text{ K}^{-1} \cdot 298 \text{ K}} = 1.227 \text{ mol air} \tag{B.3}$$

Let now the percentage of nitrogen detected in the background measurement be noted as $[\%]_{\mathrm{N}_2}^{\mathrm{back}}$. One knows that the number of moles of N_2 must be:

$$n_{\mathrm{N}_2} = 1.227 \cdot [\%]_{\mathrm{N}_2}^{\mathrm{back}} \tag{B.4}$$

In any new samples then, the following relation would hold true:

$$[\%]_{\mathrm{N}_2} \cdot n_{\mathrm{tot}} = n_{\mathrm{N}_2} \tag{B.5}$$

And at the same time, the equivalent must hold true for hydrogen: In any new samples then, the following relation would hold true:

$$[\%]_{\mathrm{H}_2} \cdot n_{\mathrm{tot}} = n_{\mathrm{H}_2} \tag{B.6}$$

By solving all of this equations for n_{H_2}, one thus gets

$$n_{\mathrm{H}_2} = [\%]_{\mathrm{H}_2} \cdot \frac{1.227 \cdot [\%]_{\mathrm{N}_2}^{\mathrm{back}}}{[\%]_{\mathrm{N}_2}} \tag{B.7}$$

For example, if a background measurement showed a background value for nitrogen to be $[\%]_{\mathrm{N}_2}^{\mathrm{back}} = 78.67\%$, and a subsequent hydrogen measurement gave the measured values $[\%]_{\mathrm{H}_2} = 0.0049\%$ and $[\%]_{\mathrm{N}_2} = 72.73\%$, one would get:

$$n_{\mathrm{H}_2} = 0.000049 \cdot \frac{1.227 \cdot 0.7867}{0.7273} = 65 \cdot 10^{-6} = 65 \text{ µmol } \mathrm{H}_2 \tag{B.8}$$

C EDX results

It is seen in the EDX that a few materials that do not fit the intuition is also included in the graph. The presence of copper is explained by the copper grid that the sample is supported on. Aluminum has been consistently showing up in all measurements for this and the previous project, and it is assumed that it is somehow related to the instrument itself, and not and actual detection in the sample.

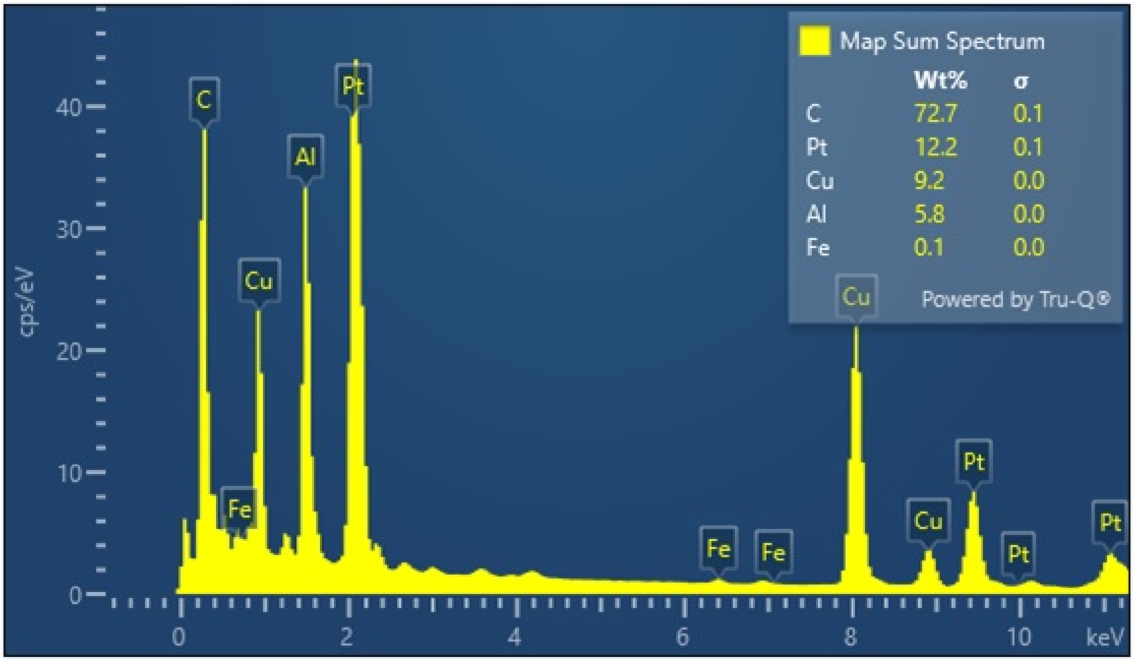

	Wt%	σ
C	72.7	0.1
Pt	12.2	0.1
Cu	9.2	0.0
Al	5.8	0.0
Fe	0.1	0.0

Figure C.1: EDX of gCN with Pt

D S(T)EM imaging

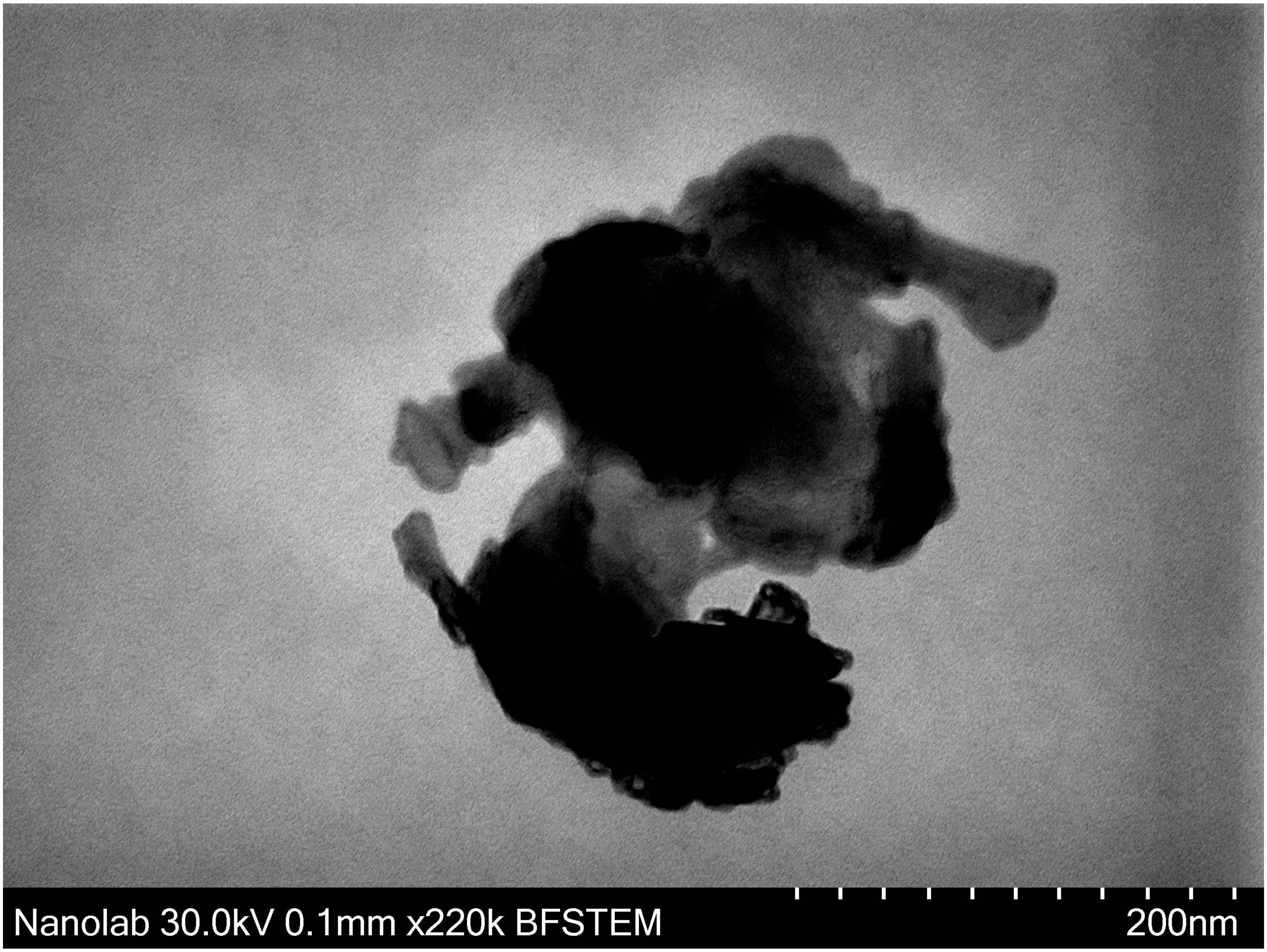

Figure D.1: S(T)EM of heat exfoliated g-C_3N_4. One can clearly see how the sample has been partially exfoliated, since parts of the particle is see-through (few stacked sheets), while other parts are not see-through (many stacked sheets).

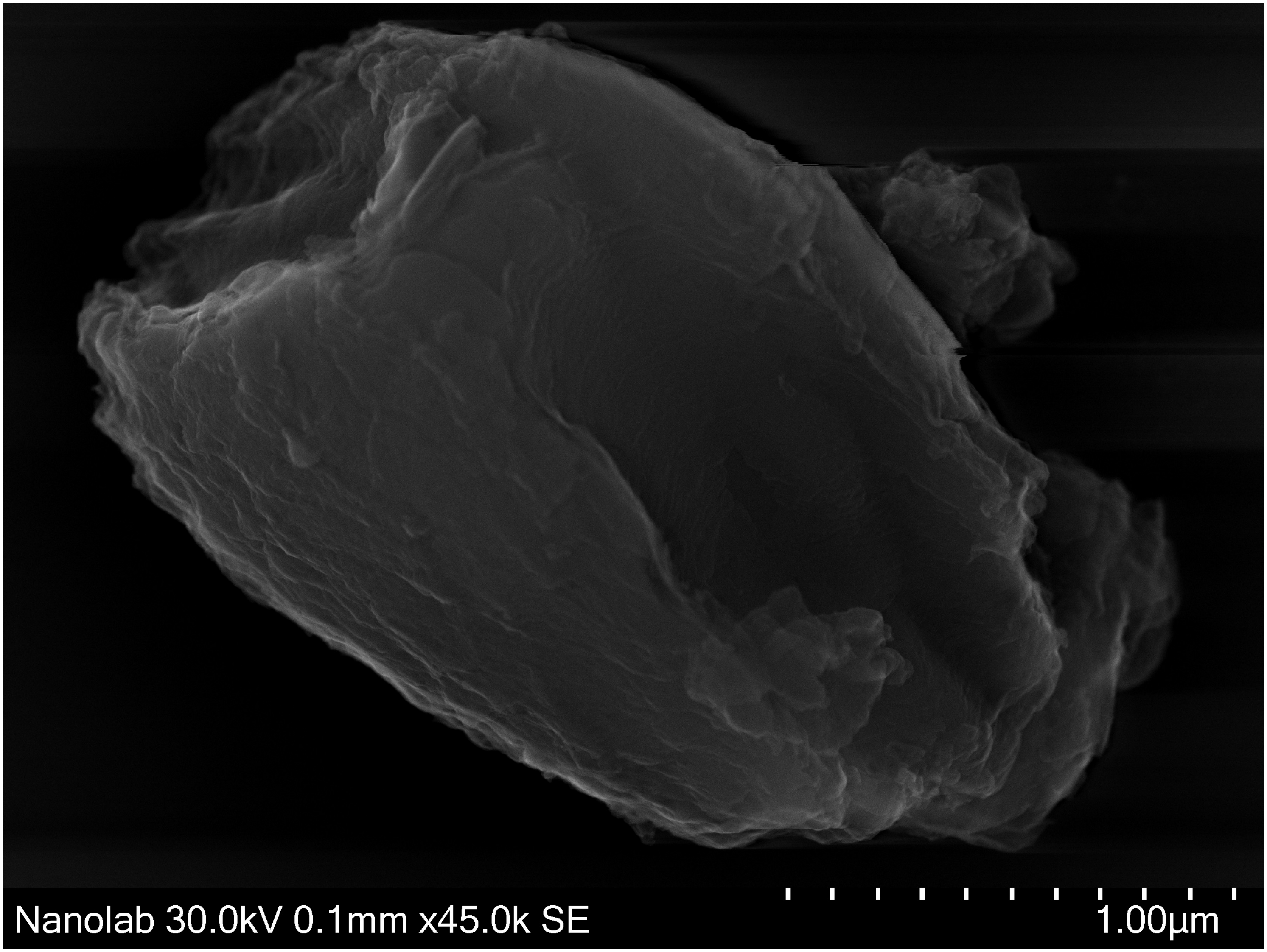

Figure D.2: S(T)EM showing graphitic layers of g-C_3N_4. Especially at the left part of the image, one can see how this bulk sample is very layered and graphitic.

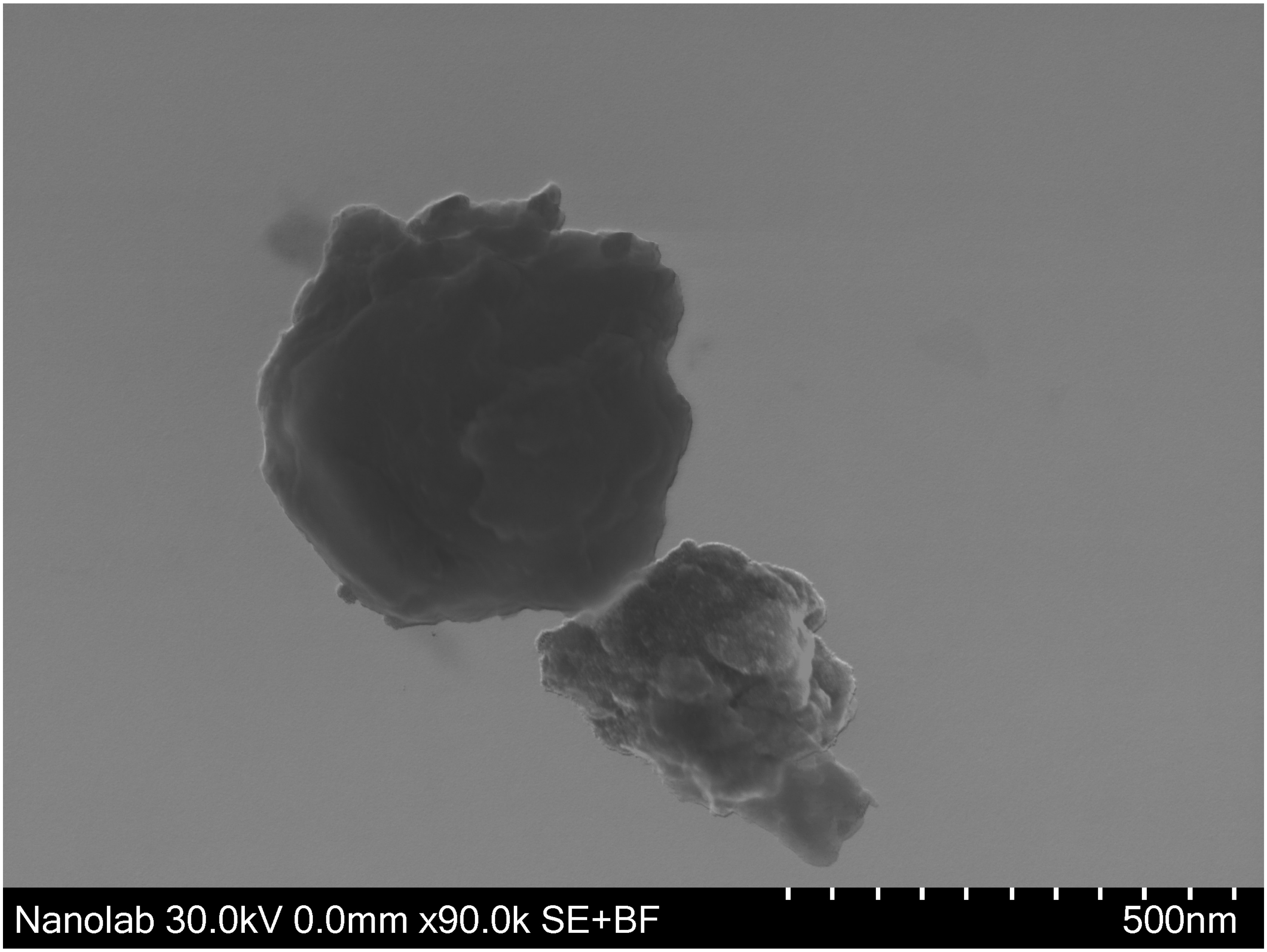

Figure D.3: S(T)EM showing clumping of platinum on bulk g-C_3N_4. The platinum is not evenly dispersed on the particle, as was shown for the exfoliated samples.

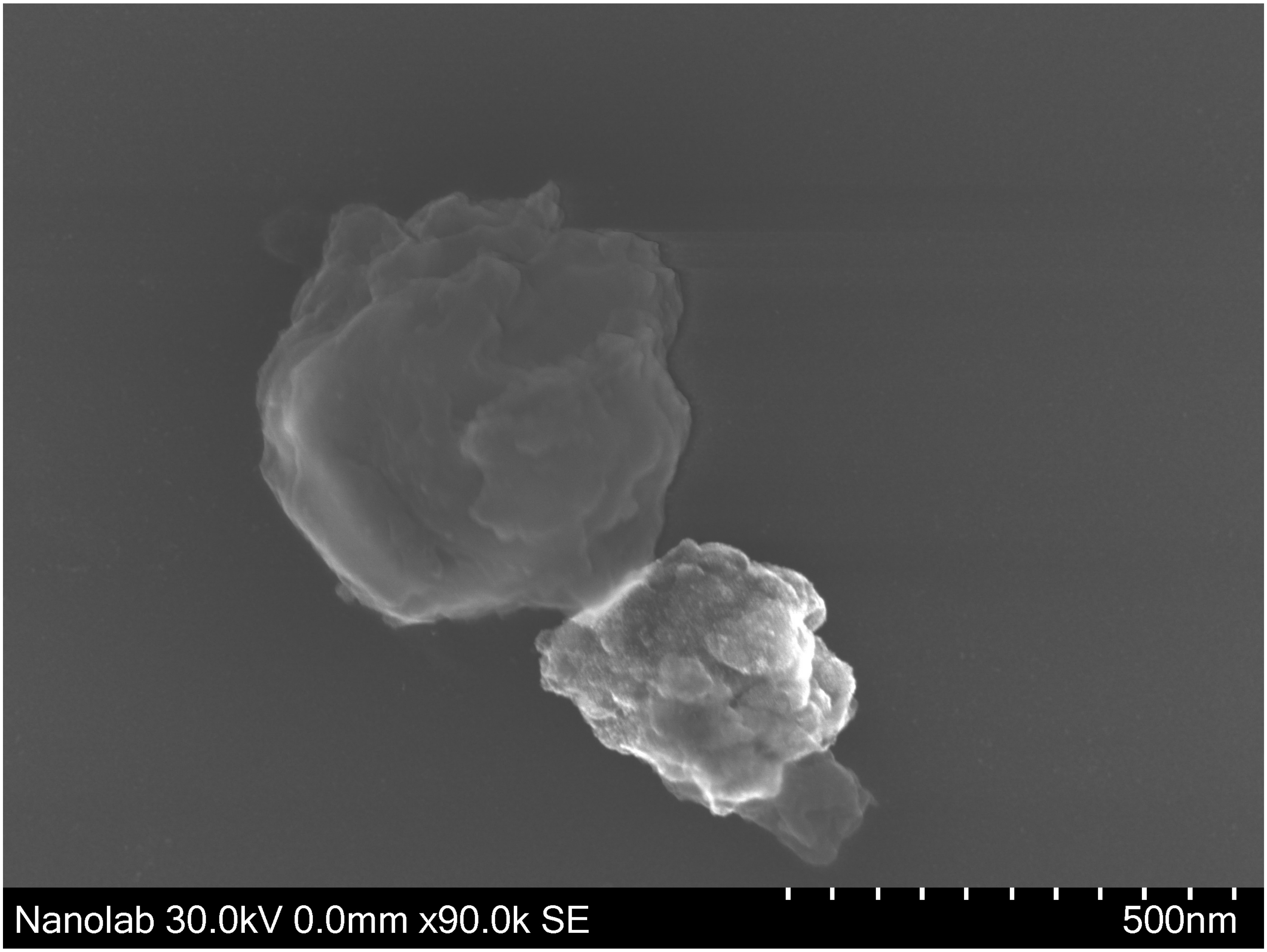

Figure D.4: S(T)EM showing clumping of platinum on bulk g-C_3N_4. The platinum is not evenly dispersed on the particle, as was shown for the exfoliated samples.

References

[1] Euro Alliages, EUROPEAN FERRO-ALLOYS AND SILICON PRODUCTION: NON-EXHAUSTIVE LIST OF TECHNOLOGICAL OPTIONS AND SOME EXAMPLES OF PROJECTS, *Comité De Liaison Des Industries De Ferro-Alliages*. 2019.

[2] S. J. Mun and S.-J. Park, *Graphitic Carbon Nitride Materials for Photocatalytic Hydrogen Production via Water Splitting: A Short Review*, Catalysts, 2019.

[3] A. J. Nozik and R. Memming, *Physical Chemistry of Semiconductor-Liquid Interfaces*, J. Phys. Chem, 1996.

[4] Atkins, P.W., T.L. Overton, J.P. Rourke, M.T. Weller, F.A. Armstrong: *Inorganic Chemistry* 6th Edition, Oxford University Press, Oxford, 2014.

[5] K. Gelderman, L. Lee, and S. W. Donne, Flat-Band Potential of a Semiconductor: Using the Mott–Schottky Equation, *Journal of Chemical Education*, 2007.

[6] K. B. Oldham, J. C. Myland, A. M. Bond, *Electrochemical Science and Technology: Fundamentals and Applications, First Edition.* John Wiley & Sons, Ltd, 2012.

[7] M. N.Paddon-Row: *Orbital interactions and long-range electron transfer - Advances in Physical Organic Chemistry* volume 38, 2003.

[8] A. J. Bard, A. B. Bocarsly, F.-R. F. Fan, E. G. Walton and M. S. Wrighton, *The Concept of Fermi Level Pinning at Semiconductor/Liquid Junctions. Consequences for Energy Conversion Efficiency and Selection of Useful Solution Redox Couples in Solar Devices*, 1980.

[9] Z. Zhang and J. T. Yates, Jr, *Band Bending in Semiconductors: Chemical and Physical Consequences at Surfaces and Interfaces*, Chemical Reviews, 2012.

[10] A. Victorious, S. Saha, R. Pandey, T. F. Didar, L. Soleymani, *Affinity-Based Detection of Biomolecules Using Photo-Electrochemical Readout*, Frontiers in Chemistry, 2019.

[11] L. M. Petera, A. B.Walker, T. Bein, A. G. Hufnagel, I. Kondoferskyc, *Interpretation of photocurrent transients at semiconductor electrodes: Effects of band-edge unpinning*, Journal of Electroanalytical Chemistry, 2020.

[12] I. Hwang, C. R. McNeill, N. C. Greenham, *Modelling the photocurrent transients currents in bulk heterojunction solar cells*, Journal of Applied Physics, 2009.

[13] B. G. Pollet, *The use of ultrasound for the fabrication of fuel cell materials*, International Journal of Hydrogen Energy, 2010.

[14] K. Okitsu, Y. Mizukoshi, H. Bandow, Y. Maeda, T. Yamamoto and Y. Nagata, *Formation of noble metal particles by ultrasonic irradiation*, Ultrason Sonochem, 1996.

[15] H. E. Hansen, F. Seland, S. Sunde, O. S. Burheimb and B. G. Pollet, *Two routes for sonochemical synthesis of platinum nanoparticles with narrow size distribution*, Materials Advances, 2021.

[16] J. Tauc, R. Grigorovici and A. Vancu, *Optical Properties And Electronic Structure of Amorphous Germanium*, Phys. Status Solidi B, 1966.

[17] E. Rosencher, B. Winter, *Optoelectronics*, Oxford University Press, 2002.

[18] J. I. Pankove, *Optical Processes in Semiconductors*, Dover, 1971.

[19] D. Pletcher, R. Greff, R. Peat, L. M Peter, J. Robinson, *Instrumental methods in electrochemistry*, Woodhead Publishing, 2002.

[20] Cambridge Department of Chemical Engineering and Biotechnology, *Linear Sweep and Cyclic Voltametry: The Principles.* Retrieved from https://www.ceb.cam.ac.uk/research/groups/rg-eme/Edu/linear-sweep-and-cyclic-voltametry-the-principles, June 2021.

[21] J. E. B. Randles, *Kinetics of rapid electrode reactions*, Discussions of the Faraday Society, 1947.

[22] E. S. Ameh, *A review of basic crystallography and x-ray diffraction applications*, The International Journal of Advanced Manufacturing Technology, 2019.

[23] J. Goldstein, D. E. Newbury, D. C. Joy, P. Echlin, C. E. Lyman, E. Lifshin, L. Sawyer and J.R. Michael, *Scanning Electron Microscopy and X-Ray Microanalysis* 3rd Edition, Springer US, 2003.

[24] A. Mohammed, *Scanning electron microscopy (SEM): A review*, 2018.

[25] M. Ismael, Y. Wu, D. H. Taffa, P. Bottkea and M. Wark, *Graphitic carbon nitride synthesized by simple pyrolysis: role of precursor in photocatalytic hydrogen production*, New J. Chem., 2019.

[26] P. Niu, L. Zhang, G. Liu, H.-M. Cheng, *Graphene-Like Carbon Nitride Nanosheets for Improved Photocatalytic Activities*, Advanced Functional Materials, 2012.

[27] Z. Zhao, Y. Ma, J. Fan, Y. Xue, H. Chang, Y. Masubuchi, S. Yin, *Synthesis of graphitic carbon nitride from different precursors by fractional thermal polymerization method and their visible light induced photocatalytic activities*, Journal of Alloys and Compounds, 2017.

[28] G. Zhang, Z.-A. Lan, L. Lin, S. Lina and X. Wang, *Overall water splitting by Pt/g-C3N4 photocatalysts without using sacrificial agents*, Chemical Science, 2016.

[29] X. Wei, Y. Qiu, W. Duan and Z. Liu, *Cathodic and anodic photocurrents generation from melem and its derivatives*, The Royal Society of Chemistry, 2015.

[30] K. Xu, A. Chatzitakis, E. Vøllestad, Q. Ruan, J. Tang and T. Norby, *Hydrogen from wet air and sunlight in a tandem photoelectrochemical cell*, International Journal of Hydrogen Energy, 2019.

[31] R. Kavithaa, P.M. Nithyab, S. Girish Kumarc, *Noble metal deposited graphitic carbon nitride based heterojunction photocatalysts*, Applied Surface Science, 2020.

[32] H. Wang, X. Zhang, J. Xie, J. Zhang, P. Ma, B. Pan and Y. Xie, *Structural distortion in graphitic-C3N4 realizing efficient photoreactivity*, The Royal Society of Chemistry, 2015.

[33] H. Liua, D. Chen, Z. Wanga, H. Jinga, R. Zhanga, *Microwave-assisted molten-salt rapid synthesis of isotype triazine-/heptazine based g-C3N4 heterojunctions with highly enhanced photocatalytic hydrogen evolution performance*, Applied Catalysis, 2016.

[34] Y. Yuan, L. Zhang, J. Xing, M. Iqbal B. Utama, X. Lu, K. Du, Y. Li, X. Hu, S. Wang, A. Genç, R. Dunin-Borkowski, J. Arbiold, and Q. Xiong, *High-yield synthesis and optical properties of g-C3N4*, Nanoscale, 2015.

[35] G. Zhang, G. Li, and X. Wang *Surface Modification of Carbon Nitride Polymers by Core– Shell Nickel/Nickel Oxide Cocatalysts for Hydrogen Evolution Photocatalysis*, ChemCatChem, 2015.

NTNU

Norwegian University of
Science and Technology